AD NUMBER
AD849535
LIMITATION CHANGES

TO:

Approved for public release; distribution is unlimited.

FROM:

Distribution authorized to U.S. Gov't. agencies and their contractors; Administrative/Operational Use; DEC 1968. Other requests shall be referred to Air Force Rocket Propulsion Lab., Edwards AFB, CA.

AUTHORITY

AFRPL ltr 27 Oct 1971

AD849555

STRUCTURE AND REACTIVITY OF
ENERGETIC CHEMICAL SPECIES

Larry Kevan
Marlin Harmony
Ralph Christoffersen

Department of Chemistry
University of Kansas
Lawrence, Kansas 66044

Annual Summary Report

December, 1968

DDC

MAR 27 1969

C

157

When U.S. Government drawings, specifications, or other
data are used for any purpose other than a definitely related
Government procurement operation, the Government thereby
incurs no responsibility nor any obligation whatsoever, and
the fact that the Government may have formulated, furnished,
or in any way supplied the said drawings, specifications, or
other data, is not to be regarded by implication or otherwise,
or in any manner licensing the holder or any other person or
corporation, or conveying any rights or permission to manu-
facture, use, or sell any patented invention that may in any
way be related thereto.

AFRPL-TR-68-239

STRUCTURE AND REACTIVITY OF

ENERGETIC CHEMICAL SPECIES

Larry Kevan
Marlin Harmony
Ralph Christoffersen

FORWARD

This research was carried out under Contract No. FO4611-67C-0032 with the University of Kansas, Lawrence, Kansas 66044, and was directed by Professor Larry Kevan in the Department of Chemistry. The Air Force program monitor was Dr. Lawrence P. Quinn (RPCL). This report covers research done between November 1, 1967, to October 31, 1968. This report was submitted in December, 1968.

This technical report has been reviewed and is approved.

W. H. EBELKE, Colonel, USAF
Chief, Propellant Division

ABSTRACT

Energetic chemical species have been investigated by both theoretical
and experimental methods. The spatial distribution of trapped radicals in
γ-irradiated ethyleneglycol dimethacrylate polymers and of trapped electrons
in γ-irradiated methanol, ethanol and 2-methyltetrahydrofuran has been
studied by paramagnetic relaxation methods. The radius within which elec-
trons are trapped increases with decreasing polarity of the matrix. Charge
storage in γ-irradiated polymethylmethacrylate (PMMA) and other organic
polymers doped with electron traps has been studied by measuring thermally-
induced thermoelectric and ohmic currents. The conduction mechanism for
the thermoelectric current in PMMA appears to be hole hopping between
rotating carbomethoxy side groups. The origin of the ohmic currents is not
yet clear. The theoretical technique for obtaining lower energy bounds has
been extended to multi-electron, polyatomic molecules by using Gaussian
basis orbitals. The use of Gaussians allows all integrals to be evaluated in
closed form or by a single numerical integration. In the geminal theory of
chemical bonding a new method for the determination of the best separated
pair geminals of a closed shell molecule has been developed. The efficiency
of triplet-triplet energy transfer in naphthalene-biacetyl mixtures has been
studied.

TABLE OF CONTENTS

LIST OF TABLES

LIST OF FIGURES

STRUCTURE AND REACTIVITY OF ENERGETIC CHEMICAL SPECIES

SCOPE OF THE PROGRAM

The physics and chemistry of highly energetic chemical species such as ions, electronically and vibrationally excited molecules, and free radicals is still in its infancy. The greatest paucity of information concerns excited state species; their structure, reactivity, and metastability represent a newly developing, experimentally difficult, but potentially rewarding field of study. Theoretical techniques are just now arriving at the point at which they can provide accurate and detailed information on energetic species of chemical interest. Thus, theory is reaching the point where it can supplement and guide the experimental investigation of energetic species. The characteristics of energetic species of all types in the solid state is also an area of great importance and limited information.

The areas of study are vectored toward an enhanced understanding of the physical and chemical characteristics of highly energetic chemical species. A balanced experimental and theoretical study of both structure and reactivity of carefully selected species and systems utilizing a variety of techniques characterizes the general approach used. In this annual report progress is reported in the following areas: (a) the spatial distribution of trapped radicals and electrons produced by γ-irradiation, (b) radiation-induced charge storage in organic polymers, (c) lower energy bound calculations on polyatomic systems, (d) geminal theory of chemical bonding, and (e) triplet-triplet energy transfer.

I. RADIATION-INDUCED ENERGY STORAGE
IN ORGANIC SOLIDS

High energy radiation such as gamma irradiation, vacuum ultraviolet
photons and solar wind protons expends its energy in an organic solid by
ionization and excitation processes. The product ions, free radicals and
excited molecules are inherently energetic chemical species but in suitable
solid matrices some of these species can be trapped and stored. The present
program has been vectored toward the storage potential, spatial distribution,
and detrapping mechanisms of trapped ions and free radicals. Our primary
focus has been on polymeric systems since the trapped energetic species can
be "stored" at room temperature and above and on ions, including electrons,
since ions are potentially more energetic than free radicals.

A. SPATIAL DISTRIBUTION OF TRAPPED RADICALS
IN γ-IRRADIATED ETHYLENEGLYCOL DIMETHACRYLATE POLYMERS

1. INTRODUCTION

Radiation energy is deposited by γ-rays in condensed systems
inhomogeneously and produces an initial inhomogeneous distribution of
energetic ionized and excited species. For very fast chemical reactions
the initial spatial inhomogeneity of the species involved must be taken
into account. In liquid water radiolysis such reasoning has led to the
development of the "spur" model and the consequent successful application
of diffusion kinetics.[1] Likewise in condensed systems such as polymers
and frozen solutions it is of considerable interest to determine if

trapped species exhibit an inhomogeneous spatial distribution because this may constitute the factor that limits the maximum concentration of trapped species.

Recently we showed how paramagnetic relaxation experiments can give new insights into the spatial distributions of trapped electrons and hydrogen atoms in frozen aqueous systems.[2-5] Trapped electrons in irradiated alkaline ices at $77^{\circ}K$ show no change in their relaxation time over a range of γ-dose from 0.2 to 3 Mrad even though the electron concentration increases linearly in this range; this implies that the average spin-spin interaction and the local concentration of electrons remains constant in this dose range. The results are explained by an inhomogeneous distribution of electrons trapped in spurs in which only intraspur spin-spin interactions are important.[2,3] At higher doses the spurs overlap, interspur spin-spin interactions become important and the relaxation time decreases with dose. In contrast, trapped hydrogen atoms in irradiated acidic ices at $77^{\circ}K$ exhibit a decreasing relaxation time and a linearly increasing concentration over a radiation dose range of 0.3 to 5 Mrad.[4,5] This is the behavior expected for a homogeneous distribution. The trapped hydrogen atoms are trapped only near oxyanion molecules and are expected to have a uniform spatial distribution. The relaxation results confirm this.

In the present work we have extended our paramagnetic relaxation method to trapped organic free radicals. This method depends on microwave power saturation and can be applied only to organic radicals that saturate within the range of available microwave power (typically 200 mw). We have found that radicals trapped in irradiated ethyleneglycol dimethacrylate (EDMA)

gels at room temperature fulfill this requirement. The EDMA monomers have the following structure

$$CH_2{=}C{-}C{-}O \left(-CH_2-CH_2-O-\right)_n C{-}C{=}CH_2$$

with CH_3 groups and O (double-bonded) on the carbonyl carbons as shown.
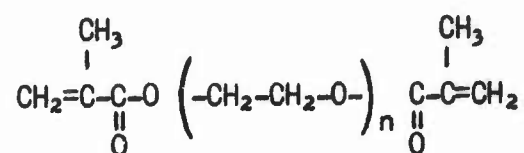
and n = 1,2,3 and 4 have been studied. Irradiation produces a rigid crosslinked polymer. Trapped radicals in irradiated polymethylmethacrylate which is not crosslinked are also saturable and have been studied recently with similar aims by Bullock et al.[6,7] The identity of the EDMA radicals and the effect of radiation dose and temperature on their relaxation time are reported. In addition, the local radical concentration and the sample-average radical concentration have been measured and compared. The results indicate that the radicals in EDMA gels are of the methacrylate type and are trapped with an inhomogeneous spatial distribution within radiation-produced spurs. The experimental results were reported in more detail last year in Report No. AFRPL-TR-67-321; but the analysis was only completed this year.

2. THEORY

Portis[8] has classified the types of paramagnetic line broadening as homogeneous or inhomogeneous. An EPR line is homogeneously broadened by interactions which allow the spin system to remain in thermal equilibrium during resonance absorption. Inhomogeneous line broadening interactions with nuclear spins cause different sets of electron spins to see different net local magnetic fields. Each such set of electron spins forms a "spin packet" and the observed spectrum of the total spin system is an envelope

of the superimposed spin packets. The shape of the envelope depends on the intensity distribution of local magnetic fields seen by the electron spins and the ratio of spin packet width to the envelope width. If the spin packet width is much less than the envelope width, as is often observed, and if the spin packets do not interact magnetically, then the envelope shape is dependent only on the intensity distribution of local magnetic fields and is Gaussian.

An electron spin system saturates when the population ratio between the upper and lower spin energy states deviates from its thermal equilibrium value. Power saturation is most readily studied by obtaining saturation curves which are plots of EPR signal intensity versus microwave magnetic field, H_1. A study of saturation behavior allows one to determine the product T_1T_2 or sometimes T_1 alone; T_1 is the spin-lattice relaxation time and T_2 is the spin-spin relaxation time. The relevant theory for obtaining relaxation times from saturation curves under slow passage conditions has been summarized in a previous paper.[3]

A typical saturation curve for the central EPR line of free radicals in triethyleneglycol dimethacrylate gel is shown in Figure I-1. An ideal inhomogeneously broadened line would have resulted in a saturation curve which had a slope of 0 at high values of H_1 whereas an ideal homogeneous line would have yielded a curve which bends down at high H_1 values even more sharply than the free radical curve.[3] If homogeneous saturation behavior is assumed T_1T_2 can be calculated from Equation (1)

$$T_1T_2 = 1/\gamma^2 H_{1/2}^2 \qquad (1)$$
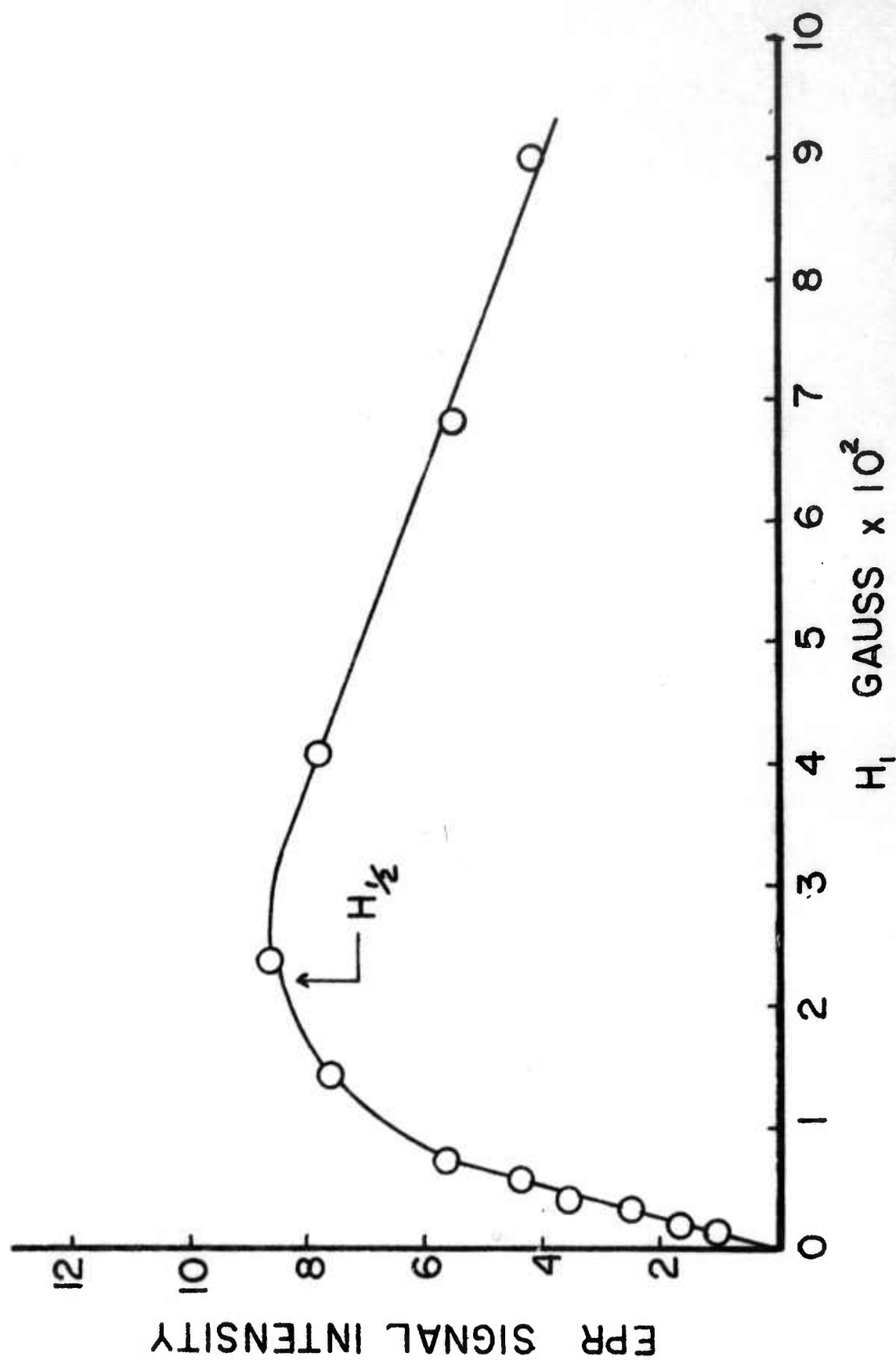
Figure 1-1. Slow passage progressive saturation curve of central line in EPR spectrum of γ-irradiated tri-EDMAX. Dose = 0.55 Mrad.

where γ is the gyromagnetic ratio of the electron and $= 1.76 \times 10^7$ gauss^{-1} sec^{-1} and $H_{1/2}$ is the value of H_1 at which the EPR signal intensity is one-half of what it would have been in the absence of saturation. If ideal inhomogeneous saturation behavior is assumed, $T_1 T_2$ is calculated by Equation (2).

$$T_1 T_2 = 3/\gamma^2 H_{1/2}^2 \qquad (2)$$

For an intermediate case such as that shown in Figure 1-1, Castner's analysis[9] may be applied using curve fitting procedures to correct $H_{1/2}$ and then using Eqn. (1) to obtain $T_1 T_2$. This method also allows the calculation of T_2 separately from Equation (3)

$$T_2 = \frac{1.70}{a\gamma\Delta H_{ms}^G} \qquad (3)$$

where ΔH_{ms}^G is the measured linewidth at maximum slope of the observed Gaussian line and a is a measure of the ratio of the Lorentzian spin packet width to the observed Gaussian linewidth; a is determined from the saturation curve.[9]

3. EXPERIMENTAL

Mono-, di-, tri- and tetraethyleneglycol dimethacrylate monomers (abbreviated mono-, di-, tri- and tetra-EDMAX where the X indicates that inhibitor has been removed) were obtained from Sartomer Resin Company and contained 60 ppm hydroquinone as an inhibitor of thermal polymerization. The hydroquinone was removed by forming its sodium salt in 1.5 M NaOH and extracting with water. The monomer was then dried over $MgSO_4$ and stored in a refrigerator.

Samples were prepared by pipetting about 2 cc of each monomer into 3 mm o.d. x 5 cm Spectrosil quartz tubes. These were irradiated at about $35^\circ C$ in a ^{60}Co γ-irradiator at a dose rate of 0.54 Mrad/hr as determined by ferrous sulfate dosimetry. Polymerization occurred[10,11] and radicals were trapped in the monomer gels which appeared to be stable for at least several days after irradiation.

The EPR measurements were made at room temperature by placing the irradiated samples in a quartz EPR dewar. After a sample had been measured at room temperature it could be measured at $77^\circ K$ by simply filling the dewar with liquid nitrogen. All EPR measurements were made on a Varian-4500 spectrometer equipped with a V-4500-41A Lo-Hi power microwave bridge, an audio modulation system, and a Varian dual cavity with dewar inserts. The bridge was operated in the low-power mode which allowed a microwave power variation over a 40-dB range. Slow passage conditions were achieved by operating with a field modulation frequency of 40 cps and a typical modulation amplitude of 0.3 gauss. The slow passage progressive saturation measurements were made as described previously.[3]

4. RESULTS

A typical EPR spectrum of radicals trapped in irradiated tri-EDMAX is shown in Figure 1-2. This is a direct recorder trace from the present work and shows the first-derivative absorption signal obtained with fast-passage (100 kc) operating conditions. Spectra from mono-, di-, and tetra-EDMAX are not shown because they are identical to that of Figure 1-2.

The relaxation time $(T_1 T_2)^{1/2}$, of free radicals trapped in tri-EDMAX was measured as a function of radiation dose and temperature under

H →

23 G
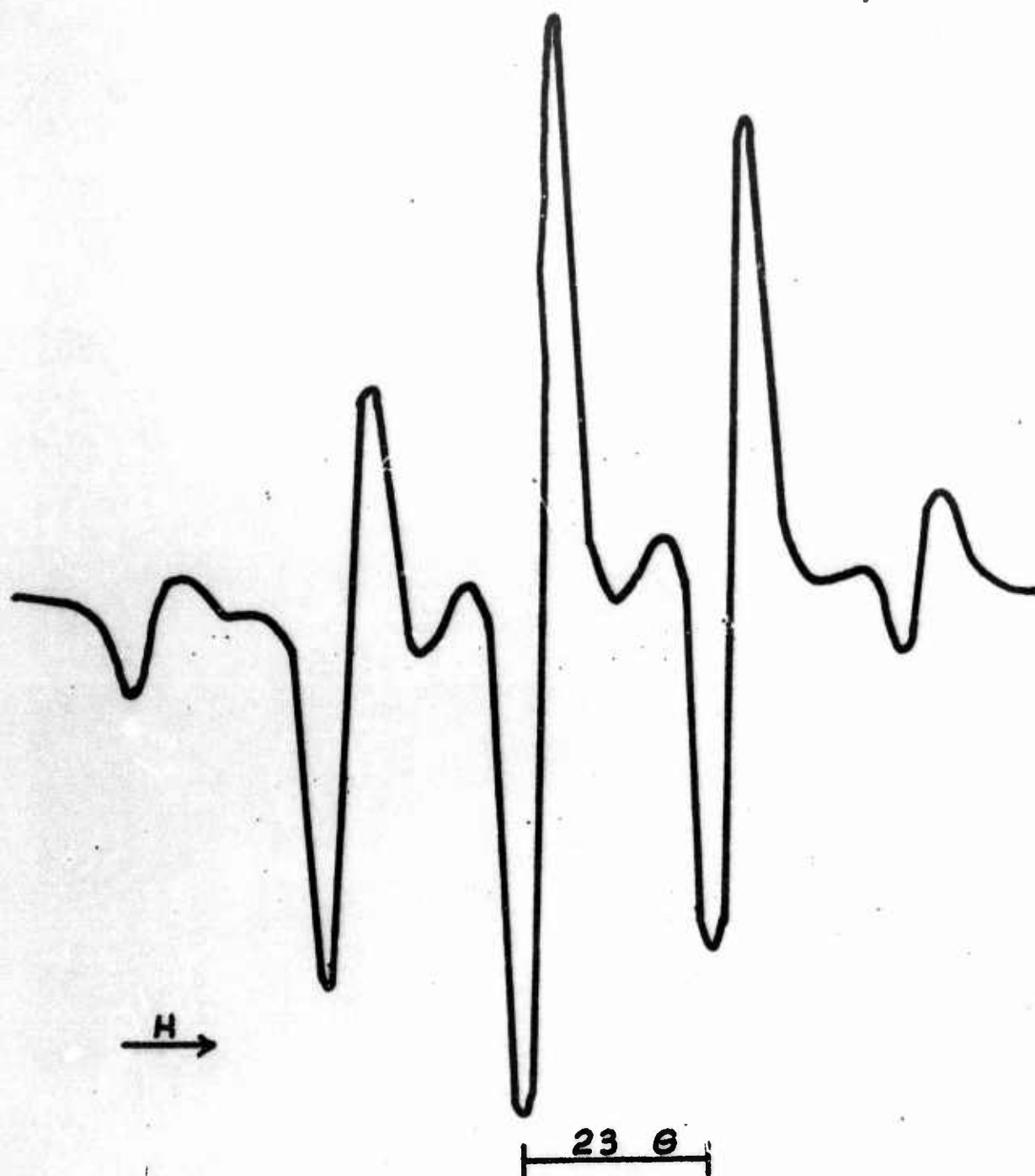
Figure 1-2. EPR spectrum of γ-irradiated tri-EDMAX at
room temperature and 0.55 Mrad dose.

slow-passage conditions. The central line of the EPR spectrum was used for the measurements. From saturation curves such as the one shown in Figure I-1 the value of $H_{1/2}$ was measured and $(T_1 T_2)^{1/2}$ was calculated from Equation (2) assuming ideal inhomogeneous conditions. Castner's[9] method was also used to calculate $(T_1 T_2)^{1/2}$ [Equation (1)] and T_2 [Equation (3)]. These data are presented in Table I-I.

Table I-II contains measurements of the linewidth between derivative maxima, ΔH_{ms}, of the central EPR line versus H_1 for trapped free radicals in tri-EDMAX at room temperature.

5. DISCUSSION

a. Radical Identification

The 9-line EPR spectrum of Figure I-2 for radicals trapped in tri-EDMAX is similar to those for radicals in mono-, di-, and tetra-EDMAX. The only observable difference among them is that the trapped radical yield increases in the direction mono→di→tri→tetra-EDMAX. Relative yield ratios for the mono- through tetra-EDMAX monomers are 1.0:1.3:2.5:2.6. The increase in radical yield correlates with the increase in length of monomer molecule and density of monomer solution. It is concluded that the radical species is the same in all four monomer gels.

Irradiated polymethylmethacrylate (PMMA) produces a radical with an EPR spectrum identical to that in the EDMAX gels.[12] This spectrum has received a great deal of study and there has been considerable argument as to whether the 9-line spectrum is due to one or two radicals.[13] However, the model suggested by Symons[14] and supported by the high resolution experiments of Fischer[15] and the deuteration experiments of Kourim and Vacek[16] lead us to assign the spectrum in Figure I-2 to the single radical

Table 1-1

Relaxation Time Versus Radiation Dose and Temperature

For Free Radicals Trapped in Tri-EDMAX Gels

Castner's "a"	Castner's $(T_1T_2)^{1/2}$, sec [a]	Castner's T_2, sec [b]	T_1, sec	Portis' $(T_1T_2)^{1/2}$, sec [c]	γ-Dose, Mrad	Temp., °K
0.5	3.1×10^{-6}	3.6×10^{-8}	2.7×10^{-4}	4.4×10^{-6}	0.55	298
0.5	3.1×10^{-6}	3.6×10^{-8}	2.7×10^{-4}	4.5×10^{-6}	1.04	298
0.5	3.3×10^{-6}	3.7×10^{-8}	3.0×10^{-4}	4.7×10^{-6}	2.09	298
0.3	3.6×10^{-6}	5.9×10^{-8}	2.6×10^{-4}	4.9×10^{-6}	2.09	73

a Eqn. (1).
b Eqn. (3).
c Eqn. (2).

Table I-II

EPR Linewidth of Free Radicals

in Tri-EDMAX Versus Microwave Magnetic Field[a]

ΔH_{ms}, Gauss	H_1 Gauss
5.2	0.00354
5.2	0.0121
5.2	0.0238
5.2	0.0900

[a] Measured on Central Line of EPR Spectrum.

$$\begin{array}{c} CH_3 \\ | \\ R-CH_2-C\cdot \\ | \\ COO(CH_2CH_2O)_3COC(CH_3)=CH_2 \end{array}$$
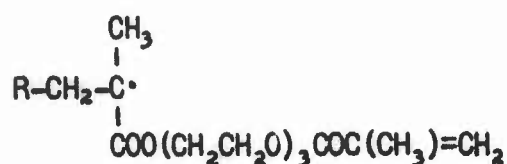
where R is the polymer chain. The quartet from the CH_3 group ($a^{CH_3} = 23$ G) is split by the two nearly equivalent methylene protons ($a^{CH_2} = 11$ and 14 G)[15] to give the observed 9-line spectrum; resolution of the even-numbered spectral lines is not achieved.

b. Line Shape and Broadening Mechanism

Table I-II shows that the central line of the monomer radical EPR spectrum does not widen appreciably at the highest microwave powers available from the klystron. The average line shape factor for this line was measured to be 2.3; 2.2 is the theoretical value for a pure Gaussian line.[17] These two results imply that the EPR line is broadened mainly by inhomogeneous mechanisms. The broadening is principally due to unresolved hyperfine interaction and to the nuclear spin state of the β-protons.[15] Analysis of progressive saturation curves (Figure I-1) by Castner's method results in a value of approximately 0.5 for his "a" parameter [Equation (3)]. Although Castner's method involves considerable uncertainty when "a" is as large as 0.5, it does indicate that the spin packet width is not negligible in comparison to the total linewidth.

c. Dose and Temperature Effects on Spatial Distributions of Radicals

Table I-I summarizes relaxation time as a function of radiation dose and of temperature for radicals trapped in tri-EDMAX gels. $(T_1T_2)^{1/2}$ has been determined by Portis' method as well as by Castner's method. Castner's

method has also been applied to the EPR central linewidths to calculate T_2
(Equation 3) separately. The data show that: (a) $(T_1T_2)^{1/2}$ and T_2 do not
change significantly with increasing radiation dose to 2 Mrad; and
(b) T_2 appears to increase upon going from 298°K to 77°K, whereas T_1 does
not change significantly.

Bullock and Sutcliffe[6] have made similar measurements on methyl-
methacrylate radicals and it is interesting to compare the results obtained
in this work for tri-EDMAX radicals which have a similar structure with
their results for radicals trapped in photopolymerized pure methylmethacrylate.
They obtain a value of 2.9×10^{-6} sec at 299°K for $(T_1T_2)^{1/2}$ by Castner's
method which compares favorably with the value 3.1×10^{-6} obtained in the
present work. Their values of 5.7×10^{-8} sec for T_2 and 2.5×10^{-4} sec for
T_1 are in fair agreement with $T_2 = 3.6 \times 10^{-8}$ sec and $T_1 = 2.7 \times 10^{-4}$ sec
obtained here. Their value of Castner's "a" parameter $\simeq 0.30$ and considering
the precision of the method is comparable to the value "a" $\simeq 0.5$ measured
in this work. It is clear from these comparisons that the relaxation
characteristics of trapped methylmethacrylate radicals are very similar
to those for the trapped radicals in tri-EDMAX gels. The EDMAX gels are
crosslinked while PMMA is not, and the mobility of segments is lower in the
EDMAX gels. These structural features apparently do not affect the
relaxation characteristics.

From 0.5 to 2.0 Mrad T_2 remains constant although the concentration
of radicals is increasing linearly in this dose range. In analogy to our
previous interpretations[2-5] this indicates that the radicals are trapped
in spurs and that the local radical concentration is higher than the average
radical concentration. These organic radicals exhibit the same relaxation

behavior as do trapped electrons in alkaline ices. At higher doses the value of T_2 should decrease due to overlap of spurs.

The value of Castner's "a" allows one to calculate the dipolar spin packet linewidth, $\Delta H_{ms}^{\perp}$, from Equation (4).

$$\Delta H_{ms}^{\perp} = \frac{a \Delta H_{ms}^{G}}{1.47} \tag{4}$$

Wyard[18] has modified Kittel and Abrahams'[19] treatment of dipolar linewidth to apply to non-equivalent magnetic centers in glassy and polycrystalline samples, and obtains $\Delta H_{ms}^{\perp} = 32 M$ where M is a local molarity of trapped spins contributing to the dipolar linewidth. The radicals in EDMAX gels may be equivalent in which case $\Delta H_{ms}^{\perp} = 48 M$; we shall use the value of 48 M to calculate the local spin molarity. The calculated local spin molarity is 0.037 M and is constant from 0.5 to 2 Mrad. Assuming $G(\text{radical}) = 4$ the average spin concentration at 2 Mrad is only 0.0084 M which is a factor of 5 less than the local spin molarity. A similar analysis on trapped radicals in polymethylmethacrylate also shows a ratio of local to average radical concentration greater than one.[7] The actual ratio of local to average spin molarity at a given dose depends on the quantitative validity of $\Delta H_{ms}^{\perp} = 48 M$ and on the precision of a, but it is certainly greater than one at doses up to 2 Mrad. This is completely consistent with the spur concept deduced from radiation dose effects.

The temperature data indicate that T_2 increases by 60% as the temperature is lowered from $299^\circ K$ to $73^\circ K$. This curious temperature dependence also is found for radicals in irradiated polymethylmethacrylate.[6] The increase in T_2 indicates that the local radical concentration is

decreased at lower temperatures. This could be related to contraction of adjacent polymer chains, but the magnitude of the effect is similar in linear polymethylmethacrylate and in cross-linked EDMA gels. The effect of a wider temperature range on T_2 needs to be studied before more speculation on the cause of the temperature dependence is warranted.

6. REFERENCES

1. A. Kuppermann, in "Chemical and Biological Actions of Radiations," $\underline{V}$, M. Haissinsky, Ed. (Academic Press, New York, 1961) p. 85.

2. J. Zimbrick and L. Kevan, J. Amer. Chem. Soc., 88, 3678 (1966).

3. J. Zimbrick and L. Kevan, J. Chem. Phys., 47, 2364 (1967).

4. J. Zimbrick and L. Kevan, Nature, 214, 693 (1967).

5. J. Zimbrick and L. Kevan, J. Chem. Phys., 47, 5000 (1967).

6. A. T. Bullock and L. H. Sutcliffe, Trans. Faraday Soc., 60, 2112 (1964).

7. A. T. Bullock, W. G. Griffiths and L. H. Sutcliffe, Trans. Faraday Soc., 63, 1846 (1967).

8. A. M. Portis, Phys. Rev., 91, 1071 (1953).

9. T. G. Castner, Phys. Rev., 115, 1506 (1959).

10. F. E. Hoecker and I. W. Watkins, Intl. J. Appl. Rad. and Isotopes, 3, 31 (1958).

11. F. E. Hoecker, Health Phys., 8, 381 (1962).

12. E. E. Schneider, M. J. Day and G. Stein, Nature, 168, 645 (1951).

13. R. E. Michel, F. W. Chapman and T. J. Mao, J. Chem. Phys., 45, 4604 (1966); see earlier references therein.

14. M. C. R. Symons, J. Chem. Soc., 1186 (1963).

15. H. Fischer, J. Poly. Sci., 82, 529 (1964).

16. P. Kourim and K. Vacek, Trans. Faraday Soc., 61, 415 (1965).

17. G. E. Pake and E. M. Purcell, Phys. Rev., 74, 1184 (1948).

18. S. J. Wyard, Proc. Phys. Soc., 86, 587 (1965).

19. C. Kittel and E. Abrahams, Phys. Rev., 90, 238 (1953).

B. PARAMAGNETIC RELAXATION OF TRAPPED ELECTRONS
IN γ-IRRADIATED ORGANIC GLASSES

1. INTRODUCTION

Recently we showed how paramagnetic relaxation experiments can give useful and semi-quantitative insights into the spatial distributions of trapped electrons and hydrogen atoms in frozen aqueous systems.[1-5] Radiation-produced electrons are also produced in organic glasses at $77^\circ K$ such as alcohols[6] and 2-methyltetrahydrofuran[7-9] (MTHF) and can be detected by optical and EPR spectroscopy. We report here the paramagnetic relaxation characteristics of trapped electrons in these organic glasses. The radiation dose dependence of the relaxation time gives information about spatial distributions, while the relaxation time magnitudes and the linewidths give information about the nature of the electron trapping site. A revealing correlation has been found between the size of the spatial inhomogeneities associated with radiation-produced trapped electrons and the polarity of the matrix.

2. EXPERIMENTAL

Reagent grade methanol, ethanol and MTHF were degassed on a vacuum line and dried over a freshly formed sodium film. Most methanol and ethanol samples were prepared as ~2 mm glassy spheres by dropping drops of the solution into liquid nitrogen; this involved a short exposure to air. MTHF samples were prepared by sealing into 3 mm o.d. Spectrosil quartz ampoules or by making glassy spheres without exposure to air. The latter was accomplished by pressurizing the vacuum line with dry nitrogen to

force out drops through a greaseless stopcock into liquid nitrogen; the short distance between the stopcock and the liquid nitrogen surface was purged with dry nitrogen.

Irradiations were carried out at $77^\circ K$ in a U. S. Nuclear Co^{60} γ-irradiator at a dose rate of 0.51 Mrad/hr as determined by ferrous sulfate dosimetry. For integral dose calculations the measured dose rate was corrected for radioactive decay.

The slow passage progressive saturation measurements were made as described before[2] at $73^\circ K$. Bubbling of liquid nitrogen was prevented by using a helium gas stream. Slow passage conditions were achieved by operating with a field modulation frequency of 40 hz and a typical modulation amplitude of 0.5 gauss. Progressive saturation curves were obtained by normalizing the EPR signal heights to a constant amplifier gain setting and plotting these heights versus microwave magnetic field, H_1. H_1 was measured as described previously.[2] Each sample using spheres utilized 3-5 spheres. Most samples were run in duplicate or triplicate.

3. RESULTS

The EPR spectrum of γ-irradiated methanol at $77^\circ K$ consists primarily of a triplet. This triplet is shown in Figure 1-3 and is due to the CH_2OH radical superimposed on a singlet due to e_t^-. Two small outer lines are also noted in the figure; these are split by 130 gauss and are due to the CHO radical. Their yield is very small. The CH_2OH radical spectrum has a theoretical 1:2:1 intensity ratio. The excess intensity in the center line is due to the trapped electron; this can be demonstrated by optical bleaching in the visible of the trapped electron line.[6] The radical spectrum was manually subtracted from the total spectrum to obtain the trapped
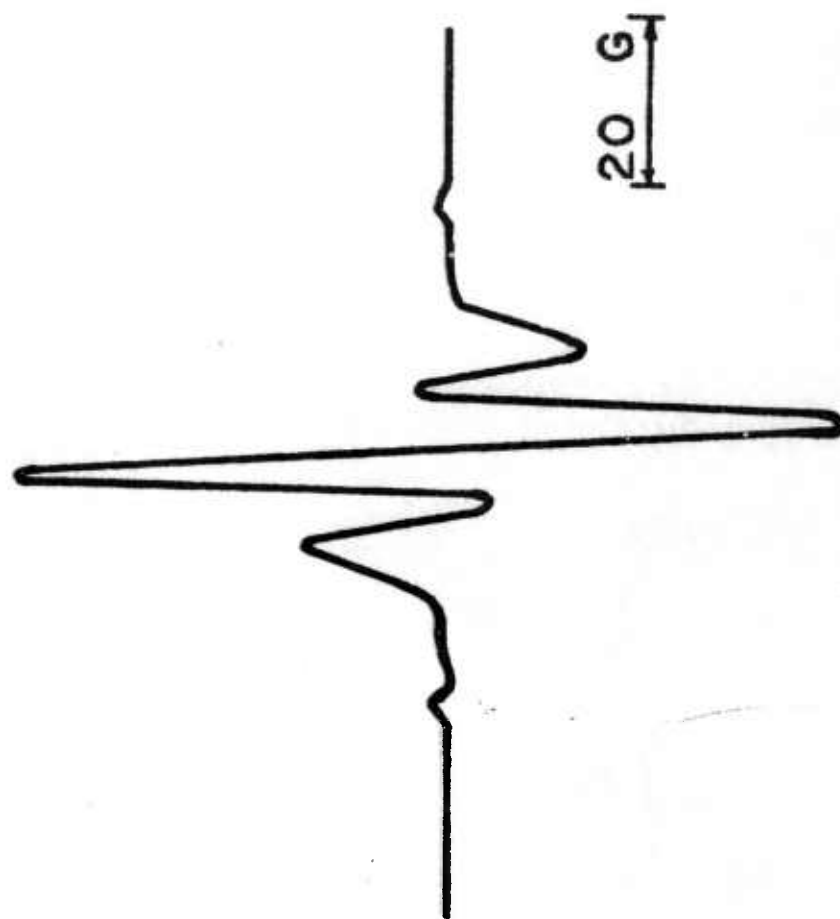
Figure 1-3. EPR spectrum of γ-irradiated glassy methanol at 73°K (dose 1.0 Mrad).

electron signal intensity as a function of microwave power. This procedure led to relatively consistent results although the accuracy is not high. The trapped electron line in methanol had a linewidth at maximum slope of 11 gauss and a line shape that was approximately Gaussian. Figure I-4 shows a typical power saturation curve for the trapped electron in methanol.

The relaxation times were calculated from the saturation curves by two methods. Method 1 was the Portis method in which ideal inhomogeneous broadening behavior was assumed.[10] The second method was Castner's analysis of the nonideal inhomogeneous broadening case.[11]

The EPR spectrum of γ-irradiated MTHF is shown in Figure I-5. The MTHF spectrum consists of a singlet e_t^- line superimposed on a 7-line radical spectrum. The 7-line radical spectrum has been interpreted as due to a free radical site at the number two carbon position. The hyperfine is then due to three methyl protons and one of the beta CH_2 protons with splitting constant A and the other beta CH_2 proton with splitting constant 2A to give relative intensities of 1:4:7:8:7:4:1. As can be seen in Figure I-5 the e_t^- line is much more intense than the underlying radical spectrum so that the radical spectrum can be easily and accurately subtracted from the total spectrum. Thus the results obtained for e_t^- in MTHF are much more accurate than those obtained for e_t^- in methanol. The trapped electron in MTHF had a linewidth at maximum slope of 3.8 ± 0.2 gauss and had a line shape parameter[2,12] of 2.2 which indicated that it was closely Gaussian. A typical power saturation curve for e_t^- in MTHF is shown in Figure I-6.[13] Note that the peak of the saturation curve in MTHF occurs at a value of H_1 five times lower than in methanol. The MTHF saturation curves were analyzed by both Portis' and Castner's methods.
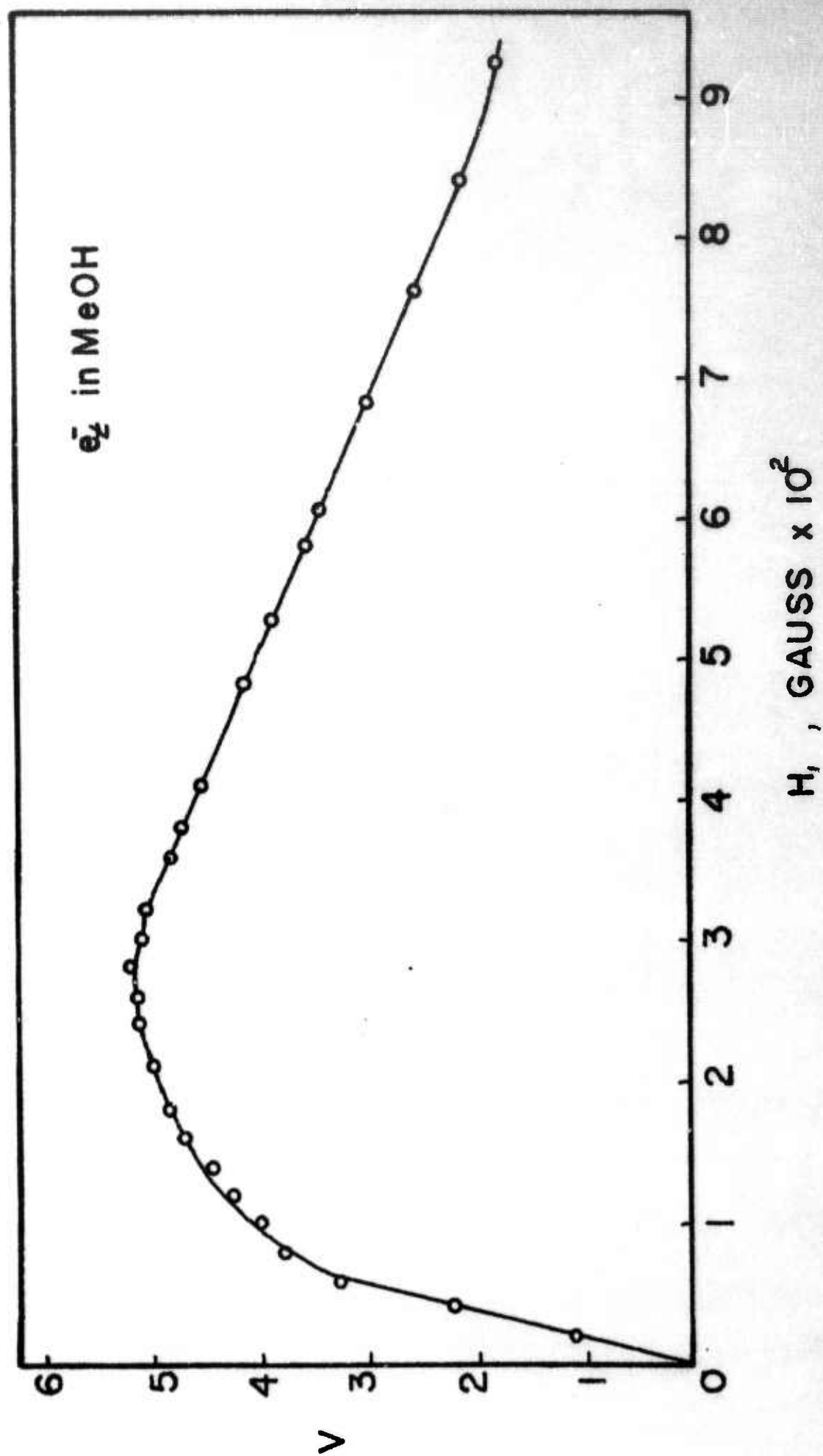
Figure 1-4. Slow passage power saturation curve for e_t^- in glassy methanol at 73°K (1.0 Mrad).
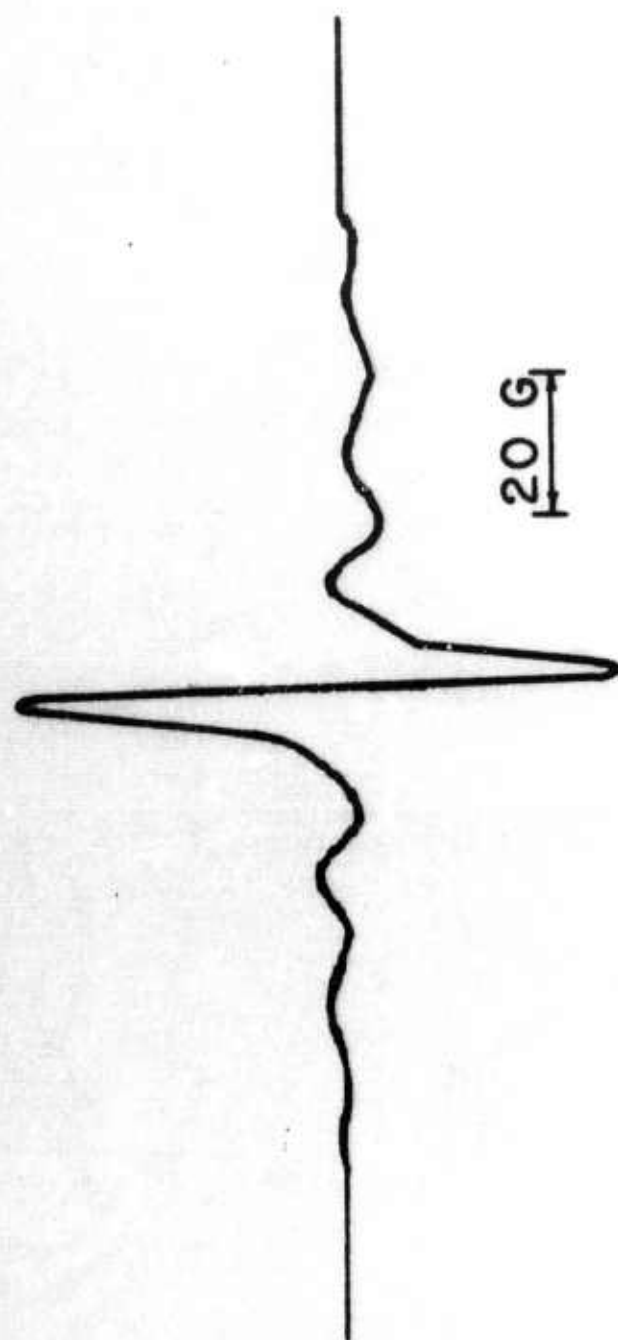
Figure 1-5. EPR spectrum of γ-irradiated glassy MTHF at 73°K (dose 0.5 Mrad).

e_z^- in MTHF

V

H , , GAUSS x10^2
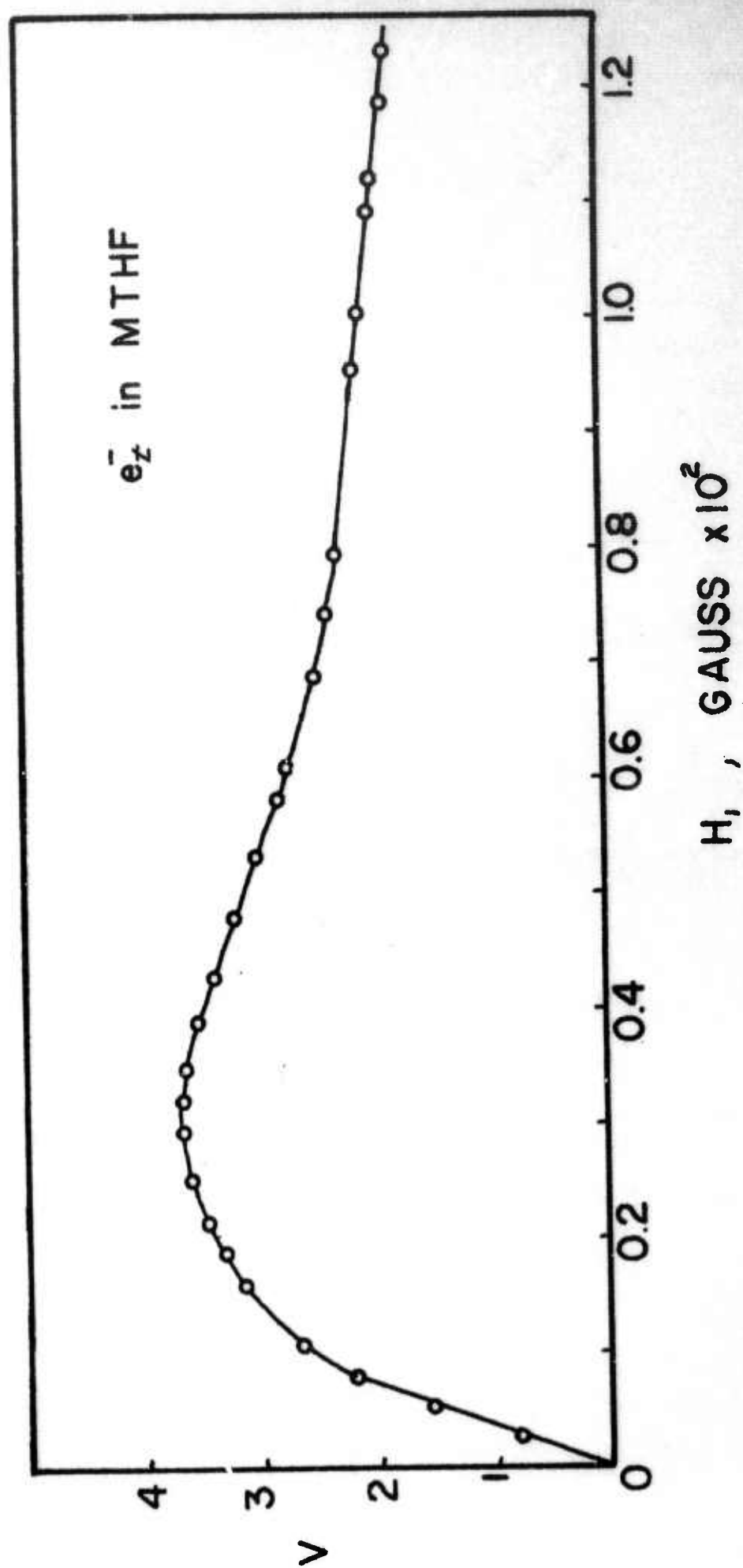
Figure 1-6. Slow passage power saturation curve for e_t^- in glassy MTHF at 73°K (0.5 Mrad).

24

A few experiments were also done on ethanol. It exhibits a 5-line
radical spectrum superimposed on a singlet trapped electron spectrum.
Saturation curves were obtained by subtracting the radical spectrum from the
total spectrum but the accuracy was not high. In general, the results in
ethanol paralleled those in methanol.

Table I-III summarizes the parameters determined for the trapped
electrons in the various matrices. Note that the relaxation times for the
electrons in the alcohols are about an order of magnitude smaller than the
relaxation times for trapped electrons in MTHF or in the sodium hydroxide
ice. All of the results in Table I-III are at doses low enough to be in
the dose independent region of the relaxation times.

Figure I-7 shows the variation of relaxation time versus radiation dose.
Determinations of T_2 show that the dose variation in $(T_1 T_2)^{1/2}$ is due
largely to variations in T_2. In Figure I-7, however, values of $(T_1 T_2)^{1/2}$
determined by Portis' method are plotted since they could be determined
for a greater number of samples. Note that the relaxation time for electrons
in methanol remains constant from 0.5 to 2.0 Mrad and then decreases. In
contrast, the relaxation time for electrons in MTHF remains constant only
from 0.1 to 1.0 Mrad before decreasing. Both of these contrast with the
results of trapped electrons in alkaline ices[2] in which the relaxation time
remains constant to about 4 Mrad dose. Figure I-8 shows relaxation data for
electrons in methanol extended to very high doses and also shows the total
spin concentration. The decrease in the relaxation time levels off at the
same dose at which the increase in the total spin concentration reaches a
plateau.

Table I-III. Parameters for Trapped Electron EPR Lines in Various γ-Irradiated Matrices at 73°K[a]

Matrix	Linewidth[b] (gauss)	Line Shape	Portis'[c] $(T_1T_2)^{\frac{1}{2}}$, sec	Castner's[d] $(T_1T_2)^{\frac{1}{2}}$, sec	Castner's $\underline{a}$	T_2, sec
10 M NaOH/H_2O[e]	13.6 ± 0.5	Gaussian	2.2 × 10⁻⁵	1.8 × 10⁻⁵	0.14	5.1 × 10⁻⁸
Methanol	11 ± 2	Gaussian	5.2 × 10⁻⁶	4.8 × 10⁻⁶	~0.4	1.8 × 10⁻⁸
Ethanol	13 ± 2	Gaussian	4.4 × 10⁻⁶	-	~0.4	1.5 × 10⁻⁸
Ethanol-d₆	5 ± 1.5	Gaussian	-	-	-	-
MTHF	3.8 ± 0.2	Gaussian	3.6 × 10⁻⁵	3.3 × 10⁻⁵	0.27	0.94 × 10⁻⁸

[a] 0.5 Mrad dose.

[b] ΔH_{ms}^{β}.

[c] Calculated according to Reference 10.

[d] Calculated according to Reference 11.

[e] Reference 2.
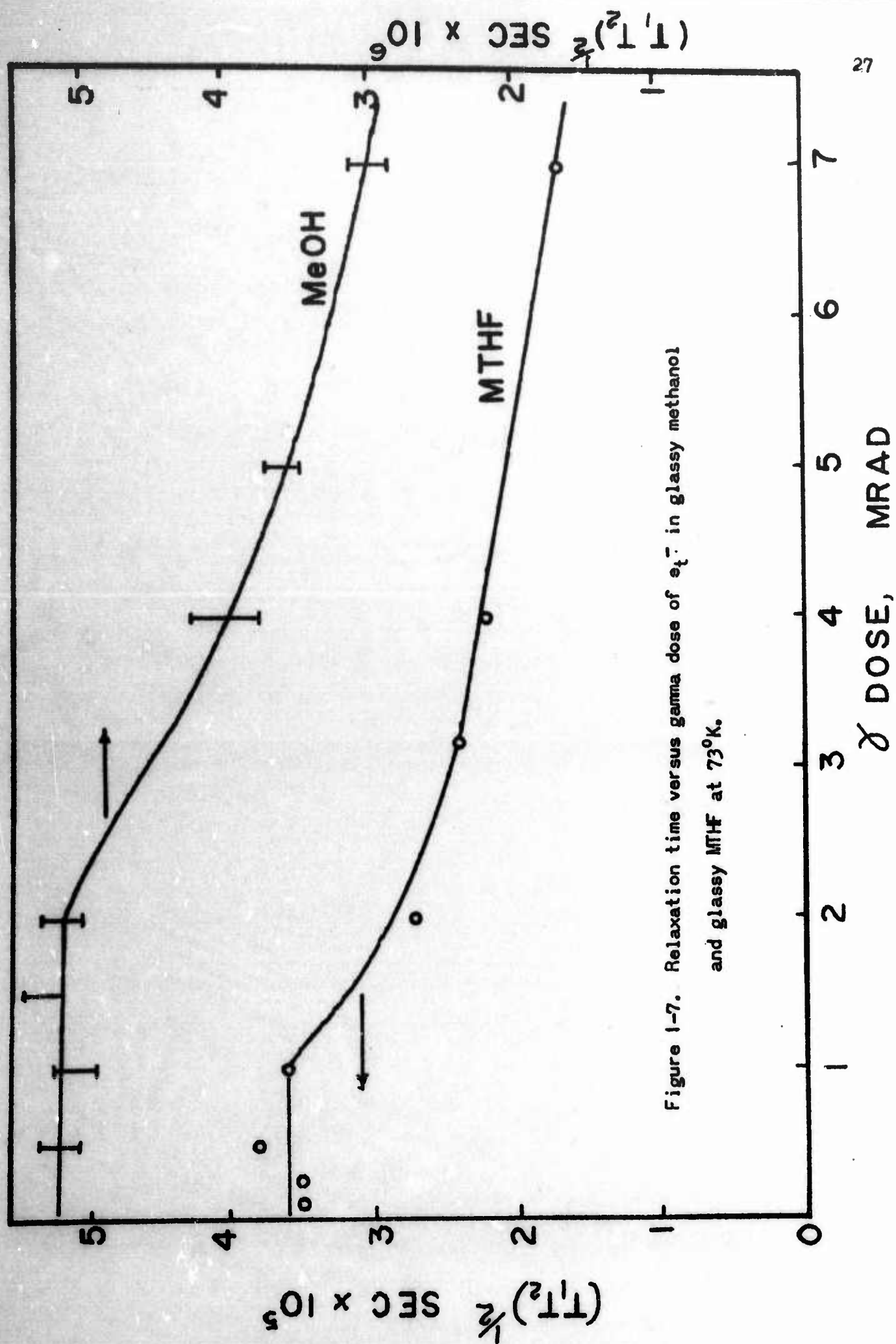
Figure 1-7. Relaxation time versus gamma dose of e_t^- in glassy methanol and glassy MTHF at 73°K.

Figure 1-8. Relaxation time of e_t^- in glassy methanol and total spin concentration in glassy methanol versus gamma dose at 77^0K.
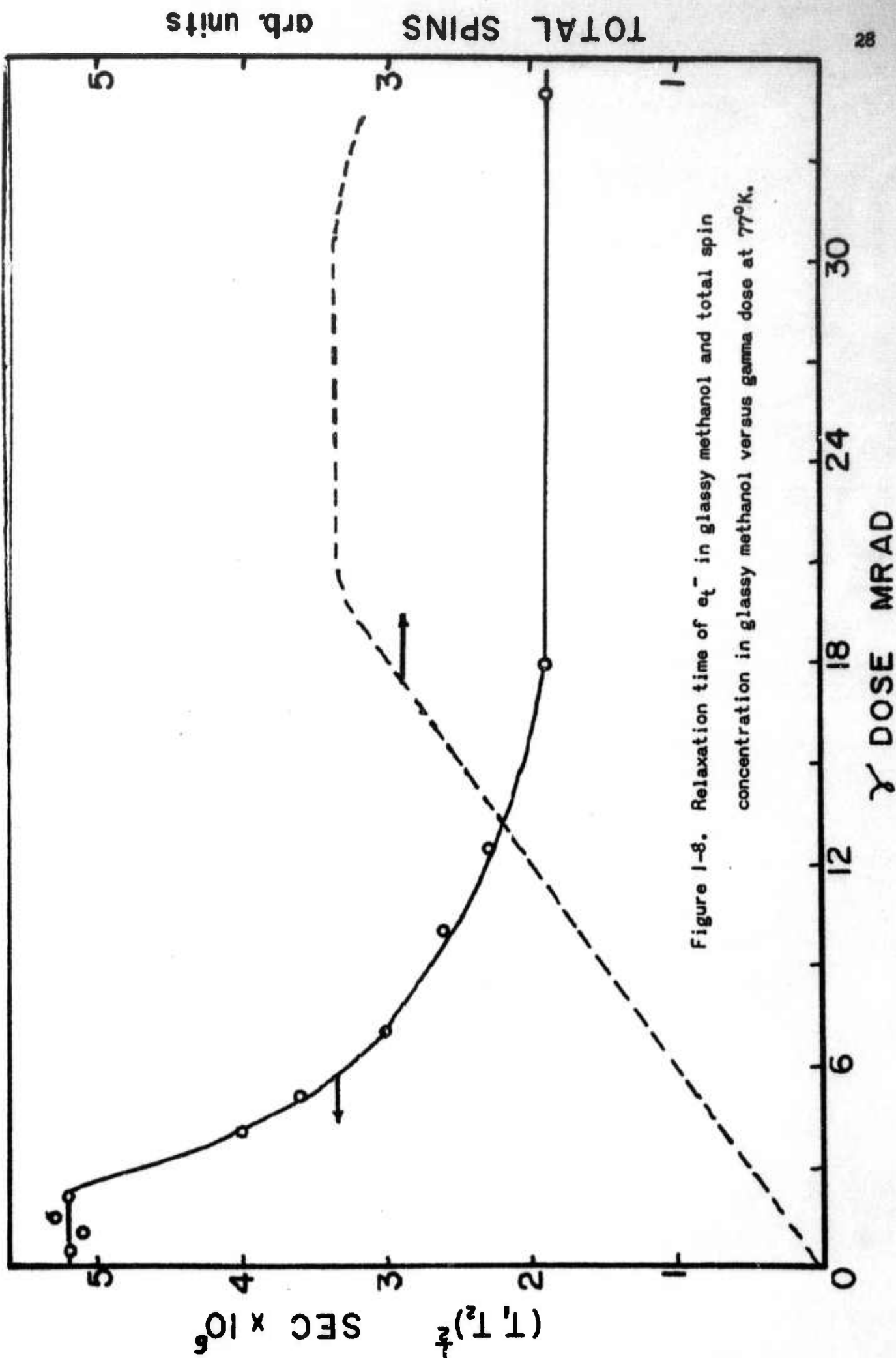
4. DISCUSSION

a. Line Shape and Broadening Mechanism

The line shape of e_t^- in MTHF fits a Gaussian function quite well according to both our data and the data of others.[9] This line shape is maintained at doses up to 6 Mrads; at higher doses it deviates slightly from a good Gaussian fit. The line shape of e_t^- in methanol and ethanol is also Gaussian. However, the fit cannot be determined precisely because of overlap with the CH_2OH radical. The e_t^- EPR linewidths in MTHF, methanol and ethanol do not increase appreciably during power saturation. At the higher microwave powers small increases in the e_t^- linewidths would be undetectable because of the increased size of the radical signal relative to that of e_t^-. However, it is clear that the e_t^- lines do not broaden with H_1 to the extent theoretically predicted for homogeneously broadened lines.

These two results imply that the e_t^- EPR lines are broadened mainly by inhomogeneous mechanisms. The shape of the power saturation curves in Figures I-4 and I-6 are consistent with this conclusion. Analysis of the saturation curves by Castner's method[11] give values of his a parameter of less than one which indicate that the spin packet width is not negligible compared to the total linewidth. The most likely inhomogeneous broadening mechanisms of importance are unresolved hyperfine interaction with surrounding protons and anisotropy broadening. The former mechanism can be evaluated semi-quantitatively from deuterated compounds.[4] The linewidth of e_t^- in ethanol-d_6 is about 5 gauss; a precise value cannot be obtained due to interference by the radical spectrum. Deuterated MTHF was not examined due to its prohibitive cost. Although quantitative analysis is not justified

the large linewidth decrease in ethanol-d_6 does indicate that unresolved hyperfine interaction is probably the dominant broadening mechanism.

b. Dose Effects on Spatial Distributions of e_t^- and Radicals

Studies in which relaxation time is measured as a function of radiation dose yield information about interactions between unpaired electron spins. For a uniform distribution of trapped species the average distance between them decreases with increasing radiation dose, and the spin-spin interaction becomes stronger. In this case T_2 is expected to decrease with increasing dose. This behavior is observed for trapped H atoms in acidic ices.[4] However, Figure I-7 shows that T_2 for e_t^- in polar organic glasses behaves somewhat differently. For e_t^- in MTHF and in methanol the dose variation in $(T_1 T_2)^{1/2}$ is due to a variation in T_2. The important result is that $(T_1 T_2)^{1/2}$ for e_t^- in methanol remains constant at 5.2×10^{-6} sec from 0.5 to 2.0 Mrad dose before decreasing. Similarly $(T_1 T_2)^{1/2}$ for e_t^- in MTHF remains constant at 3.6×10^{-5} sec from 0.1 to 1.0 Mrad before decreasing.

The constancy of $(T_1 T_2)^{1/2}$ over a given dose range indicates that e_t^- has spin-spin interactions with unpaired spins very close to it and only weakly interacts with other much more distant spins. This suggests that the spins are trapped in radiation-produced regions of inhomogeneity which we shall call spurs. At higher doses the spurs overlap and $(T_1 T_2)^{1/2}$ begins to decrease. Similar results and interpretation have been reported for e_t^- in alkaline ice.[2]

The inverse relationship between the variation in $(T_1 T_2)^{1/2}$ for e_t^- and the total spin concentration with radiation dose is demonstrated for methanol in Figure I-8. The total spin concentration includes e_t^- and CH_2OH

spins; since the EPR spectra of e_t^- and CH_2OH overlap both types of spins undergo relaxation with e_t^-. Note that as the total spin concentration reaches a limiting maximum value above 18 Mrad, the dose variation in $(T_1T_2)^{\frac{1}{2}}$ also reaches a limiting minimum value.

A semi-quantitative measure of the spur size may be obtained from the dose at which $(T_1T_2)^{\frac{1}{2}}$ begins to decrease. This dose is 1 Mrad in MTHF, 2 Mrad in methanol and about 4 Mrad in alkaline ice.[2] We assume that at these doses the spurs just overlap to fill the entire volume and that there are $G(e_t^-)$ electron spins per spur where G is the yield per 100 ev of absorbed radiation energy. Then the spur radius in angstroms is given by

$$r(\overset{o}{A}) = \left(\frac{4.8 \times 10^6}{4\pi D\rho} \right)^{\frac{1}{3}}$$

where ρ is the density and D is the dose in Mrad at which $(T_1T_2)^{\frac{1}{2}}$ begins to decrease. The calculated spur radii are 72 $\overset{o}{A}$ in MTHF, 59 $\overset{o}{A}$ in methanol and 42 $\overset{o}{A}$ in alkaline ice. This calculation leads to an overestimate of the spur radii, but the trend with matrix polarity is unambiguously shown by the experimental data. As the matrix polarity decreases from alkaline ice to methanol to MTHF the size of the spurs increases and the amount of spatial nonuniformity exhibited by the trapped radicals becomes less. In a nonpolar matrix like 3-methylpentane glass, trapped electrons produced by γ-irradiation are expected to show little if any evidence of spatial inhomogeneity. The correlation between spur size and matrix polarity implies that radiation-produced electrons travel further before being trapped the less polar the matrix. This suggests that the trapping cross section or the trap density for radiation-produced electrons is higher in more polar matrices.

The dependence of $(T_1 T_2)^{\frac{1}{2}}$ on radiation dose shows clearly but qualitatively that spatial inhomogeneity of trapped electrons and radicals exists. The absolute value of T_2 or equivalently, $\Delta H_{ms}^{\perp}$, the dipolar spin packet linewidth, allows one to calculate a local spin concentration to compare with the sample average spin concentration. The value of T_2 and $\Delta H_{ms}^{\perp}$ depend on the $\underline{a}$ parameter which is only accurate to about 30% for $\underline{a} > 0.2$. However, to the accuracy of $\underline{a}$, $\Delta H_{ms}^{\perp}$ may be calculated from Eqn. (1).[2]

$$\Delta H_{ms}^{\perp} = \frac{a \, \Delta H_{ms}^{G}}{1.47} \qquad (1)$$

The relation between the dipolar linewidth and the local spin concentration was given by Kittel and Abrahams[14] for single crystals and was modified by Wyard[15] to apply to non-equivalent magnetic centers in glassy and poly-crystalline matrices. Wyard obtains $\Delta H_{ms}^{\perp} = 32\,M$ where M is the total molarity of trapped spins contributing to the dipolar linewidth. The local molarity is then calculated from Eqn. (2) and the sample average molarity

$$M(\text{local}) = \frac{a \, \Delta H_{ms}^{G}}{32 \times 1.47} \qquad (2)$$

is calculated from Eqn. (3) where D is the dose in Mrad and ρ is the density.

$$M(\text{sample average}) = \frac{G(\text{total spins})D\rho}{900} \qquad (3)$$

The results for 1 Mrad total dose are summarized in Table I-IV. For each matrix M(local)/M(average) is greater than one which again indicates a non-uniform spatial distribution of trapped radicals.

Table I-IV. Spatial Distribution Data on Trapped Radicals
in Various γ-Irradiated Matrices at 73°K

Matrix	M(local) [a]	M(avg) [a]	$2G(e_t^-)$ [b]	ρ, g/cc [c]	$\dfrac{M(local)}{M(avg)}$ [a]	Dose Indep Range of $(T_1T_2)^{\frac{1}{2}}$ [a]	Spur Radius Å
10 M NaOH/H_2O	0.040	0.0061	4.2	1.3	6.6	4 Mrad	42
Methanol	0.094	0.0060	6	0.9	16	2	59
MTHF	0.022	0.0058	5.2	1.0	3.8	1	72

a Dose: 1 Mrad.

b Taken as G(total spins); this may be an underestimate for methanol.

c Estimated for solid phase.

5. REFERENCES

1. J. Zimbrick and L. Kevan, J. Am. Chem. Soc., **88**, 3678 (1966).

2. J. Zimbrick and L. Kevan, J. Chem. Phys., **47**, 2364 (1967).

3. J. Zimbrick and L. Kevan, Nature, **214**, 693 (1967).

4. J. Zimbrick and L. Kevan, J. Chem. Phys., **47**, 5000 (1967).

5. L. Kevan and D. H. Chen, J. Chem. Phys., **49**, 1970 (1968).

6. C. Chachaty and E. Hayon, Nature, **200**, 59 (1963).

7. M. R. Ronayne, J. P. Guarino and W. H. Hamill, J. Am. Chem. Soc., **84**, 4230 (1962).

8. G. A. Salmon, Disc. Faraday Soc., **36**, 284 (1963).

9. D. Smith and J. J. Pieroni, Can. J. Chem. **43**, 876 (1965).

10. A. M. Portis, Phys. Rev., **91**, 1071 (1953).

11. T. G. Castner, Phys. Rev., **115**, 1506 (1959).

12. G. E. Pake and E. M. Purcell, Phys. Rev., **74**, 1184 (1948).

13. Our curve is in substantial agreement with recent data of J. Lin, K. Tsuji and F. Williams, J. Am. Chem. Soc., **90**, 2766 (1968).

14. C. Kittel and E. Abrahams, Phys. Rev., **90**, 238 (1953).

15. S. J. Wyard, Proc. Phys. Soc., **86**, 587 (1965).

C. RADIATION-INDUCED CHARGE STORAGE IN ORGANIC POLYMERS

(with James Barnes)

1. INTRODUCTION

A distinguishing effect of high energy radiation on matter is that it produces ionization. This can be both desirable and deleterious. If the ions can be trapped and stored they represent potential stored energy. The efficiency and maximum amount of energy storage is partially dependent on the spatial distribution of the trapped species. This aspect was investigated in previous sections A and B. In this section we concern ourselves with fundamental investigations of factors that affect the utilization of stored energy in the form of ions. These factors include the detrapping mechanism and the conduction mechanism of the trapped charges.

Conduction mechanisms of trapped charges in polymeric systems, especially polymethylmethacrylate (PMMA), have been investigated and represent a continuation of the studies reported in the 1967 Annual Report.[1] Thermal heating is used to detrap the trapped charges in γ-irradiated polymers doped with electron traps. Conduction of these charges in a preferred direction was studied by application of a temperature gradient across the sample and by an applied electric field. The characteristics of thermoelectric currents generated by a temperature gradient in irradiated PMMA indicate that the positive charge becomes mobile when the carbomethoxy side groups of the polymer chain begin to rotate freely. This finding suggests that polymers with a prescribed 3-dimensional structure can be designed to allow charge storage to persist to quite high temperatures. Currents generated

by applied electric fields are less clearly understood and seem to be independent of the thermoelectric currents. Further work is aimed toward clarification of this point.

2. EXPERIMENTAL

Samples of commercial polymers were machined from cylindrical rods into discs, normally 2.5 cm in diameter and 1.0 cm thick. Attachment of the electrodes, irradiation procedure, current measurement apparatus and other experimental details have been described in the 1967 Annual Report.[1] Only new experimental details will be presented here.

Synthesized PMMA, both pure and with additives designed to act as electron or hole traps, was prepared by thermal polymerization of degassed, inhibitor-free methylmethacrylate (Rohm and Haas Co.). To avoid bubble formation the synthesized samples were prepared in small tubes and the typical sample size was 1.0 cm in diameter and 0.4 cm thick. The temperature cycle used for the thermal polymerization of MMA in this work consisted of an initial period at 90°C, a period of 60°C, followed by heating at 75°C, and 90°C. The initial temperature was maintained until the viscosity of the liquid, when hot, was like that of glycerine. The time necessary to reach this viscosity varied with the tube diameter and the length of time the monomer had been stored at room temperature prior to use. This normally ranged from 1 to 5 hours. The 60°C temperature cycle was maintained for approximately 16 hours followed by 6 to 8 hours at 75°C. Hardening at 90°C for approximately 16 hours completed the polymerization.

Figure 1-9 shows the circuit block diagram for the measurement of thermally-induced charge conduction in irradiated polymers under the influence
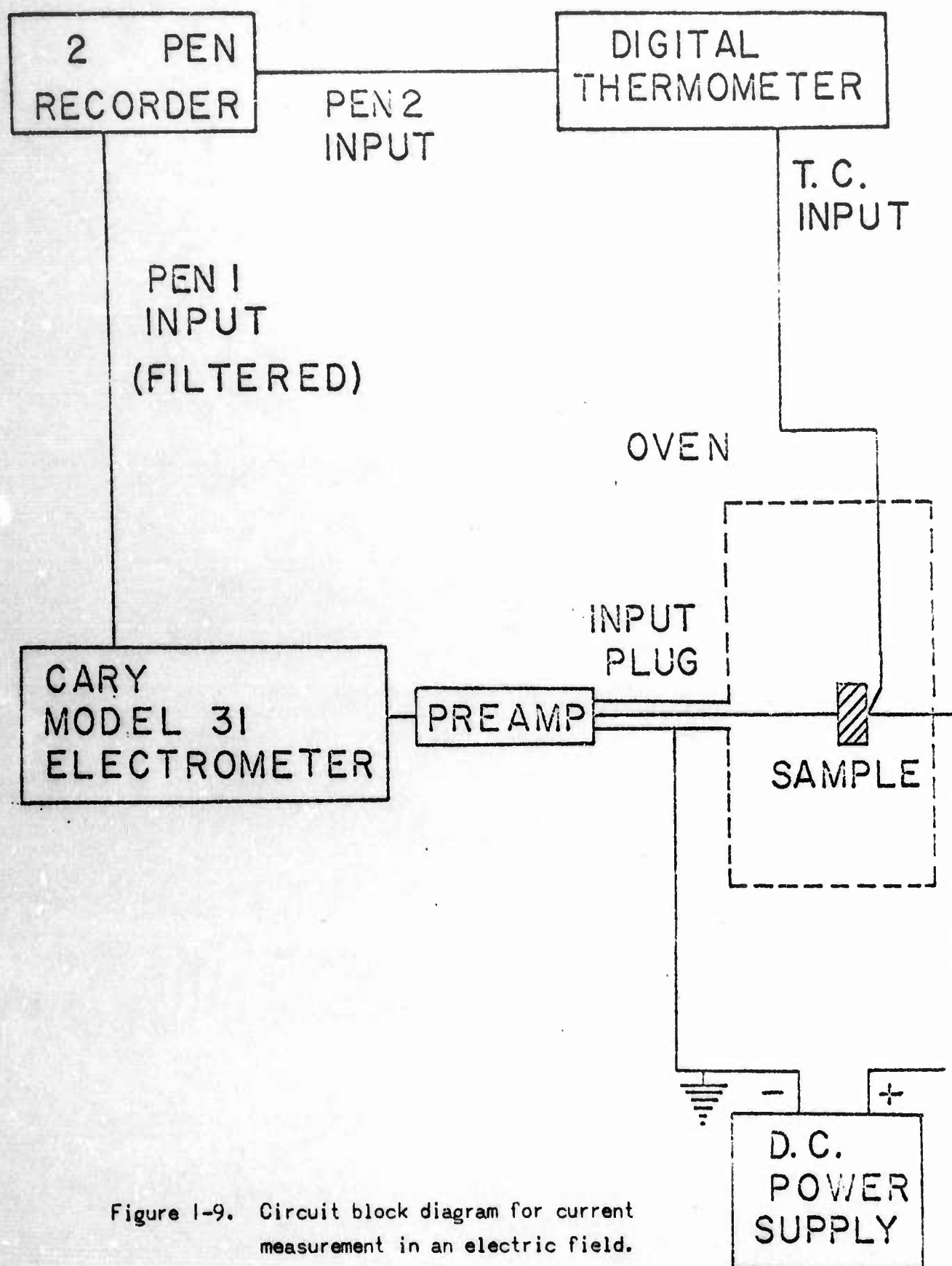
Figure 1-9. Circuit block diagram for current
measurement in an electric field.

of an electric field. The irradiated samples were heated in the absence of a temperature gradient. The electric field was applied by connecting a DC power supply between the right-hand electrode of the sample holder and the circuit ground. The power supply was a Keithly Model 240A High Voltage Supply with an output of 0 to 1200 volts. The polarity of the electric field will refer to the polarity of the right-hand electrode of the sample holder relative to ground.

In order to separate the effects of charge flow between the sample and the external circuit from internal charge movement, measurements were made with layers of insulating material placed between the sample and the sample holder electrodes. Glass microscope slides, 1 mm thick, were cut into squares (25 mm x 25 mm) and used as "blocking electrodes". One side of each square was made conducting by coating it with Eccobond solder. The tabs of each sample to be measured with blocking electrodes were broken off of the surface of the sample after irradiation. The samples were mounted in the sample holder with a blocking electrode on either side. Each blocking electrode was mounted with its conducting surface in contact with the electrode of the sample holder. Current measurements were then performed.

The electron paramagnetic resonance (EPR) measurements were made with a Varian V-4500 EPR system with 100 kc magnetic field modulation. Samples of Lucite and polyvinyl chloride (PVC) were cut from 1/8-inch diameter cylind- rical rod. Each sample was approximately 3 inches long, and was handled by a thin thread tied to one end. An absorbed dose of 0.5 Mrad was given to each sample before it was mounted in the EPR cavity. During measurement the samples were heated at a linear rate of $6^\circ C/min$ by circulating hot nitrogen gas through the EPR cavity. The gas was heated by passing it over a heating

coil. The rate of heating the sample was controlled by the rate of gas flow and the amount of current flowing through the heating coil. The temperature of the sample in the EPR cavity was measured with a Digitec Digital Thermocouple Thermometer. The thermocouple was placed on the surface of the sample and sensed a temperature slightly higher than the average temperature of the entire sample. EPR spectra were taken periodically throughout the heating cycle from 25°C to 100°C.

3. RESULTS

Most of our results on thermoelectric currents in Lucite including dose, decay and some chemical additive effects have been reported in the 1967 Annual Report.[1] A few additional results on Lucite are reported here together with new results on thermoelectric currents in PVC and in a few other polymers. Applied field and EPR results are presented on all systems studied.

a. Thermoelectric Current Measurement

Most of the measurements of the induced thermoelectric current in the organic polymers reported here were made on disk-shaped samples, 2.5 cm in diameter and 1.0 cm thick. The samples were irradiated to a level of absorbed dose of 0.5 Mrad and subsequently heated at a constant rate of 6°C/min. Unless stated otherwise these values should be assumed for all measurements.

Thermoelectric current curves for Lucite and PVC have been reported.[1] Figure I-10 shows the thermoelectric current for polystyrene. The curve is composed of a major peak of 1.1 picoamps (pa) at 115°C and a plateau of 0.3 pa between 60 and 80°C. The general shape of this curve is similar to that obtained from polystyrene in a study made by Hardtke[2] using a much larger temperature gradient.
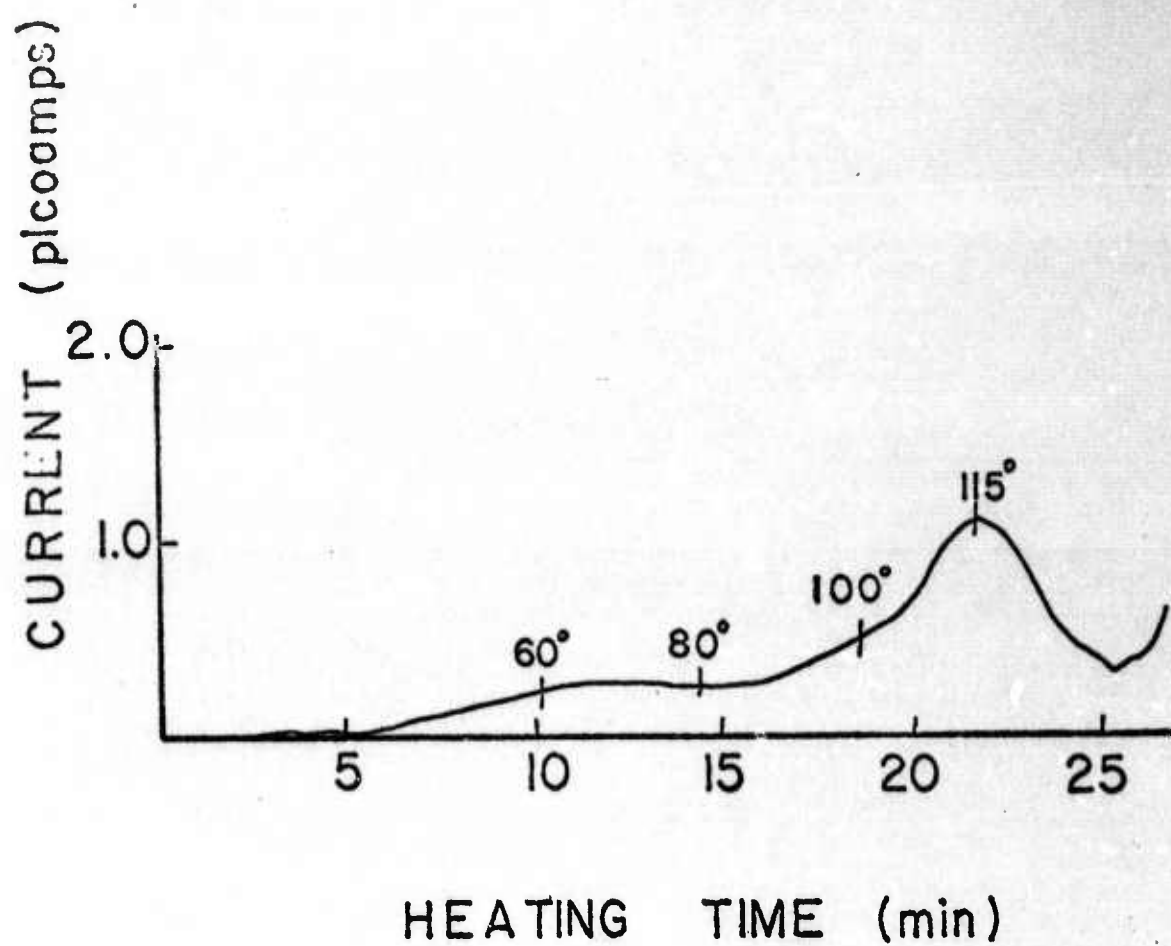
Figure I-10. Thermoelectric current plot for polystyrene.
Dose: 0.5 Mrad; Heating Rate: 6°C/min;
Sample Size: 2.0 cm dia. x 1.0 cm thick.

Samples of polyethylene and of Teflon were prepared, irradiated and heated. No measurable thermoelectric current was observed in repeated trials of either of these materials in the temperature range of 25 to 150°C.

b. Radiation Dose and Thermal Decay Measurements on PVC

Samples of PVC, 1 cm thick, were exposed to various doses of Co^{60} gamma-radiation and then heated in a temperature gradient to produce thermo-electric currents. Table I-V shows the results of measuring the currents generated in PVC after absorbing doses as high as 116 Mrad. The relationship between normalized total charge and exposure time is shown graphically in Figures I-11 and I-12 for two different dose ranges. Values of normalized total charge for exposure times to 1 hour (0.5 Mrad) are shown in Figure I-11 while data for exposure times to 22 hours (11 Mrad) are illustrated in Figure I-12. A combination of the curves in Figures I-11 and I-12 would consist of three linear segments with inflection points at absorbed doses of approximately 0.12 Mrad and 1.2 Mrad. Saturation of the trapped charge carrier population does not occur within the dose range studied.

The trapped charges in PVC are quite stable. Samples of PVC irradiated to 0.5 Mrad and stored at room temperature for 4 months showed no observable decrease in the normalized total charge release as shown in Table I-VI. Data from measurements of the thermoelectric current in PVC after the release of trapped charge carriers at various temperatures from 50 to 70°C are presented in Table I-VII. The stability of the charge trap appears to be constant to a temperature of approximately 60°C in PVC. This is illustrated in Figure I-13 where the normalized total charge measured in PVC samples after storage for a 5 hr period at various temperatures is plotted against temperature.

Table I-V. Effect of Absorbed Dose on the Thermoelectric

Current in PVC[a]

Exposure Time	Absorbed Dose	Peak Current	Temperature of Peak	Normalized Total Charge[b]
----	Mrad	picoamps	^{o}C	arbitrary units
5 min.	.04[d]	5.8	100	14
10 min.	.08	10.5	102	25
15 min.	.12	13.5	95	32
30 min.	.25	19	97	46
60 min.	.50	31	85	67
2 hr.	1.0	48	90	108
3 hr.	1.5	70	87	134
6 hr.	3	75	83	157
12 hr.	6	100	82	199
18 hr.	9	111	80	264
22 hr.	11	134	81	270
40 hr.	20	120	84	247
78 hr.	39	152	75	349
120 hr.	60	114	75	357[c]
	(two peaks)	64	103	
186 hr.	93	120	75	367[c]
	(two peaks)	90	93	
232 hr.	116	159	78	447[c]
	(two peaks)	129	93	

[a]Sample Size: 2.5 cm dia. X 1.0 cm thick, Heating Rate: $6^{o}C/min$

[b]Curves integrated to $120^{o}C$

[c]Normalized Total Charge of both peaks

[d]Underline indicates uncertainity
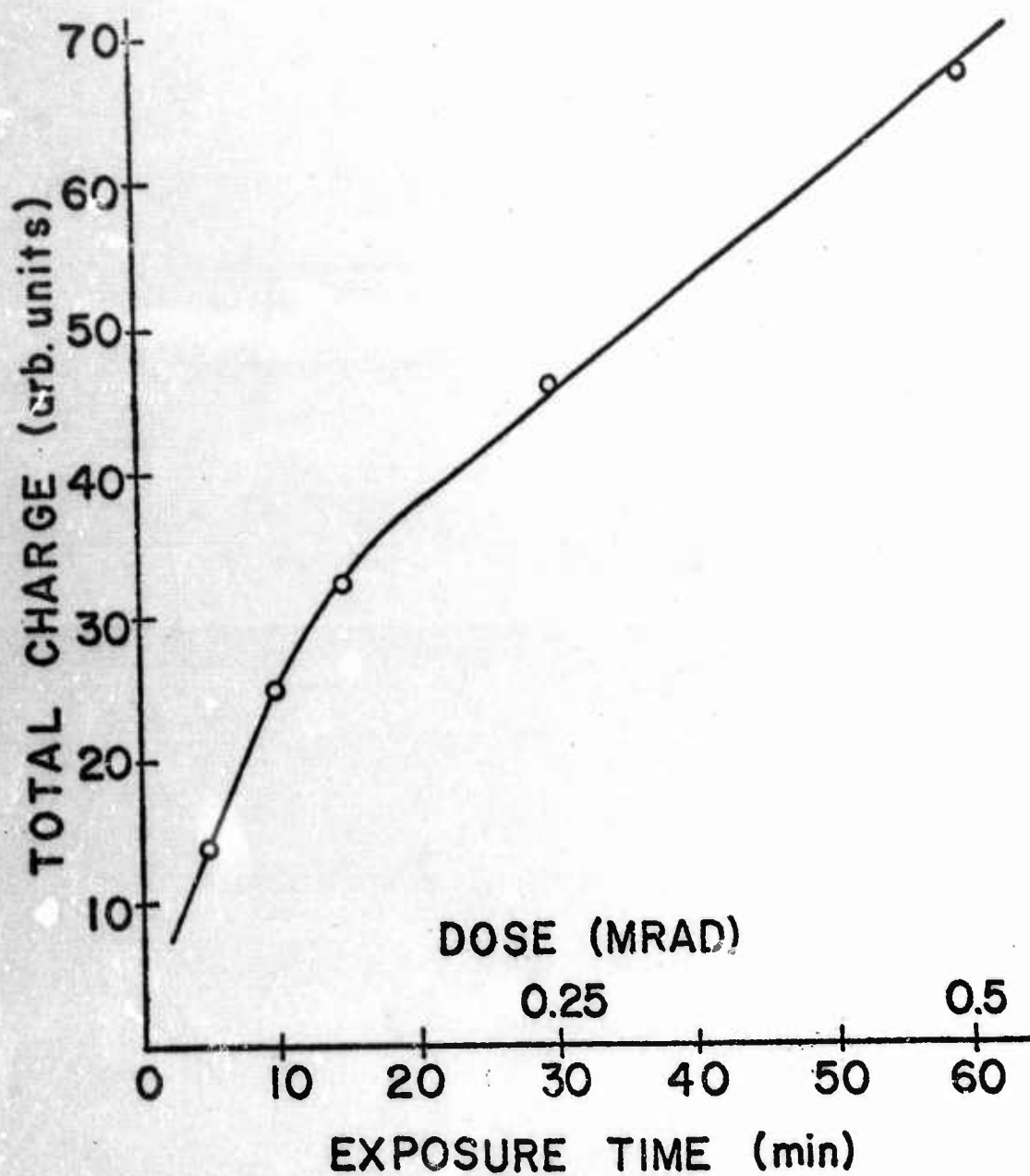
Figure I-11. Buildup of normalized total charge with gamma dose to 0.5 Mrad in PVC. Dose Rate: 0.5 Mrad/hr; Heating Rate: 6°C/min; Sample Size: 2.5 cm dia. x 1.0 cm thick.

Figure 1-12. Buildup of normalized total charge with gamma dose to 11 Mrad in PVC. Dose Rate: 0.5 Mrad/hr; Heating Rate: 6°C/min; Sample Size: 2.5 cm dia. x 1.0 cm thick.
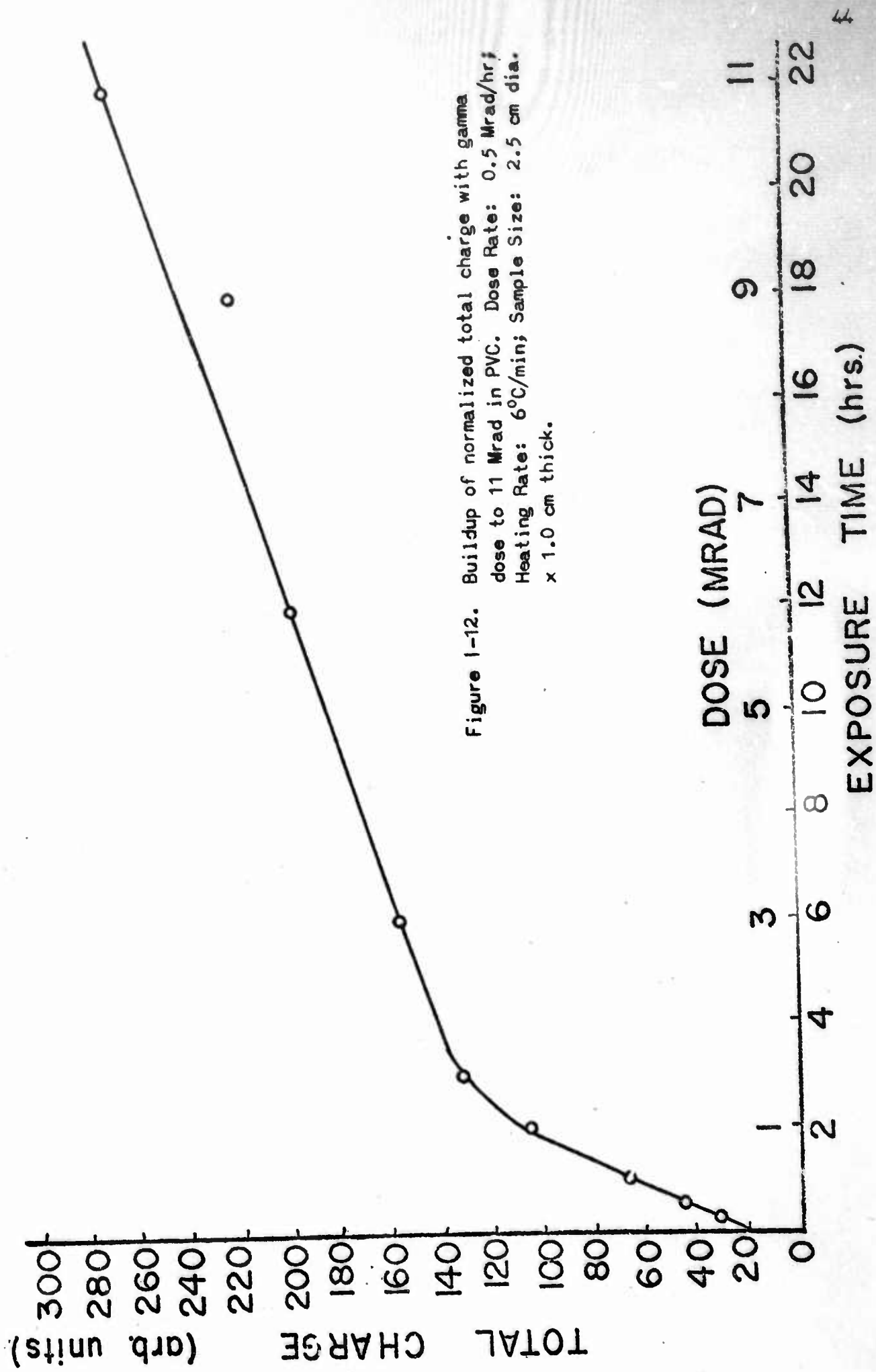
Table I-VI. Release of Trapped Charge Carriers
in PVC at 25°C [a]

Decay Time	Peak Current	Temperature of Peaks	Normalized Total Charge [b]
----	picoamps	^{o}C	arbitrary units
10 hrs.	28	86	56
25 hrs.	28	87	54
4 days	31	90	61
2 weeks	27	87	60
3 weeks	28	85	58
6 weeks	26	88	57
8 weeks	25	94	55
16 weeks	27	92	61

[a] Sample Size: 2.5 cm dia. X 1.0 cm thick, Absorbed Dose: 0.5 Mrad

[b] Curve integrated to 120°C

Table I-VII. Release of Trapped Charge Carriers

in PVC at Various Temperatures[a]

Decay Time	Peak Current	Temperature of Peak	Normalized Total Charge[b]
hours	picoamps	^{o}C	arbitrary
Temperature 50°C			
0	31	85	67
1	30	87	66
3	37	92	64
5	37	95	62
10	35	90	54
Temperature 60°C			
1	43	90	67
3	42	92	61
5	42	95	62
7.5	47	93	62
10	43	97	63
Temperature 65°C			
1	50	92	70
3	43	92	58
5	37	93	48
7.5	33	93	47
10	28	100	35
Temperature 70°C			
1	28	96	37
3.6	9.5	99	13
5	5.5	95	7

[a] Sample Size: 2.5 cm dia. X 1.0 cm thick, Absorbed Dose: 0.5 Mrad, Heating Rate: 6°C/min

[b] Curves integrated to 120°C
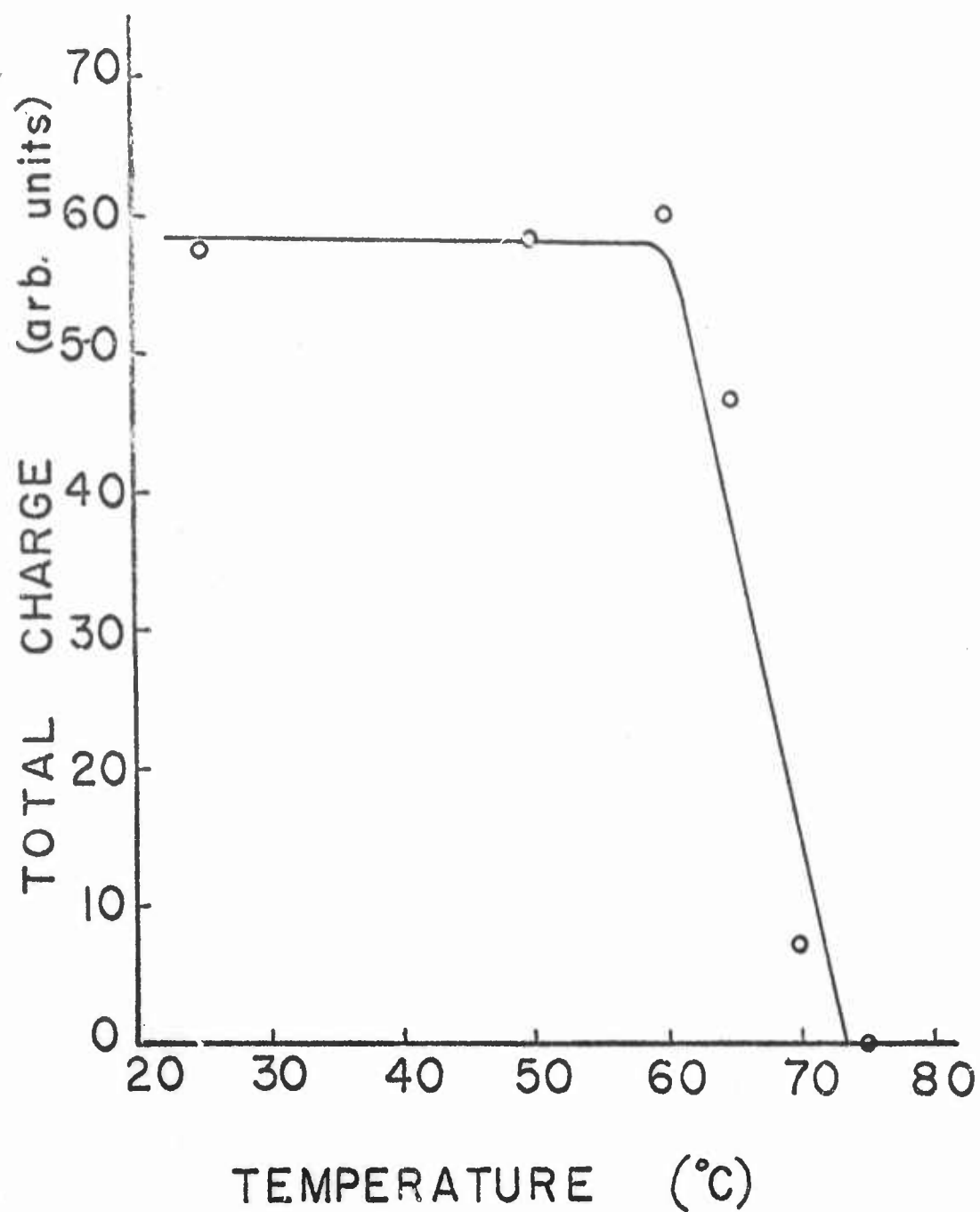
Figure I-13. Five hour release of trapped charge carriers at various temperatures in PVC. Dose: 0.5 Mrad; Heating Rate: 6°C/min; Sample Size: 2.5 cm dia. x 1.0 cm thick.

Virtually no release is observed after 5 hours at temperatures below 60°C. However, above 60°C the release rate increases very rapidly. Complete curves of trapped charge carrier release for temperatures from 50 to 75°C are shown in Figure I-14.

The release of trapped charge carriers in PVC follows a first-order rate equation. If the slopes of the curves of trapped charge carrier release at 60°C and above are determined and used to construct an Arrhenius plot, Figure I-15, an activation energy can be determined from the slope of the straight line. A value of 67 kcal/mole (2.9 ev) is obtained.

c. Effect of Blocking Electrodes on Thermoelectric Current

Glass blocking electrodes were used to distinguish the flow of charge between the sample and the external circuit from the internal movement of charge carriers within the sample. Lucite disks, 1 cm thick, were irradiated and the thermoelectric currents generated in the disks were measured with and without the presence of blocking electrodes. Curves of the same shape and, within experimental error, of the same magnitude were observed in samples measured with the blocking electrodes as was observed in samples measured without the blocking electrodes. This is evidence that the thermoelectric current is due entirely to a recombination of charge carriers within the volume of the sample.

d. Thermoelectric Currents in PMMA with Additives

Additives which could act as electron or hole traps were doped into synthesized PMMA to study their effects on the thermoelectric currents. Additive effects on photopolymerized PMMA have been reported previously.[1] The effect of several electron scavengers on the thermoelectric current

Figure 1-14: Release of trapped charge carriers at various temperatures in PVC.

Dose: 0.5 Mrad; Heating Rate: 6°C/min.;
Sample Size: 2.5 cm dia. x 1.0 cm thick.
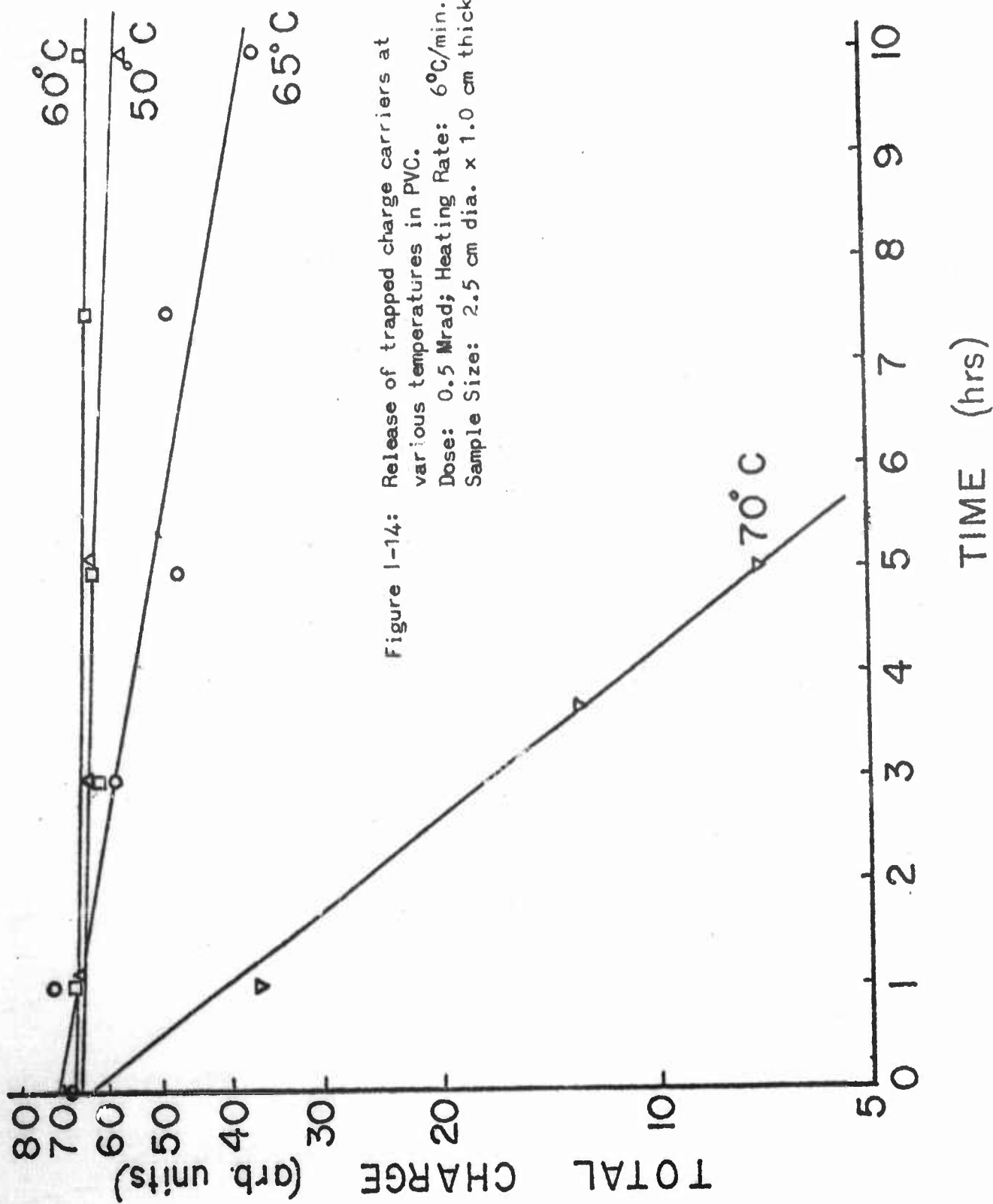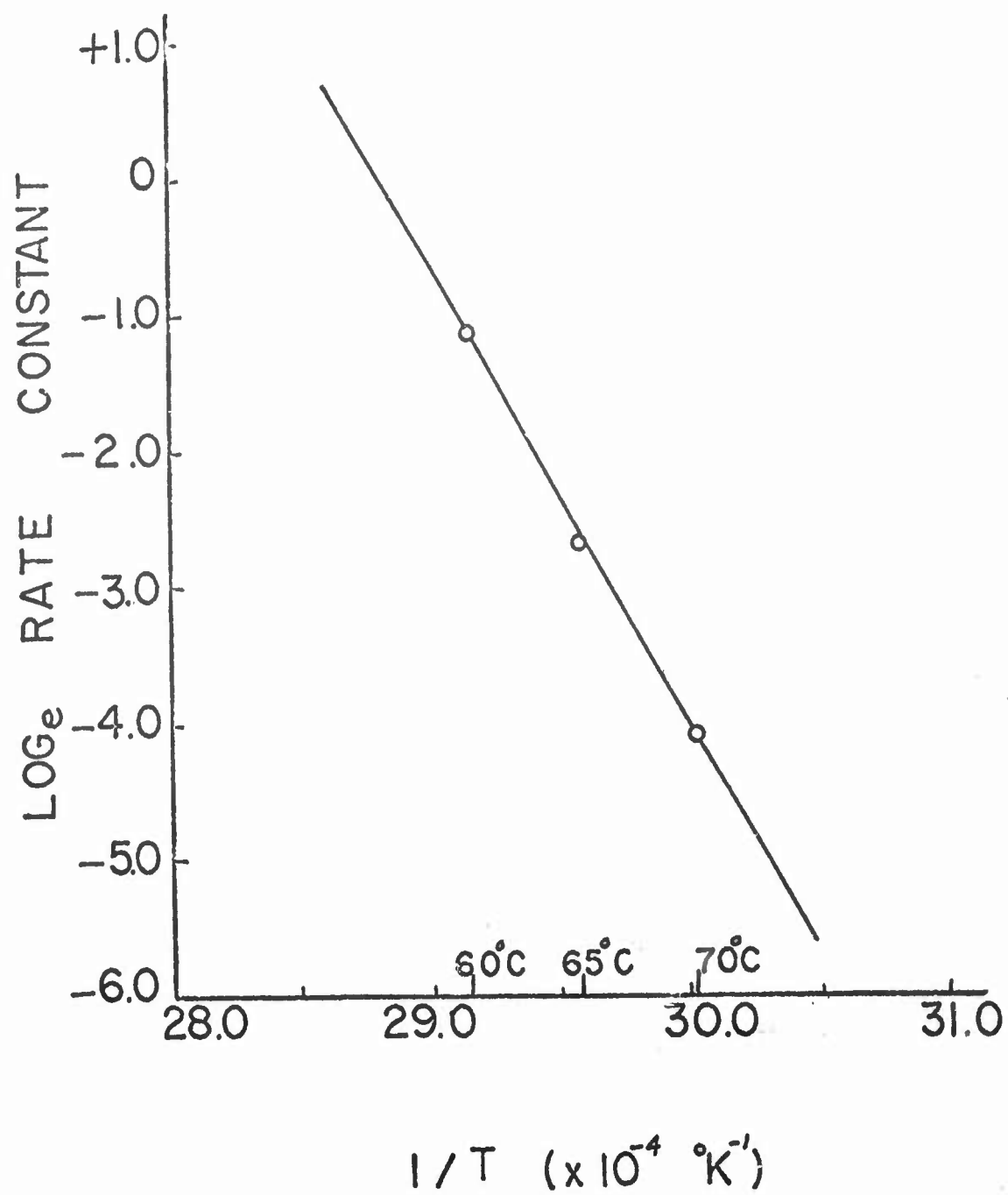
Figure I-15. Arrhenius plot for release of trapped charge carriers in PVC.

measured in thermally-polymerized PMMA are shown in Table I-VIII. The addition of biphenyl, CO_2, O_2 or azobisisobutyronitrile (AIBN) produces a significant increase in thermoelectric current measured in the synthesized polymer. AIBN is a compound which also functions as an initiator of polymerization in methyl methacrylate. Benzoyl peroxide added before polymerization likewise produces an increase in the thermoelectric current. Since benzoyl peroxide is a chemical initiator of polymerization commonly used in the commercial production of Lucite it must be at least one of the components responsible for the trapping of electrons and the subsequent generation of thermoelectric current in this commerical material.

The relative effects of the concentration of CCl_4 on the generation of charge carriers in a temperature gradient are shown in Table I-IX. All of these samples were thermally polymerized and then machined into disks 2.5 cm in diameter and 0.4 cm thick. The disks were irradiated to a dose of 0.5 Mrad prior to heating. The normalized total charge generated in the samples is plotted against CCl_4 concentration in Figure I-16. The initial large positive slope of the curve indicates that a very small concentration of CCl_4 has a large effect on the concentration of trapped charge carriers. The normalizeu total charge shows a linear dependence on CCl_4 concentration in the range of 2 mole % and 8 mole % but decreases significantly at a concentration between 8 and 12 mole %. The decrease at 12 % may be due partially to extraneous effects of the polymerization process since the scavenger concentration is so high.

Disks of PMMA, 1.0 cm in diameter and 0.4 cm thick, were prepared by thermally polymerizing MMA with various additives in conce. trations of 1 mole % and 4 mole %. The samples were irradiated to a dose of 0.5 Mrad

Table I-VIII. Effect of Electron Scavengers on Thermoelectric

Current in Thermally Polymerized PMMA[a]

Additive	Sample Thickness	Peak Current	Temperature at Peak	Normalized Total Charge[b]
(concentration)	cm	picoamps	^{o}C	arbitrary units
Biphenyl (1 mole %)	1.0	5.6	60	161
O_2 (saturated)	1.0	5.6	55	163
	1.0	5.9	57	174
CO_2 (saturated)	1.0	9.3	63	292
AIBN (saturated)	0.4 (two peaks)	5.6	63	192
		2.6	92	
CCl_4 (2 mole %)	1.0	3.0	55	92.1

[a]Sample Size: 2.5 cm dia., Dose: 0.5 Mrad, Heating Rate: 6^oC/min

[b]Curves integrated to 120°C

Table IX.   Effect of CCl_4 Concentration on Thermoelectric

Currents in Thermally Polymerized PMMA[a]

CCl_4 conc. mole %	Peak Current picoamps	Temperature At Peak °C	Normalized Total Charge[b] arbitrary units	Average Normalized Total Charge
0	1.5	66	38.3	
0	1.1	57	24.9	34.1 ± 6.1
0	1.5	60	39.0	
2	3.0	55	92.1	92.1
4	3.4	59	96.5	91.9 ± 4.6
4	3.1	60	87.3	
8	3.8	65	105.8	109.9 ± 4.1
8	3.9	60	114.1	
12	1.6	58	56.5	55.4 ± 1.1
12	2.1	61	54.3	

[a] All samples 2.5 cm dia. X 1.0 cm thick, Dose: 0.5 Mrad, Heating Rate: 6°C/min

[b] Curves integrated to 120°C
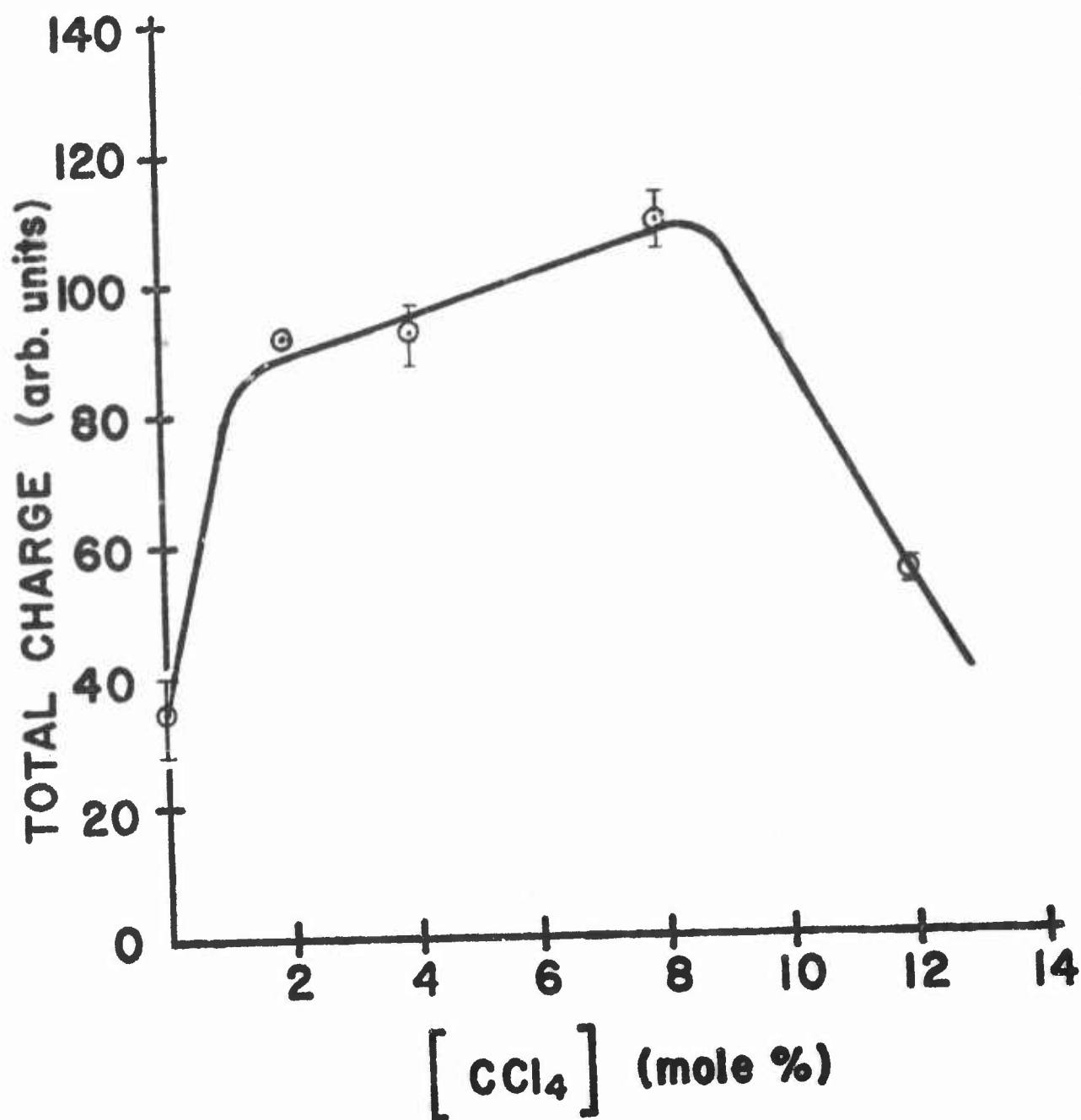
Figure I-16. Variation of normalized total charge vs. CCl_4 concentration in PMMA. Dose: 0.5 Mrad; Heating Rate: 6°C/min; Sample Size: 2.5 cm dia. x 1.0 cm thick.

and then heated to generate thermoelectric currents. The results of measuring
these currents are shown in Table I-X. Increasing the concentration of
CCl_4, biphenyl, and 2-methylpentene-1 by a factor of 4 increases the average
normalized total charge measured in each respective polymer by a factor of
approximately two. The values reported in Table I-X for measurements on
samples of PMMA containing CCl_4 are smaller than values reported for the same
materials in Table I-IX. This is because of the correspondingly smaller
diameter of the respective samples. The smaller diameter was used because
cylindrical sections without voids could be produced more consistently
during the polymerization process.

e. Thermally-Generated Currents in an Applied Electric Field

An investigation was made to determine how an electric field (E) would
influence the charge carriers generated as a result of heating a previously
irradiated organic polymer. The heating of all samples reported in this
section was carried out in a zero temperature gradient with the exception
of results on the combined effects of a temperature gradient and an electric
field.

(1) Electric Field Dependence

The results of applying a potential across a 1.0 cm thick
irradiated sample of Lucite, while heating the sample uniformly, are shown
in Figure I-17. The data for each curve was measured in a different sample
after the sample had been given a gamma dose of 0.5 Mrad. Electric fields
from 0 to 500 volts/cm are shown. Each of the curves contain a peak in the
temperature range of 100 to 115°C. This corresponds approximately with
the glass transition temperature for Lucite.[3] The curves do not return to
zero current but rather increase sharply above 120°C.

Table I-X. Effect of Various Additives at Different Concentrations on Thermoelectric Currents in Thermally Polymerized PMMA

Additive	conc mole %	Peak Current picoamps	Temperature At Peak °C	Normalized Total Charge[b] arbitrary units
None	----	0.2	57	6.7
	----	0.3	52	8.6
CCl$_4$	1	0.7	61	19.9
	4	1.7	60	51.2
	4	1.5	62	40.9
biphenyl	1	0.7	60	18.7
	1	0.9	58	25.6
	4	1.6	60	47.2
	4	1.5	62	
2-MP-1	1	0.5	61	13.7
	1	0.6	62	15.3
	4	.9	65	25.8
	4	1.2	68	30.5
CCl$_4$-1 mole % and 2-MP-1	1	1.4	64	38.0
	1	1.3	58	35.6
	4	1.2	60	28.2
	4	1.1	62	36.6

[a]Sample Size: 1.0 cm dia. X 1.0 cm thick, Dose: 0.5 Mrad, Heating Rate: 6°C/min

[b]All curves integrated to 120°C

Figure 1-17. Thermally generated current profiles of irradiated Lucite samples in various electric fields. Dose: 0.5 Mrad; Heating Rate: 6°C/min; Sample Size: 2.5 cm dia. x 1.0 cm thick; Zero Temperature Gradient.
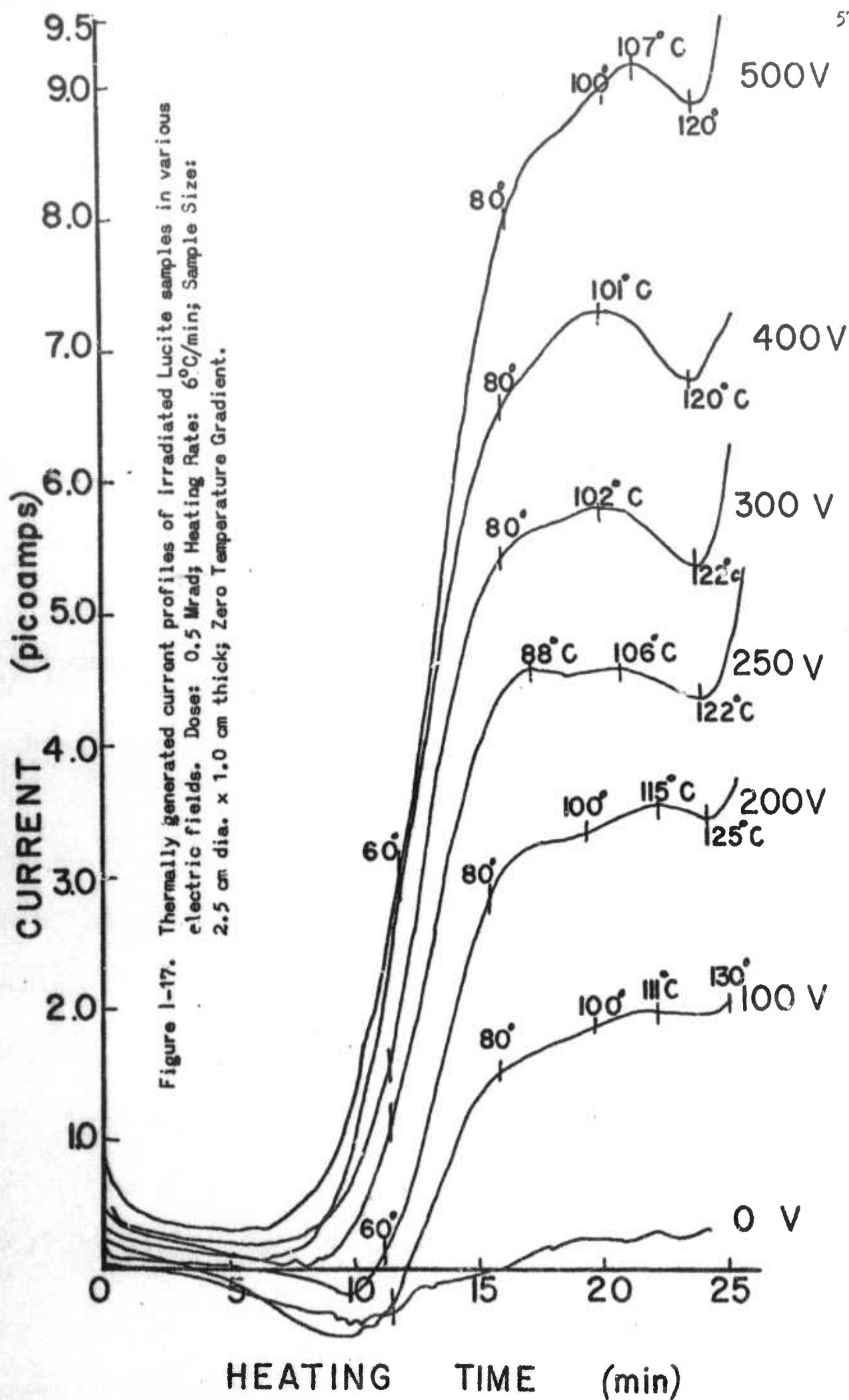
The measurement of background current in an unirradiated Lucite sample during heating in an electric field is shown in Figure I-18 for electric fields of 90 and 500 volts/cm. This background current shows a significant increase at temperatures above $90^{\circ}C$. Background current measurements made for values of E between 90 and 500 V are intermediate to the curves for these two values.

In order to separate the radiation-produced effect from the background current, it is necessary to subtract the background current from the curves shown in Figure I-17. This is illustrated for the 90 and 500 V/cm curves in Figure I-18. The result of this correction is to define the peak of the curves better and to give them a more uniform shape. The corrected curves are shown in Figure I-19. The temperature at the peak after the correction for background current has been made is approximately $100^{\circ}C$.

The current peak height is presented as a function of the applied electric field (E) in Figure I-20. There is a linear relation between these two factors for values of E to 1000 V/cm. This indicates that the current is ohmic.

(2) Radiation Dose Dependence

Figure I-21 presents an illustration of the effect of accumulated exposure to the gamma-flux on the growth of charge carrier movement. Exposure times from 0 minutes (background current only) to 60 minutes are shown. This corresponds to absorbed doses from 0 to 0.5 Mrad. An electric field of +300 V/cm was applied for each measurement. The curves are not corrected for background current. The integrated current versus dose data is given in Figure I-22 and Table I-XI for exposure periods up to 4 hours (2 Mrad). The normalized total charge reaches approximately 95% of

Figure 1-18. Background currents in unirradiated Lucite samples and correction of measured current profiles. Dose: 0.5 Mrad; Heating Rate: 6°C/min; Sample Size: 2.5 cm dia. x 1.0 cm thick; Zero Temperature Gradient.
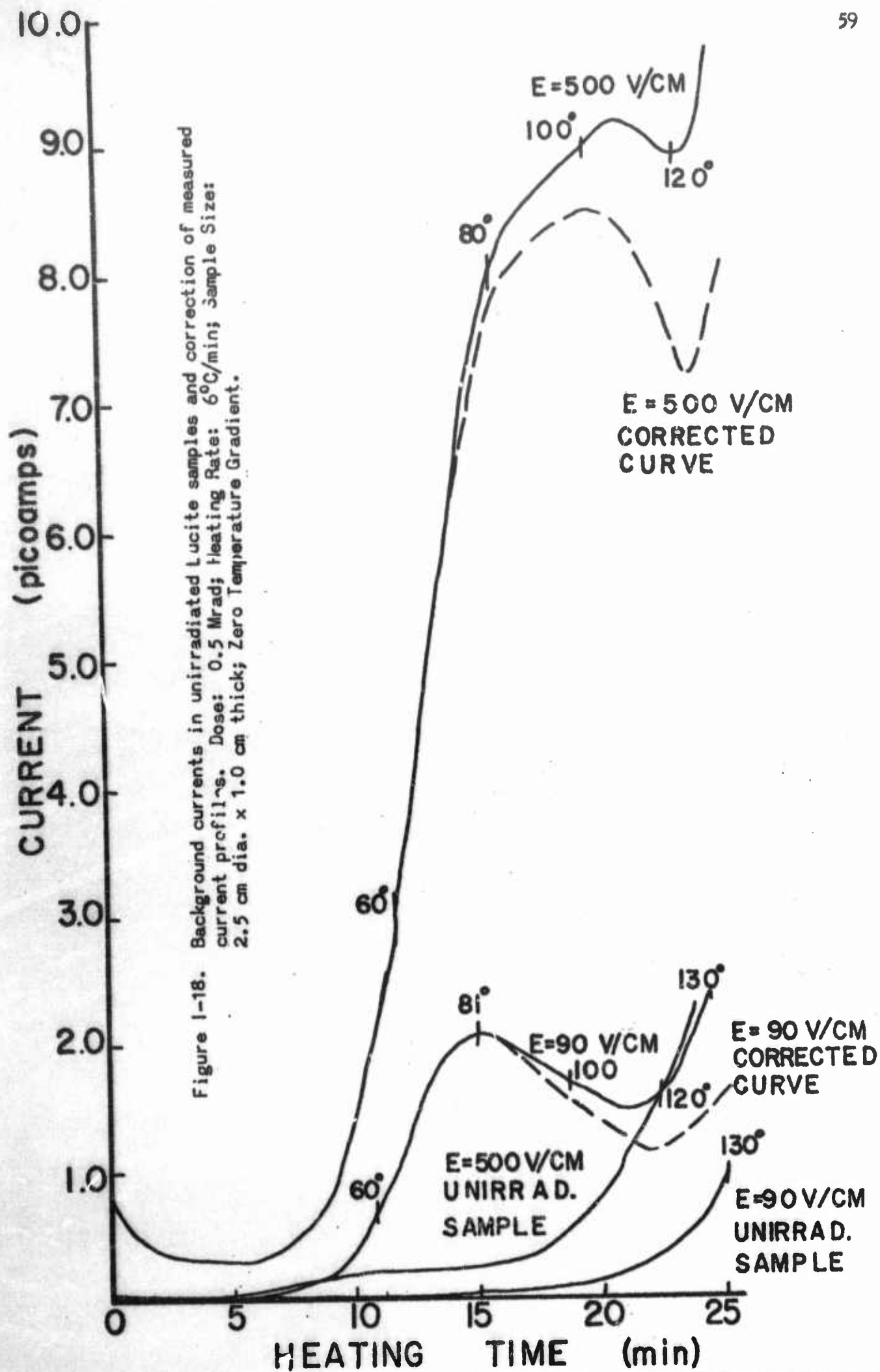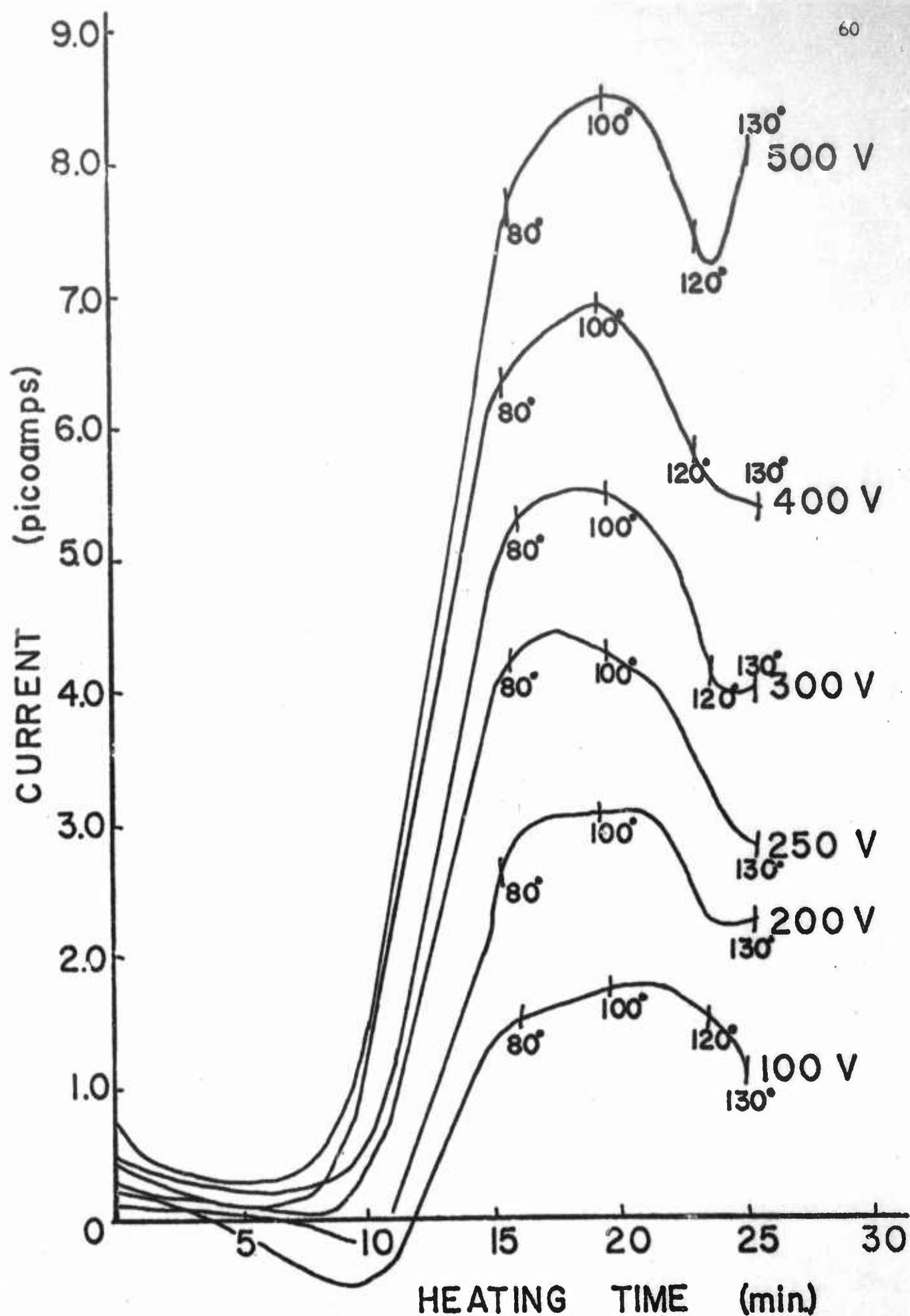
Figure I-19. Thermally generated current profiles corrected for background current. Dose: 0.5 Mrad; Heating Rate: 6°C/min; Sample Size: 2.5 cm dia. x 1.0 cm thick; Zero Temperature Gradient.

Figure 1-20. Electric field vs. maximum current in Lucite. Dose: 0.5 Mrad; Heating Rate: 6°C/min; Sample Size: 2.5 cm dia. x 1.0 cm thick; Zero Temperature Gradient.
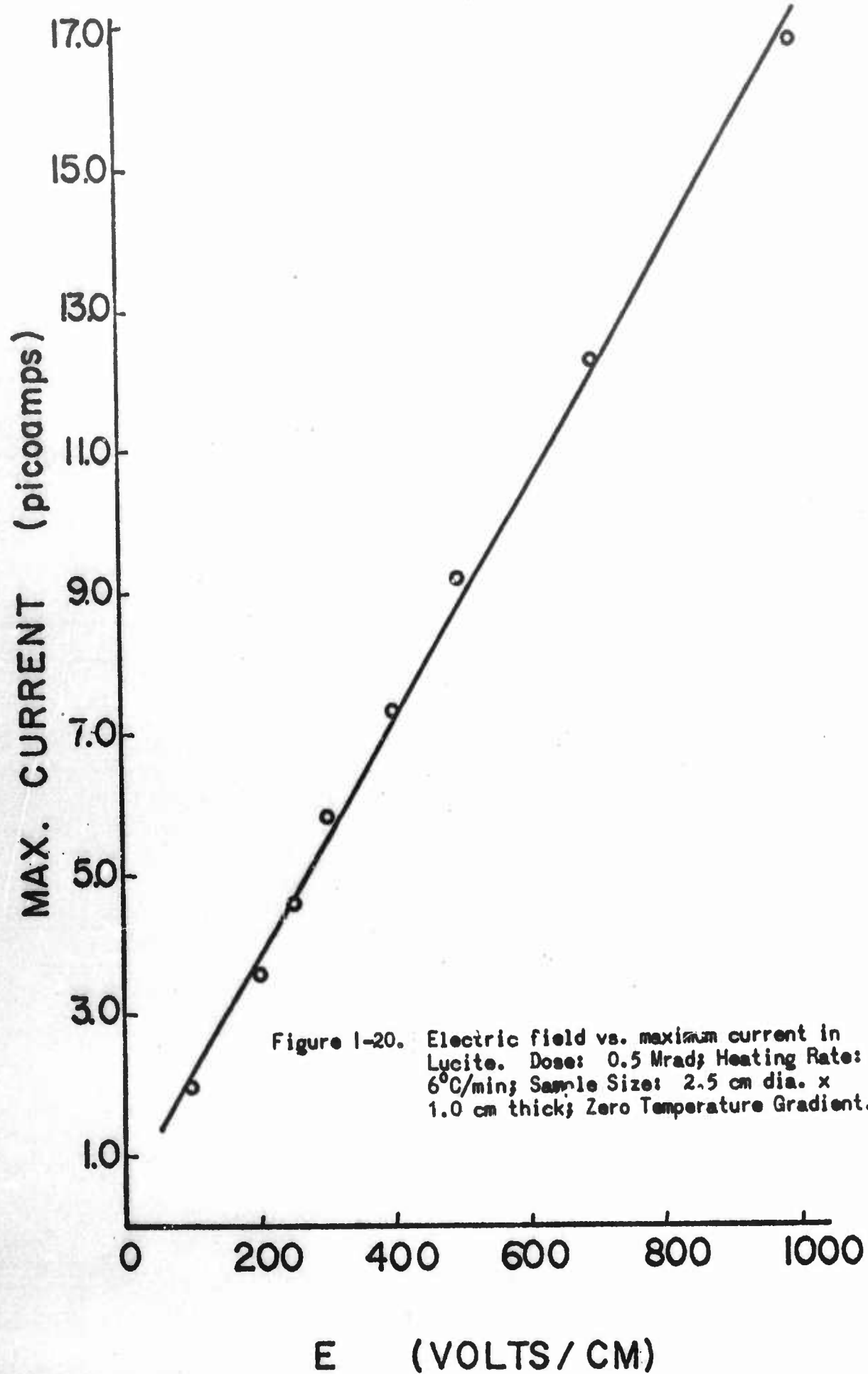
Figure I-21. Thermally generated current profiles in a 300 V/cm field for doses below saturation in Lucite. Dose Rate: 0.5 Mrad/hr; Heating Rate: 6°C/min; Sample Size: 2.5 cm dia. x 1.0 cm thick; Zero Temperature Gradient. Curves labeled for exposure time in minutes.
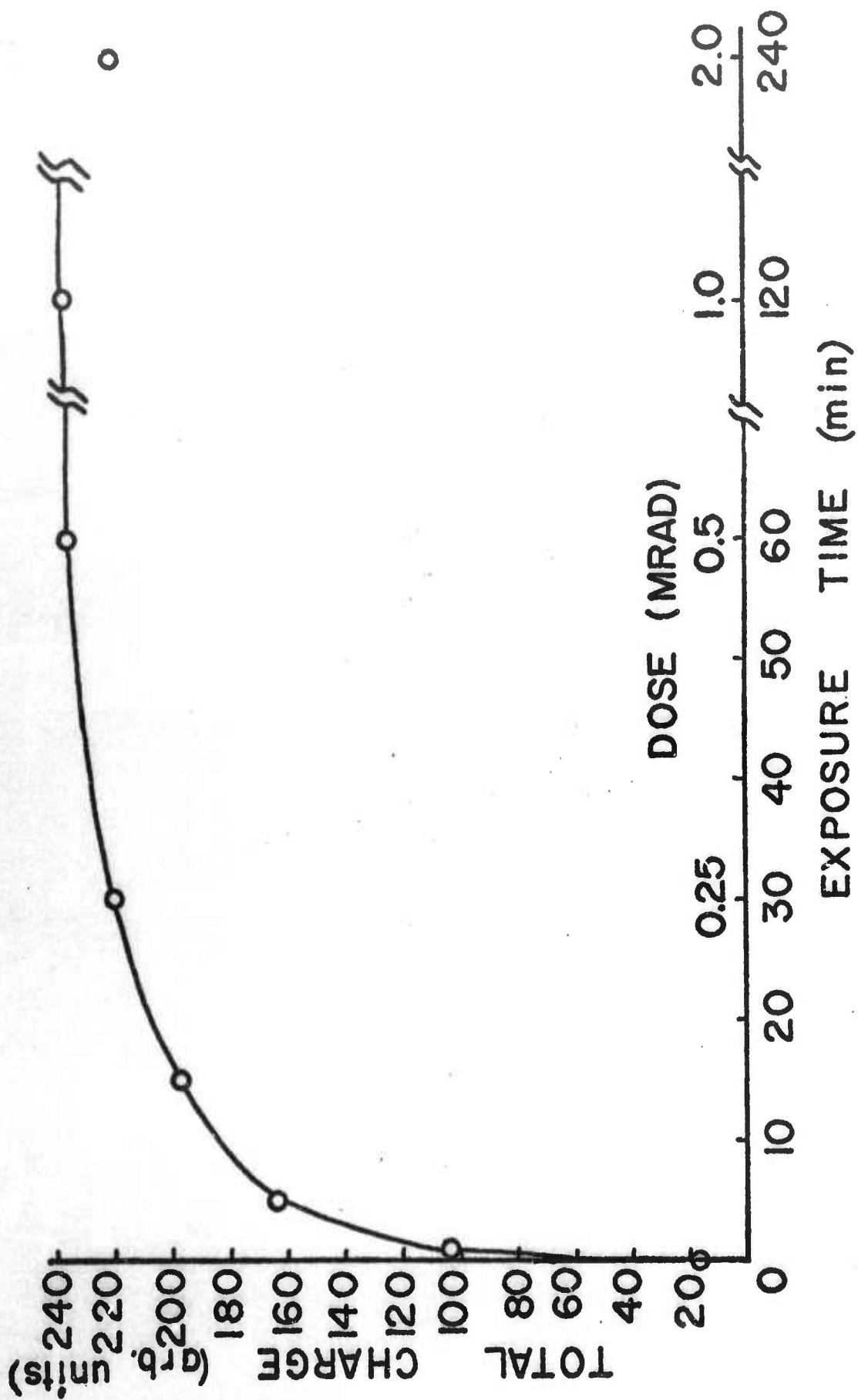
Figure 1-22. Saturation of normalized total charge with dose for a 300 V/cm field in Lucite. Dose Rate: 0.5 Mrad/hr; Heating Rate: 6°C/min; Sample Size: 2.5 cm dia. x 1.0 cm thick; Zero Temperature Gradient.

63

Table I-XI. Effect of Absorbed Dose on Thermal-Induced Charge
Conduction in an Electric Field[a]

Exposure Time	Absorbed Dose	Peak Current	Temperature of Peak	Normalized Total Charge[b]
----	Mrad	picoamps	^{o}C	arbitrary units
1 min.	0.01	3.6[b,c]	110	103
5 min.	0.04	4.7[b,c]	112	164
15 min.	0.12	5.2	106	198
30 min.	0.25	5.5	101	220
1 hr.	0.5	5.7	88	236
2 hr.	1.0	5.2	90	237
4 hr.	2.0	5.5	98	220

[a]Lucite sample, Electric Field: + 300 V/cm, Sample Size: 2.5 cm dia. X 1.0 cm
thick, Heating Rate: $6^{o}C$/min

[b]Curves integrated to $120^{o}C$

[c]inflexion only

saturation at a dose of 0.25 Mrad. This is to be compared with a dose of 1.0 Mrad for the saturation of normalized total charge under the influence of a temperature gradient.

(3) Polarization Effect in Lucite

During successive measurements of the background current in the same electric field it was discovered that there was a distinct reproducible difference in this current if the electric field was applied across the sample while the disk was being cooled from $120^{\circ}C$ to room temperature. Figure I-23 shows the results of five successive measurements made on the same unirradiated Lucite sample with an applied field of 500 V/cm. The only difference in the five trials is whether the 500 V was applied during the cooling period or removed at the temperature of $120^{\circ}C$.

Curve A in Figure I-23 was the current measured during the first heating of the sample. The electric field was then applied continuously during the cooling periods after trial 1 and trial 2 and curve C represents the currents measured during trial 2 and trial 3. At the upper temperature of trial 3, the electric field was removed and then reapplied to the sample after it had reached room temperature. Curve B represents the current measured during trial 4. The field was again removed at the end of the heating cycle and reapplied at room temperature. Trial 5 also produced curve B.

The results of the five current measurements represent evidence that the background current measured in the Lucite samples in an electric field is lower if the electric field is applied during the cooling period after the sample is heated to $120^{\circ}C$. This suggests that the background
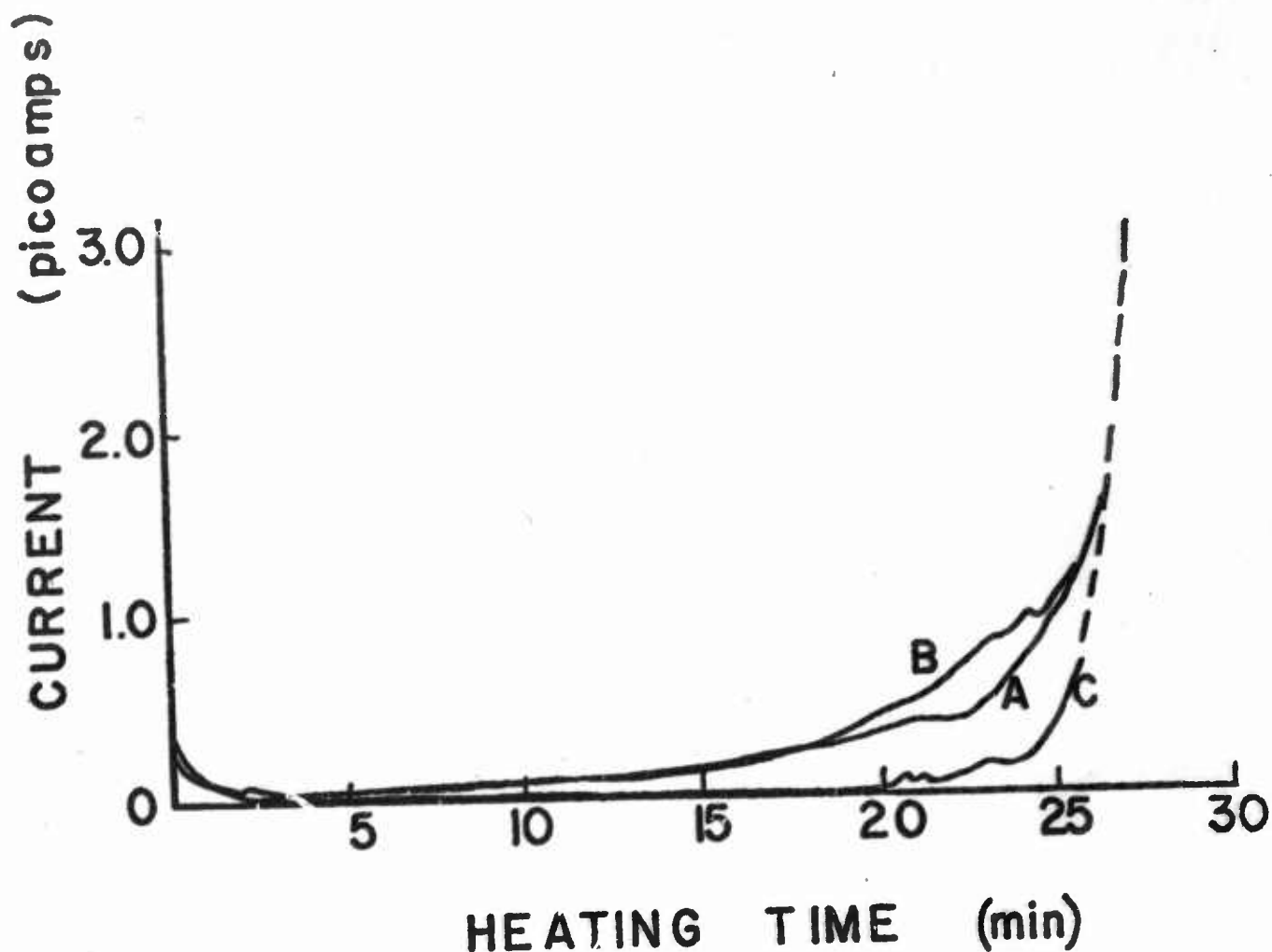
Figure 1-23. Effect of electric field applied during cooling on background current in unirradiated Lucite. First Heating: Curve A—E applied during cooling, Second Heating: Curve C—E applied during cooling, Third Heating: Curve C—E not applied during cooling, Fourth Heating: Curve B—E not applied during cooling, Fifth Heating: Curve B. Applied Field (E): +500 V/cm; Heating Rate: 6°C/min; Sample Size: 2.5 cm dia. x 1.0 cm thick; Zero Temperature Gradient.

current may be due to some type of a polarization effect produced by the electric field during the heating cycle. This effect is similar to that used in the production of electrets.[4]

(4) Combined Effect of Temperature Gradient and Electric Field

The effect of applying both the temperature gradient and an electric field to a sample during the heating cycle was investigated. One cm thick Lucite samples were irradiated to a dose of 0.5 Mrad before the measurements were made. Figure 1-24 shows the results of combining a +200 V/cm field with the temperature gradient. Curve A represents the current in a Lucite sample while under the influence of the temperature gradient only. Curve B represents The current in a similar sample under the influence of a +200 V/cm field. Curve C is the mathematical sum of curves A and B while curve D is the current measured in a Lucite sample under the influence of both the temperature gradient and a +200 V/cm field. The difference between curve D and curve C is probably due to a small change in the temperature gradient produced by the required change in wire connections made to the sample holder.

A measurement was also made with the temperature gradient and a reverse electric field. It was first verified that a reverse electric field would produce equal and opposite currents in the sample. Nearly identical curves of current versus heating time were obtained for + and -300 V/cm fields with the recorder input polarity reversed for the negative electric field.

Figure 1-25 shows the results of combining the temperature gradient with a -300 V/cm field. Again the broken curve is the mathematical sum of the two individual current plots and the solid curve is the measured current plot.
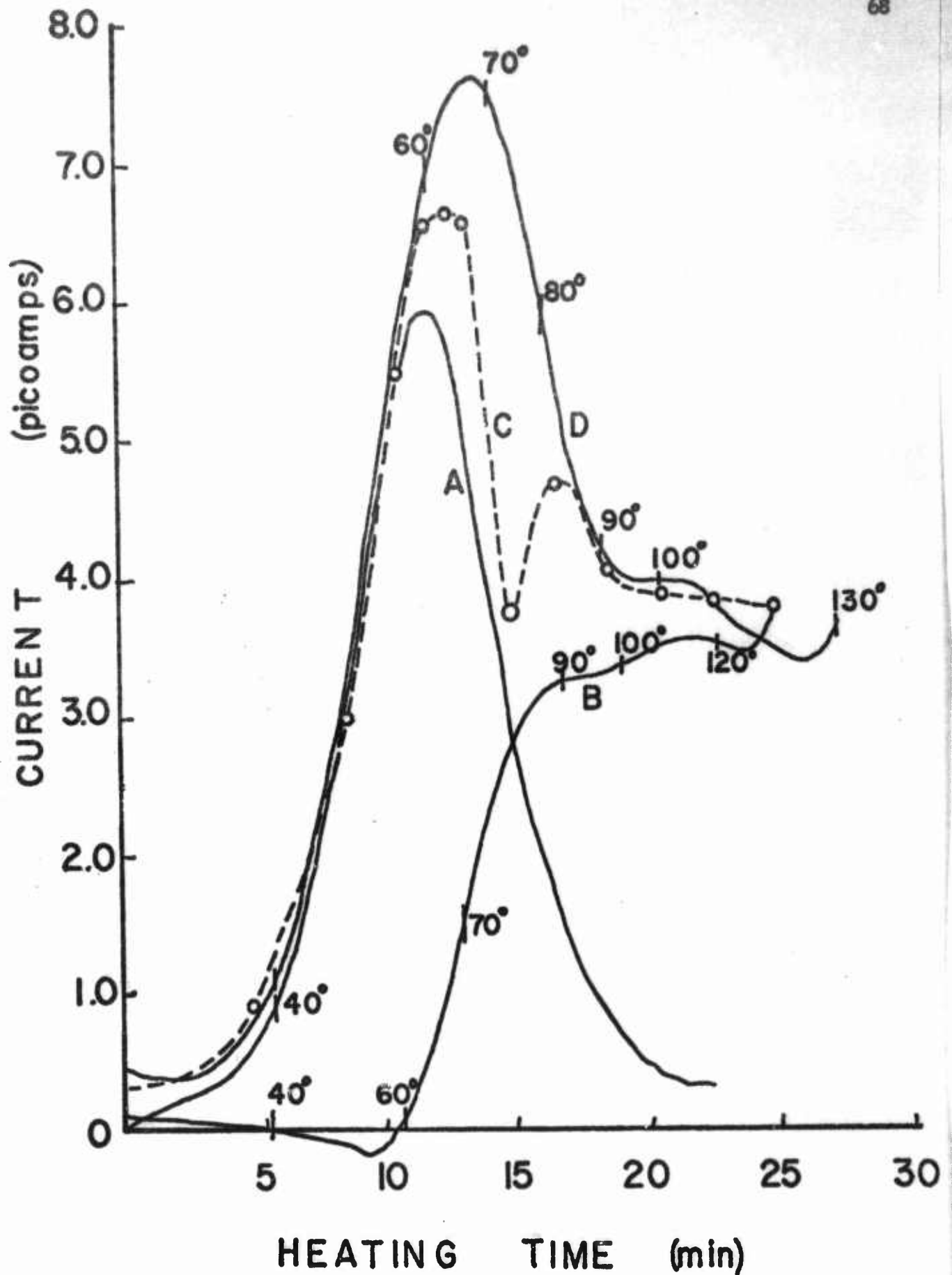
Figure 1-24. Combined effects of temperature gradient and electric field on current generated in irradiated Lucite. Curve A: Temperature gradient only, Curve B: E field only, Curve C: Sum of A and B, Curve D: Measured curve, E field: ±200 V/cm; Heating Rate: 6°C/min; Dose: 0.5 Mrad; Sample Size: 2.5 cm dia. x 1.0 cm thick.
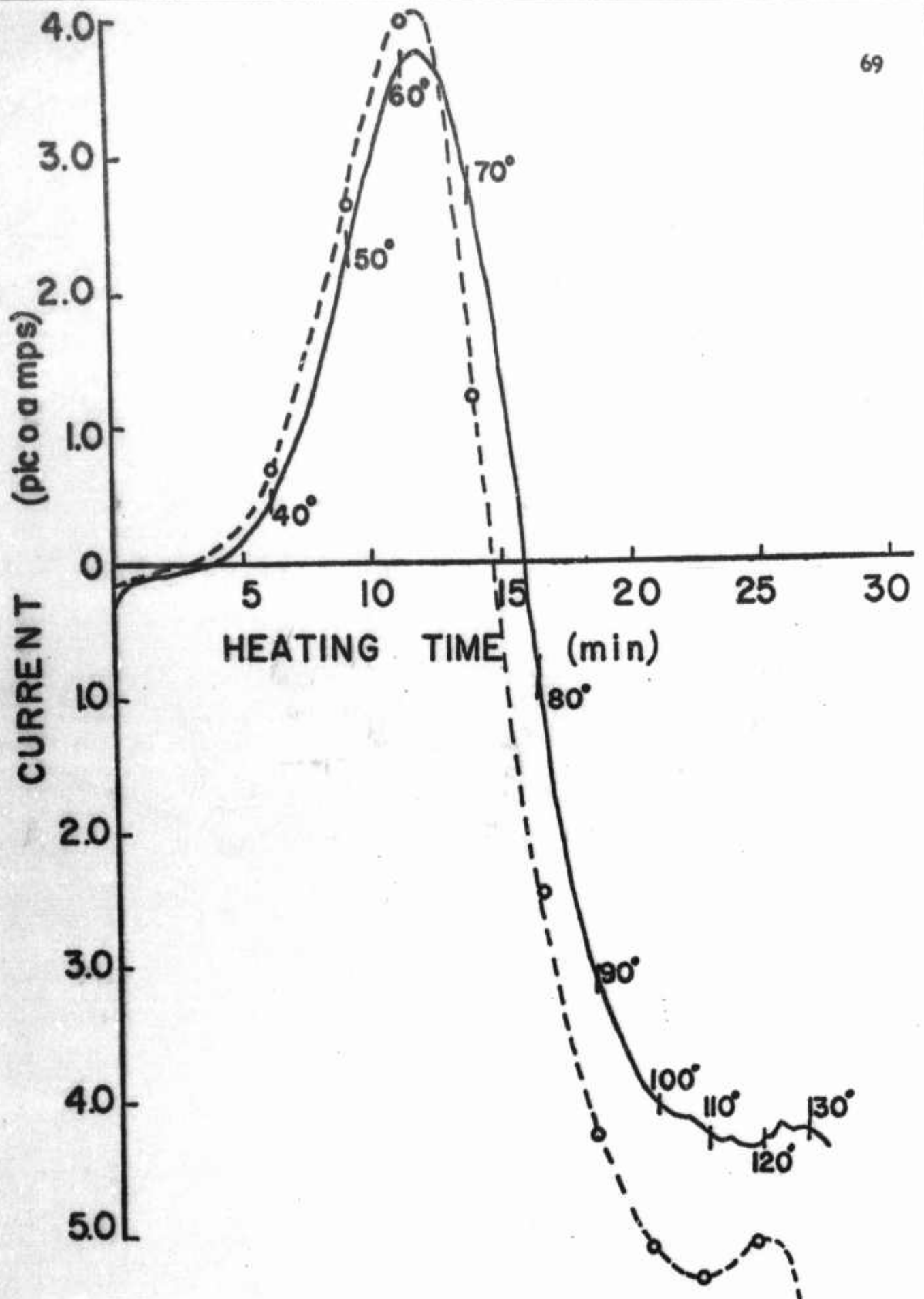
Figure 1-25. Combined effects of temperature gradient and reverse electric field on current generated in irradiated Lucite. —— Curve: Sum of individual effects, —— Curve: Measured curve, E field: -300 V/cm; Heating Rate: 6°C/min; Dose: 0.5 Mrad; Sample Size: 2.5 cm dia. x 1.0 cm thick.

The obvious conclusion from Figures I-24 and I-25 is that the two effects are additive. Therefore current conduction in a temperature gradient and in an electric field must involve different conduction mechanisms.

(5) Currents from Other Polymers

Several polymers were observed to conduct currents in an electric field but not under the influence of the temperature gradient in the same temperature range. Figure I-26 shows current measurements made while heating pure synthesized PMMA and linear polyethylene (PE) in an electric field. Both samples were 1.0 cm thick and were given a dose of 0.5 Mrad prior to measurement. A 500 V/cm field produces about the same current peak height in pure PMMA as a 300 V/cm field produces in PE. The current peak from pure PMMA occurs at $66^{\circ}C$ which is approximately the same temperature at which the thermoelectric current peak occurs in Lucite. The current peak height in pure PMMA is almost twice the current peak height measured in Lucite for the same applied electric field. The peak in Lucite, however, occurs at a much higher temperature than the peak in pure PMMA. The temperature at which the current peak occurs in PE is also much higher than the temperature at the current peak in pure PMMA. The current peak in PE occurs at a temperature of $90^{\circ}C$ which is 20 to $40^{\circ}C$ below the melting temperature[5] (T_m) of 110 to $130^{\circ}C$ for PE.

Figure I-27 shows the current conduction in Teflon while being heated in a 300 V/cm field. The sample was 1.0 cm thick and had been given a dose of 0.5 Mrad prior to measurement. A peak current of 86 picoamps at a temperature of $137^{\circ}C$ was observed. The temperature at the peak is well below the T_m of $327^{\circ}C$ for Teflon. A second heating of the same sample results in the background current shown in the lower curve of Figure I-27.
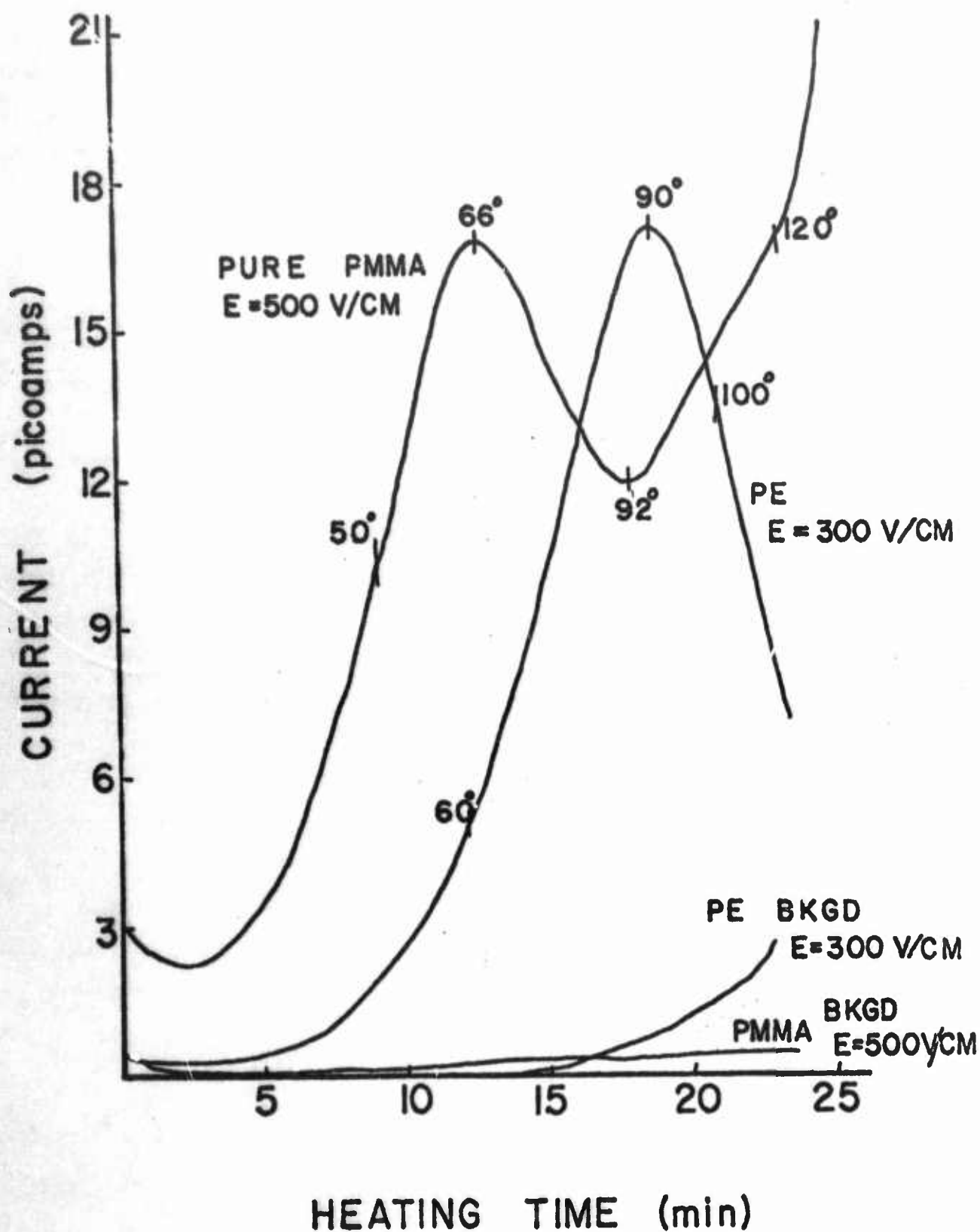
Figure 1-26. Thermally generated current profiles of pure PMMA and PE in an electric field. Dose: 0.5 Mrad; Heating Rate: 6°C/min; Sample Size: 2.5 cm dia. x 1.0 cm thick; Zero Temperature Gradient.

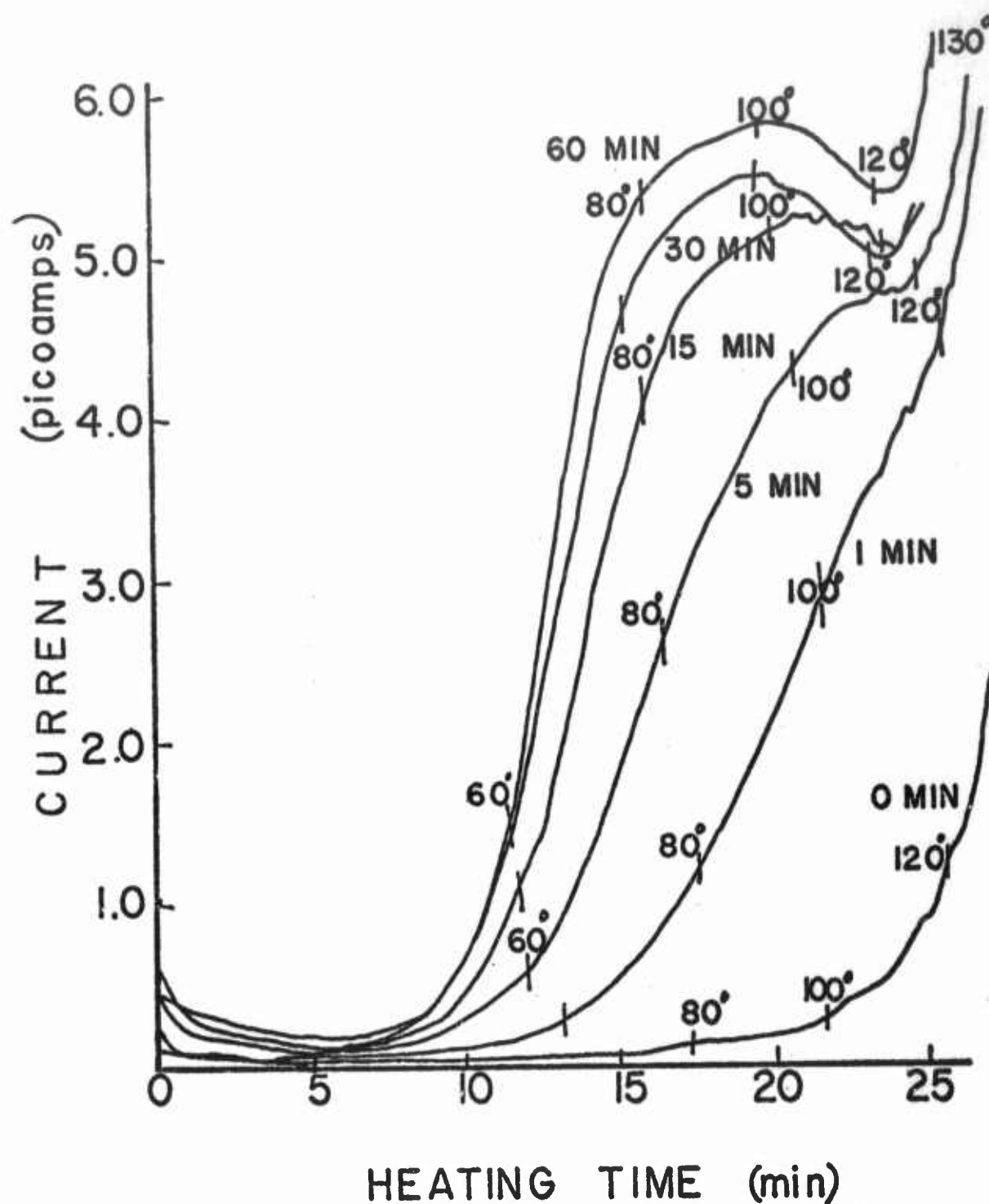Figure 1-27. Thermally generated current profile in Teflon, E = +300 V/cm; Dose: 0.5 Mrad; Heating Rate: 6°C/min; Sample Size: 2.5 cm dia. x 1.0 cm thick; Zero Temperature Gradient.
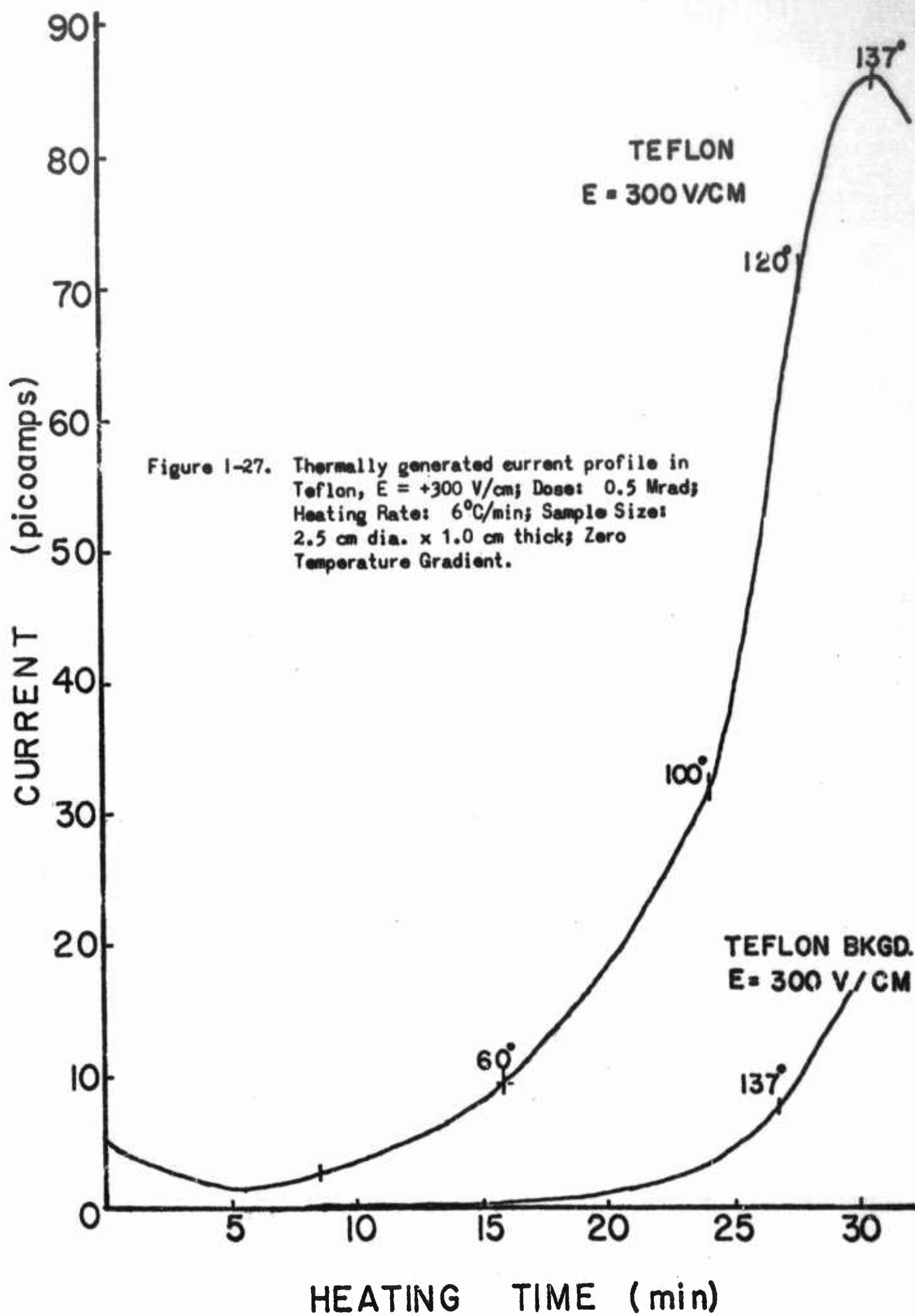
None of these materials--pure PMMA, linear PE or Teflon--produced measurable thermoelectric currents in the temperature range of 25 to 120°C.

Irradiated and unirradiated samples of PVC were also heated in a zero temperature gradient with an electric field applied. The current increased continually from 60°C with temperature for both the irradiated and unirradiated samples. The current reached the maximum range of the electrometer (3×10^{-9} amps) before the heating cycle was completed. Any radiation effects on the thermally-induced currents were therefore masked by the background current.

f. EPR Measurements of Radical Decay with Temperature

Samples of Lucite and PVC were irradiated to a dose of 0.5 Mrad and their free radical concentration was measured by EPR. The variation of free radical concentration was observed at various temperatures while the sample was heated at a linear rate of approximately 6°C/min. Figure I-28 shows the results of such a measurement on the two different samples of Lucite (PMMA) and a sample of PVC. In each case the concentration of free radicals begins to decrease sharply at a specific temperature. For the two Lucite samples this temperature was approximately 65 and 72°C, respectively, and for the PVC sample it was approximately 60°C. The initial increase in the signal intensity from the Lucite samples during the heating process was unexpected but was not investigated further.

4. DISCUSSION

a. Model of Thermoelectric Current Generation

(1) Charge Mobility and Charge Trapping

The results from the synthesized polymers are quite revealing. Pure PMMA with no additives exhibits a very small current. Few charges,
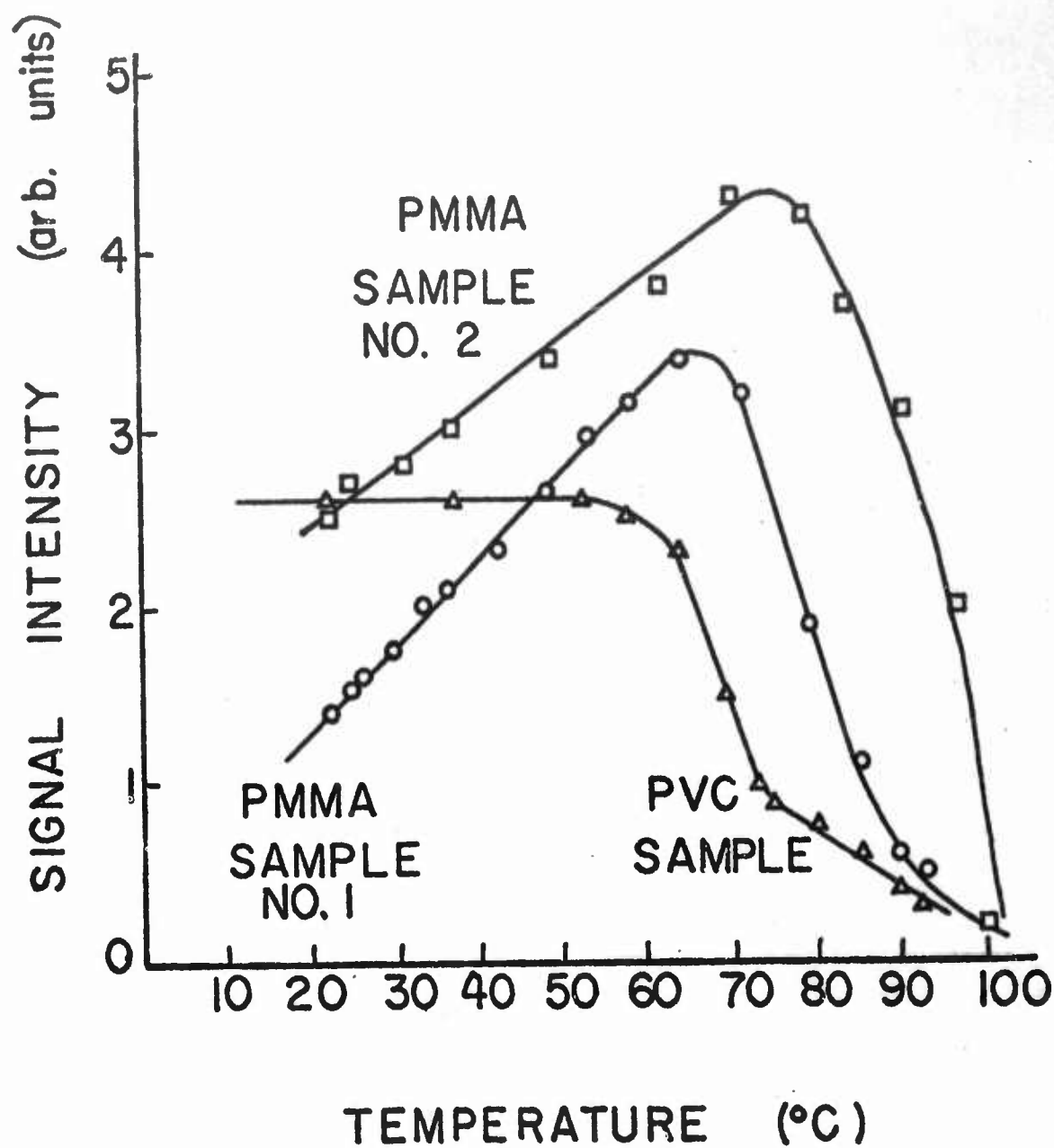
Figure I-28. Variation of EPR signal intensity with
temperature in gamma-irradiated PMMA and PVC.
PMMA (Lucite), Dose: 0.5 Mrad; Heating Rate:
6°C/min.

which contribute to the thermoelectric current, appear to be trapped in it during irradiation at $32^{\circ}C$. Thus either or both positive and negative charges are mobile during irradiation and undergo recombination. If a good electron trapping agent, such as CCl_4, is present the thermoelectric current increases significantly. This suggests that at room temperature in pure PMMA without additives, radiation-produced electrons are mobile and recombine with trapped holes during irradiation. If the positive charge carriers were also mobile in the presence of an electron trap, recombination could still occur, and no increase in the thermoelectric current would be observed. This is contrary to our findings. This conclusion is also supported by the experiments with 2-methylpentene-1 (2-MP-1) in PMMA. In solid organic matrices 2-MP-1 is a good positive center trapping agent and a relatively poor electron trapping agent.[6] PMMA doped with 2-MP-1 exhibits a relatively small current increase compared to pure PMMA. This result would be expected if the positive centers are assumed to be immobile during irradiation.

If CCl_4 or benzoyl peroxide is present in PMMA, the observed thermoelectric current increases by a factor of approximately 10 over that in pure PMMA. CCl_4 is well known to react with electrons by dissociative electron attachment in solid organic matrices. It seems likely that benzoyl peroxide can act in a similar manner because of its weak oxygen-oxygen bonds and the electron affinity of oxygen. Alternatively, it is probable that peroxide and oxide radicals from benzoyl peroxide are produced during polymerization and can act as electron traps. It should be pointed out that electron traps produced by dissociative attachment or by oxygen-containing radicals are quite thermally stable, and may well be stable above

room temperature in a polymer matrix. The results reported here bear this out. Both benzene and chlorobenzene act as poor electron and positive center traps in solid organic matrices. That they cause no increase in the thermoelectric current in PMMA is also consistent with the results cited above.

Commercial PMMA (Lucite) is thermally polymerized by using benzoyl peroxide as a chemical initiator; thus, it should be similar to PMMA doped with benzoyl peroxide. This has been verified. Lucite is, therefore, convenient to work with since it has a built-in electron trap. It should be remembered, however, that the currents observed in Lucite are characteristic of added electron traps and not of the pure PMMA polymer itself.

Polyvinyl chloride shows a relatively large current. It is a polyalkyl chloride and can itself react with electrons by dissociative electron attacnment. Alkyl chlorides readily show this reaction in the solid phase.[7] The large thermoelectric currents observed in PVC, compared with PMMA containing 2 mole % CCl_4, are due to the fact that the number of trapping sites is larger. Also, the C-Cl bond in PVC is distributed uniformly while CCl_4 in PMMA may not be. Commercial PVC may contain additives which also act as electron traps but their effect should not change the behavior of PVC itself.

In contrast to PVC, Teflon shows a negligible thermoelectric current in the temperature range studied. There is no trapping in this polymer because the C-F bond is strong enough to preclude dissociative electron attachment.

The absence of a thermoelectric current in polyethylene (PE) above room temperature is expected because H^- formation is improbable. However,

Frankevich and Tal'roze[8] report "bursts of emf" in electron irradiated PE plates at temperatures both below and above room temperature while the samples were heated in a manner which resulted in a temperature gradient. Further work on PE below room temperature would be of interest.

(2) Sign of the Mobile Charge Carrier

The observation of thermally generated currents indicates that one or both charge carriers are mobilized by thermal stimulation. Since the currents are the result of charge carrier movement in a temperature gradient they are thermoelectric, and the most mobile charge carrier corresponds to the polarity of the colder sample electrode.[9] This was positive for all measurements. Additional evidence that the positive centers are the mobile charge carrier is provided by the information obtained from the use of additives in PMMA. If the electrons were thermally detrapped, the temperature at which the peak current occurs should depend on the particular electron trapping agent. However, the temperature at which the peak current occurs is about the same for all electron trapping agents observed. Therefore it must be the trapped positive centers and not the trapped electrons which are mobilized by thermal excitation.

Positive ion mobility has been proposed by several authors[10,11,12] to explain their measurements of conductivity in an applied electric field during irradiation in PE, polystyrene, Teflon and PVC. Other authors[13-16] propose that the radiation-induced conductivity in the same systems is due to the mobility of electrons. These assumptions are based on an attempt to explain the dependence of the induced current on the dose rate of the incident radiation. But, none of these authors have presented positive experimental evidence for the identity or sign of the mobile

charge carrier during irradiation. The use of a temperature gradient to generate thermoelectric currents has allowed us to obtain the first unambiguous sign determination for charge carriers in irradiated polymeric systems.

b. Charge Trapping Efficiency

(1) Estimation of G Value in Lucite

The G value of trapped charge carriers in Lucite can be estimated from the saturation of normalized total charge versus dose reported previously.[1] The normalized total charge generated in a temperature gradient saturates at a dose of approximately 1.0 Mrad. This value is in agreement with the dose required for the saturation of color centers in PMMA as measured by Gardner and Epstein.[17] At this dose it can be assumed that all trapping sites in the material have been filled. It has been established that benzoyl peroxide provides trapping sites in Lucite. Benzoyl peroxide is present in Lucite in a concentration of approximately 0.12 mole %. From the equation,

$$\frac{DG}{100} = \text{number of trapped charge carriers,}$$

where D is the dose delivered to the sample in ev, we can calculate G if it is assumed that each benzoyl peroxide molecule acts as a trapping site for one charge carrier. The dose delivered to a disk shaped sample, 2.5 cm in diameter and 1.0 cm thick, at the saturation dose of 1 Mrad is 3.6×10^{20} ev, and the number of molecules of benzoyl peroxide in the same sample at a concentration of 0.12 mole % is 4.1×10^{19} molecules. The G value for trapped charges is calculated to be $G = 11.3$. The validity of this result

will be discussed below. This G value is based on the assumption that each benzoyl peroxide molecule forms one trap. If the molecule forms two traps, the G value would be double. The calculation also assumes that the only trapping agent is benzoyl peroxide. Other unknown additives in the commercial material may, in fact, contribute to the trapping. This would also raise the G value.

(2) Calculation of the Net Distance of Charge Carrier Movement

The experiments with blocking electrodes indicate that the charge conduction is due almost entirely to the internal recombination of charge carriers. If a charge, q, moves a distance d between two parallel plates, it will contribute $q\frac{d}{D}$ to the externally measured charge Q, where D is the total distance between the two plates.[18] If charge carriers move at an angle other than $90°$ to the plates, only the component of motion perpendicular to the plates would be registered in the external circuit. The movement of charge carriers under the influence of a temperature gradient is a process of diffusion and therefore involves random motion with a net movement in the direction of the temperature gradient. It is this net motion of charge carriers that is observed. If the externally measured charge is Q, then the average component, d, of net movement of charge carriers perpendicular to the measuring electrodes equals $\frac{Q}{q}D$. The value of Q measured in a 1 cm thick Lucite sample under the influence of a temperature gradient after an absorbed dose of 1 Mrad corresponds to 2.6×10^{-9} coulombs. The value of q is equal to the number of trapped charges $(\frac{DG}{100})$ times 1.6×10^{-19} coulombs per charge and D equals 1.0 cm. From the equation above, d was calculated to be 1.2 $\overset{o}{A}$. This distance seems unrealistically small, since it would represent movement of less than the

internuclear distance between neighboring atoms in the polymer. One might therefore conclude that the calculated G value was much too high, since q is dependent on G, and d equals $\frac{Q}{q}$. The postulate that one charge carrier is trapped per molecule is probably invalid.

If, for example, 10% to 1% of the benzoyl peroxide molecules act as trapping sites, the distance of charge movement would be in the more reasonable range of 12 to 120 $\overset{o}{A}$. One might therefore conclude that the trapping efficiency of benzoyl peroxide in Lucite is less than unity. Similar arguments apply to other electron trapping agents. Since the mobile charge carrier is positive, the relative efficiency of the various electron trapping agents is proportional to the normalized total charge measured in polymer samples containing equal concentrations of each additive after exposure to the same amount of radiation. The assumption has also been made that one positive charge carrier participates in the thermoelectric current for every trapped electron. If only a fraction of the trapped positive charge carriers is able to participate in the thermoelectric current, the calculated recombination distance would have a higher value.

(3) Comparison of Lucite with PVC

Polyvinyl chloride (PVC) gives much larger currents in a temperature gradient than does doped PMMA primarily because of the larger number of trapping sites in this material. The normalized total charge in the sample does not saturate at doses as large as 100 Mrad. The normalized total charge measured in PVC under the influence of a temperature gradient after a dose of 0.5 Mrad is 1.7×10^{-8} coulombs. If a G value of 0.1 is assumed, 5.7×10^{-2} couloumbs would be trapped in the sample, and each mobile charge carrier would move an average of 30 $\overset{o}{A}$ before recombination

occurred. Again this indicates that a value of G much less than 1 must be assumed in order to obtain a reasonable value of d. Since G for total ionization is normally around 3 we see that only a small fraction of the initially formed ions are trapped.

c. Model of Conduction Mechanism

Deutsch and co-workers[3] have measured the dispersion in the dielectric constant and the mechanical compliance of PMMA at various temperatures. By plotting log frequency versus temperature curves for the various parameters they obtain the loci of maximum change in these properties. From these studies they have identified two transitions in PMMA which they have labeled alpha and beta. Alpha is the transition at the highest temperature, $120^{\circ}C$, and corresponds to the change from the glassy to the rubbery state. It is caused by the movement of large groups of atoms or the main polymer chain. Values for the softening point or glass transition temperature, T_g, in PMMA are quoted by different authors as temperatures ranging from $90^{\circ}C$ to $120^{\circ}C$.[19,20] This range of temperatures may be due to different degrees of polymerization and to the fact that different physical parameters were measured as an indication of the transition point.

The beta transition in PMMA was observed by Deutsch, et al., at $50^{\circ}C$. This was determined from measurements of the dielectric loss of the polymer at various temperatures. The change in dielectric loss is ascribed to the onset of free rotation of the polar, carbomethoxy side groups attached to the main polymer chain. From plots of log (frequency at loss maximum) versus $1/T^{\circ}K$, activation energies (E_a) were calculated. Values for the beta transition in PMMA were determined by measurements of two different physical

parameters. From dielectric loss measurements, a value of 20 kcal/mole was calculated, and from audio frequency mechanical loss measurements, E_a was determined to be 18 kcal/mole. This is in excellent agreement with our measured activation energy of 18.6 kcal/mole calculated from the thermal decay of trapped charge carriers in PMMA. Furthermore, the temperature at which the peak thermoelectric current occurs in Lucite is comparable to the temperature of the beta transition. This correlation of activation energy and peak temperature strongly suggests that the detrapping of charge carriers in PMMA is associated with the rotation of the carbomethoxy side groups.

One can then envision an attractive conduction mechanism as illustrated below where positive centers are transferred between adjacent side groups and thus propagated through the sample.

$$
\begin{array}{ccccc}
CH_3 & & H & & CH_3 \\
| & & | & & | \\
-\,C & - & C & - & C\,- \\
| & & | & & | \\
& & H & & \\
C\,-\,O^{\oplus} & \longrightarrow & O\,-\,C & & \\
\| \quad | & & | \quad \| & & \\
O \quad CH_3 & H_3C & O & &
\end{array}
$$
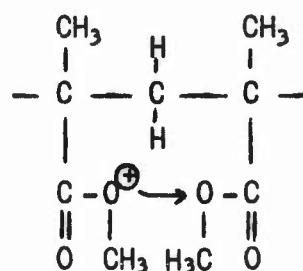
This conduction mechanism should show stereospecificity and depend on whether adjacent carbomethoxy groups are on the same side (isotactic polymer) or opposite sides (syndiotactic polymer) of the main chain. The polymer we have used was largely atactic (random orientation of side groups). Future experiments are aimed toward testing the stereospecificity of the thermo-electric current magnitudes and the trapped charge stability in PMMA.

There is also a correlation between the temperature of the alpha transition in PMMA, between 90°C and 120°C, and the temperature at which

the maximum current occurs in PMMA in an applied electric field. This
suggests that the population of radiation-induced charge carriers, seen with
an applied electric field, are not mobile until a temperature is reached at
which the main polymer chains can move.

The peak thermoelectric current measured in PVC also occurs approxi-
mately at its glass transition temperature. In this case there is no lower
temperature transition due to internal motion and main chain motion is
apparently necessary for conduction to occur. We have found no activation
energy measurements in PVC with which to compare our values. The high
temperature stability of the trapped charge carriers in PVC together with
the ability to build up trapped charge without saturation to very large
doses (to at least 100 Mrad), suggests that the PVC might have possible
application where it is desirable to store relatively large amounts of
charge for long periods of time.

d. Thermally Generated Charge Conduction in an Electric Field

The results reported in Section 3e show conclusively that the conduction
mechanisms and mobile charge carrier populations are different for currents
thermally-generated in an electric field compared with currents produced by
a temperature gradient in irradiated Lucite. The explanation for this
difference is not readily apparent. More definitive experiments will be
necessary before an adequate description of the mobile charge population
responding to the electric field can be given.

The effect of electron scavengers on the radiation-induced electrical
conductivity should be studied in greater detail. How does the concen-
tration of these additives influence the current and the temperature at which

the maximum current occurs? Why is a current observed upon heating irradiated samples of some materials, such as PE, Teflon and pure PMMA, in an electric field, but no thermoelectric current is observed in these materials in the same temperature range? These and other questions need to be answered.

One would expect an electric field to influence the movement of the same thermally liberated charge carriers that would be influenced by a temperature gradient. The observation that the currents produced by these two current generating mechanisms are independent, and can be added or subtracted, is very puzzling. One possible explanation for the origin of the current produced by the electric field is that the radiation polarizes some part of the polymer chain which remains polarized until the sample is heated above the glass transition temperature. At this temperature polarization relaxation could provide the observed current. Further investigation of these phenomena is in progress.

5. REFERENCES

1. L. Kevan, M. Harmony, R. Christoffersen and J. Barnes, Annual Summary Report No. AFRPL-TR-67-319.

2. F. C. Hardtke, J. Chem. Phys., 42, 3000 (1965).

3. K. Deutsch, E. A. W. Hoff and W. Reddish, J. Polym. Sci., 13, 565 (1954).

4. B. Gross, Phys. Rev., 67, 253 (1945).

5. P. J. Flory, Principles of Polymer Chemistry, Cornell University Press, New York, 1953, Chapters 2 and 4.

6. W. H. Hamill, Radical Ions, E. T. Kaiser and L. Kevan, Eds., Wiley-Interscience, New York, 1968, Chapter 9.

7. R. F. C. Claridge and J. E. Willard, J. Amer. Chem. Soc., 87, 4992 (1965).

8. E. L. Frankevich and V. L. Tal'roze, Soviet Physics - Solid State, 3, 131 (1961).

9. F. Gutman and L. E. Lyons, Organic Semiconductors, John Wiley, New York, 1967, p. 75.

10. S. Mayburg and W. L. Lawrence, J. Appl. Phys., 23, 1006 (1952).

11. A. J. Warner, F. A. Muller and H. G. Nordlin, J. Appl. Phys., 25, 131 (1954).

12. P. Y. Feng and J. W. Kennedy, J. Amer. Chem. Soc., 77, 847 (1955).

13. J. F. Fowler and F. T. Farmer, Nature, 173, 317 (1954).

14. J. F. Fowler and F. T. Farmer, Nature, 174, 136 (1954).

15. J. F. Fowler and F. T. Farmer, Nature, 174, 800 (1954).

16. J. F. Fowler, Proc. Roy. Soc., A236, 464 (1956).

17. D. G. Gardner and L. M. Epstein, J. Chem. Phys., 34, 1653 (1961).

18. J. J. Markham, F-Centers in Alkali Halides, Academic Press, New York, 1966, pp. 66-67.

19. E. H. Riddle, Monomeric Acrylate Esters, Reinhold, New York, 1954, p.36.

20. W. J. Roff, Fibres, Plastics and Rubbers, Academic Press, New York, 1956, pp. 195-201.

II. THEORETICAL INVESTIGATIONS

A. INTRODUCTION

In a continuing theoretical study concerned with the characterization of highly energetic species having potential interest to the U. S. Air Force, the tools of ab initio quantum mechanics have been used both to characterize several individual molecules and to devise new techniques of general applicability to molecular problems. Studies of this nature, although time-consuming and often difficult, provide exceedingly powerful tools for the understanding of the chemistry of small molecules, since the solutions of the Schrödinger equation apparently provide the only infallible basis for the discussion of chemical phenomena associated with isolated molecules or small groups of them.

The individual species studied include H_3^+, HeH^+, He_2^{++}, H_2 and Li^+. These species were examined from the point of view of establishing a lower bound estimate of the energy of the ground state. This is an especially important study for molecules such as H_3^+, where the magnitude of the binding energy is crucial to discussions of possible stabilization by anions, and is not known from experiment.

The effort directed toward developing new and innovative techniques which will allow quantum chemists to perform calculations which are accurate enough for the prediction and interpretation of phenomena such as chemical bonding has been carried on in two separate directions.

In order to make lower bound estimates for multi-electron, polyatomic molecules, it was necessary to devise new mathematical techniques for

handling the problem. It was found that Gaussian basis orbitals provided an excellent answer to this search, for all of the integrals that arise can be evaluated either in closed form, or by a single numerical integration. Furthermore, the application of this technique provided a very sensitive test of a trial wavefunction, and indicates where improvements should be made.

The development and implementation of the geminal theory of chemical bonding also experienced major developments. The new technique for the solution of the coupled integro-differential equations that arise in the determination of the optimum geminals for a system has been developed considerably, and an iterative method having quadratic convergence to the true solution has been developed. In addition, the connection between geminal theory and traditional Hartree-Fock theory has been explicitly derived, so that a direct assessment of the expected improvement in accuracy can be made.

The implementation of the calculations using geminal theory on the GE-625 has proceeded slowly, and the integral programs are now fully operational. Since small inefficiencies in programs of this nature result in large increases in the amount of computing time necessary to perform these computations, it was deemed essential to proceed slowly in their development, to be certain that efficiency had not been sacrificed. The consummation of these efforts in terms of the programs to determine the energy and geminals using these integral values is now underway.

B. LOWER BOUND AND ENERGY VARIANCE CALCULATIONS

1. PURPOSE

The Variation Theorem and methods of computation such as configuration interaction provide powerful techniques for obtaining the lowest energy possible for a wavefunction with adjustable parameters.[1] The power of these techniques lies in the fact that, for an arbitrary choice of the adjustable parameters, the energy associated with the trial wavefunction will always be above the true energy of the system. The difficulty in such an approach is that the method in which the trial wavefunction should be found, i.e., which terms and how many terms should be included, is difficult to formulate in general. Thus, there is a great need for a technique that will provide more information concerning the accuracy of both the approximate energy and the associated wavefunction at any stage of complexity.

It is known that an examination of the energy variance associated with a trial wavefunction provides a means by which, in principle, this desired information can be obtained.[2] The variance is defined as

$$U^2 = \langle \mathcal{H}^2 \rangle - \langle \mathcal{H} \rangle^2 \geq 0, \tag{1}$$

where

$$\langle \mathcal{H}^2 \rangle = \int (\mathcal{H}\varphi)^*(\mathcal{H}\varphi) \, d\tau, \tag{2}$$

and

$$\langle \mathcal{H} \rangle = \int \varphi^* \mathcal{H}\varphi \, d\tau. \tag{3}$$

Here φ is a normalized trial wavefunction, $\mathcal{H}$ is the Hamiltonian operator for the system under consideration, and the integration is performed over

the coordinates of all of the electrons. Because of the nature of the operators contained in $\mathcal{H}^2$, the energy variance, which should be zero for an exact solution, provides a sensitive test for any proposed trial function. Also, the formulas of Temple,[3] Stevenson[4] and Weinstein[5] can be used to estimate a lower bound to the true energy of the system if the variance is known. Consequently, an evaluation of U^2 provides not only a means of estimating the overall accuracy of the trial wavefunction, but also a means of bracketing the true energy of the system.

When Slater-type orbitals are used as basis orbitals, the evaluation of the integrals contained in $\langle \mathcal{H}^2 \rangle$ is exceedingly difficult.[6] If, on the other hand, the trial function is formed using a basis set consisting of Gaussian-type orbitals, the necessary integrals over the square of the Hamiltonian can be calculated both accurately and conveniently.

In this study, the energy variance for a series of simple systems has been examined using Gaussian orbitals. The systems that were investigated are H_2^+, H_2, HeH^+, He_2^{++} and H_3^+.

2. ENERGY VARIANCE CALCULATIONS

The wavefunctions for the above systems that were employed in this study have been reported recently by M. Schwartz and L. Schaad.[7,8] In that study, a basis set consisting of unnormalized, 1s-type Gaussian orbitals was employed,[9]

$$G_A(1) = \exp(-ar^2_{A1}), \tag{4}$$

where

$$r^2_{A1} = (x_1-A_X)^2 + (y_1-A_Y)^2 + (z_1-A_Z)^2, \tag{5}$$

and where "a" is a variable orbital exponent. Also, (A_x, A_y, A_z) locate the position of the Gaussian orbital relative to some arbitrary origin. The coordinates (A_x, A_y, A_z) do not necessarily coincide with a nucleus, thus allowing for the possibility of "floating" orbitals.

In the determination of the wavefunction to be used here, the energy was minimized with respect to all the parameters, including the position and size of the Gaussians. The non-relativistic Hamiltonian for a system of N electrons and M nuclei, within the Born–Oppenheimer approximation, can be written in atomic units[10] as

$$\mathcal{H} = -\tfrac{1}{2} \sum_{i=1}^{N} \nabla_i^2 - \sum_{i=1}^{N} \sum_{A=1}^{M} \frac{Z_A}{r_{Ai}} + \sum_{i<j}^{N} \frac{1}{r_{ij}} + \sum_{A<B}^{M} \frac{Z_A Z_B}{r_{AB}} , \tag{6}$$

where the indices i and j refer to electrons, and A and B refer to nuclei. By direct substitution of equation (6) into equation (2), it can be seen that the new integrals that arise in the evaluation of $\langle \mathcal{H}^2 \rangle$ that have not already been evaluated in $\langle \mathcal{H} \rangle$ are, when written in their most general form,

$$J_1 = \int [\nabla_1^2 \varphi_A(1)][\nabla_1^2 \varphi_B(1)] \, dv_1 , \tag{7}$$

$$J_2 = \int [\frac{1}{r_{C1}} \varphi_A(1)][\nabla_1^2 \varphi_B(1)] \, dv_1 , \tag{8}$$

$$J_3 = \iint [\nabla_1^2 \varphi_A(1) \varphi_C(2)][\frac{1}{r_{12}} \varphi_B(1) \varphi_D(2)] \, dv_1 \, dv_2 , \tag{9}$$

$$J_4 = \int [\frac{1}{r_{C1}} \varphi_A(1)][\frac{1}{r_{C1}} \varphi_B(1)] \, dv_1 , \tag{10}$$

$$J_5 = \iint [\frac{1}{r_{12}} \varphi_A(1) \, \varphi_C(2)][\frac{1}{r_{12}} \varphi_B(1) \, \varphi_D(2)] \, dv_1 \, dv_2 \; , \tag{11}$$

$$J_6 = \int [\frac{1}{r_{C1}} \varphi_A(1)][\frac{1}{r_{D1}} \varphi_B(1)] \, dv_1 \; , \tag{12}$$

$$J_7 = \iint [\frac{1}{r_{E1}} \varphi_A(1) \, \varphi_C(2)][\frac{1}{r_{12}} \varphi_B(1) \, \varphi_D(2)] \, dv_1 \, dv_2 \; , \tag{13}$$

$$J_8 = \iiint [\frac{1}{r_{12}} \varphi_A(1) \, \varphi_C(2) \, \varphi_E(3)][\frac{1}{r_{13}} \varphi_B(1) \, \varphi_D(2) \, \varphi_F(3)] \, dv_1 \, dv_2 \, dv_3 \; . \tag{14}$$

The reason for the intractability of these integrals when Slater-type orbitals are employed is apparent, due to the presence of a four-center one-electron integral, as well as a five-center two-electron and a six-center three-electron integral. A discussion of the methods used to evaluate these integrals is given in the subsection on integral evaluation.

For H_2^+, the nine-term optimized wavefunction for the $^2\Sigma_g^+$ ground state was employed. For the diatomic molecules H_2, He_2^{++} and HeH^+, the wavefunctions as given in Tables IX, XI and XII of Reference (7) were employed. These configurations take into account the left-right and in-out correlation of the electrons, with a complete optimization of all the parameters. Finally, for H_3^+ the multi-configurational wavefunctions, whose complexity is defined by the parameters (n_1, n_2, n_3), were used. These calculations on H_3^+ represent the best variational calculations on this molecule to date.

The total wavefunction for the two-electron molecules can be written as

$$\psi(1,2) = \underset{\sim}{\varphi}^\dagger(1) \, \underset{\sim}{C} \, \underset{\sim}{\varphi}(2) \tag{15}$$

where $\underset{\sim}{\varphi}$ is a column vector of $1s$-type Gaussian orbitals, and the coefficient matrix $\underset{\sim}{C}$ is real and symmetric.

The results of the computations using these wavefunctions are given in Table II-I. Included in this table are the expectation values over $\mathcal{H}$ and $\mathcal{H}^2$, as well as the variance U^2, the Weinstein lower bound λ_W, and the expectation values of the three components of $\mathcal{H}^2$, T^2, $(TV+VT)$, and V^2, respectively.

3. DISCUSSION

The value of the energy variance is, with the possible exception of H_2^+, far from the desired zero result. This is not particularily surprising, since the parameters contained in the wavefunction have been obtained by the minimum energy condition of the variational method. This does not necessarily guarantee that the expectation value of the other operators will be predicted accurately, since another quantum mechanical operator may weight a different region in space than does the Hamiltonian.[11] Thus, it is expected that the operators contained in $\mathcal{H}^2 (= T^2 + TV + VT + V^2)$ will provide a critical test of any wavefunction. Operators such as ∇_1^4 depend not only on the accuracy of the charge density close to the nuclei, but also on the slope of the wavefunction in that region. It is in this region, however, where Gaussian orbitals generally have difficulty providing a good description of the charge distribution, which is a point that has been emphasized recently by Schwartz.[12] In the case of the hydrogen atom, Schwartz compared the local energy for the exact solution to that of a Gaussian approximation to this exact solution. Although the energy was within 10^{-6} hartrees of the true energy, the best energy variance was only 0.013 hartrees^2. It was pointed out that, for the hydrogen atom case in particular,

$$(H^2 \psi)/\psi = [(T+V)^2 \psi]/\psi \tag{16}$$

Table II-I. A Tabulation of Some Expectation Values of the Gaussian Wavefunctions. The column N indicates the increasing complexity of the Gaussian description. Here λ_w is the Weinstein lower bound to the true energy and is defined by $\lambda_w = \langle H \rangle - (U^2)^{1/2}$. All values in this table are quoted in terms of hartree atomic units.[10]

	$\langle H \rangle$	$\langle H^2 \rangle$	U^2	$\langle T^2 \rangle$	$\langle TV+VT \rangle$	$\langle V^2 \rangle$	λ_w	N
H_2^+	- 0.602592	0.386131	.023014	1.579485	- 3.875947	2.682593	- 0.754296	1
	- 0.602634[a]							
H_2	- 1.07347	2.231802	1.079464	1.808578	- 5.987839	6.411063	- 2.112443	1
	- 1.13703	2.140708	0.847871	2.724103	- 8.048824	7.465429	- 2.057829	2
	- 1.14929	1.939574	0.618506	3.188669	- 9.029406	7.780111	- 1.935741	3
	- 1.15485	1.885138	0.551459	3.320432	- 9.320626	7.885282	- 1.897453	4
	- 1.15737	1.814827	0.475322	3.479164	- 9.642192	7.977855	- 1.846806	5
	- 1.15849	1.699423	0.357324	3.624849	- 9.944976	8.019550	- 1.756256	6
	- 1.15881	1.667315	0.324474	3.669935	- 10.036355	8.033735	- 1.728436	7
	- 1.1744[b]							
He_2^{++}	- 3.35161	21.365693	10.132403	17.313423	- 56.993632	61.045902	- 6.534753	1
	- 3.57010	21.034101	8.288487	28.552041	- 82.440839	74.922899	- 6.449073	2
	- 3.61398	19.139842	6.078991	34.100672	- 94.259451	79.298621	- 6.079541	3
	- 3.64128	19.169255	5.910335	35.391359	- 97.473307	81.251203	- 6.072398	4
	- 3.64906	17.697876	4.382237	37.879440	-102.562428	82.380864	- 5.742439	5
	- 3.680[c]							

Table II-I. (continued)

	$<H>$	$<\mathcal{H}^2>$	U^2	$<T^2>$	$<TH+VT>$	$<V^2>$	λ_w	N
HeH⁺	- 2.59534	14.249430	7.524018	10.352679	- 34.447640	38.344391	- 5.336334	1
	- 2.84261	14.808039	6.727607	19.426967	- 55.358805	50.739877	- 5.436373	2
	- 2.88636	13.130263	4.799189	24.553751	- 66.168570	54.744882	- 5.077065	3
	- 2.92291	13.308922	4.765519	23.870475	- 64.922177	54.360199	- 5.105798	4
	- 2.93149	11.912772	3.319138	26.315701	- 69.929623	55.526694	- 4.748080	5
	- 2.93957	12.293862	3.652790	26.434521	- 70.361794	56.221135	- 4.850797	6
	- 2.94446	12.209595	3.539750	26.606203	- 70.773383	56.376775	- 4.825882	7
	- 2.978ᵈ							
H₃⁺								
(1,1,0)	- 1.27368	2.805540	1.183279	2.805237	- 8.869414	8.869717	- 2.361466	1
(1,1,1)	- 1.30459	2.717427	1.015472	3.238075	- 9.880413	9.359765	- 2.312296	2
(2,1,0)	- 1.31730	2.559759	0.824480	3.683690	- 10.857453	9.713522	- 2.225309	3
(2,2,0)	- 1.32438	2.462601	0.708619	3.888858	- 11.255168	9.858911	- 2.165807	4
(2,2,2)	- 1.33155	2.441650	0.668625	3.911305	- 11.361224	9.891569	- 2.149428	5
(3,3,1)	- 1.33423	2.207586	0.427416	4.265828	- 12.083831	10.025589	- 1.987988	6
(4,4,1)	- 1.33650	2.216552	0.430320	4.288042	- 12.146910	10.075420	- 1.992488	7
(4,5,1)	- 1.33764	2.195881	0.406600	4.318873	- 12.213129	10.090137	- 1.975291	8

(a) and (b) represent the "exact" solutions for the nonrelativistic Schrödinger equation in the Born-Oppenheimer approximation. See References (17) and (18), respectively.
(c) See Reference (19).
(d) See Reference (20).

should be constant for an exact solution[12,13] and that deviations from constancy for a trial function can be attributed to a variance in the terms containing the momentum operator. Thus, one might expect for the more complicated molecules under consideration here that this situation will be magnified. In addition, any inadequacy of the wavefunction to describe the electron correlation is also expected to be a contributing factor to the magnitude of the energy variance.

Unfortunately, it is not possible to compare the components of $\langle \mathcal{H}^2 \rangle$; namely, $\langle T^2 \rangle$, $\langle TV+VT \rangle$ and $\langle V^2 \rangle$, with their "true" values for the cases under consideration here. However, a comparison of these quantities as a function of the complexity of the wavefunction can give some indication of their convergence. For this reason they are also listed in Table II-I. As can be seen for those cases where a variety of trial wavefunctions were used, the rather rapid convergence of the energy is not accompanied by a corresponding convergence of the energy variance.

The investigations that were made on the one-electron H_2^+ ion provide an energy variance of 0.023 hartrees^2, which is comparable in magnitude to that obtained for the hydrogen atom[12] (.013 hartrees^2). Although the energy in both these systems is accurately predicted, the magnitude of the quantity, $\langle \mathcal{H}^2 \rangle - \langle \mathcal{H} \rangle^2$, is far from zero. This result emphasizes dramatically that $\langle \mathcal{H}^2 \rangle$ accentuates the features of the wavefunction not accounted for in its variational determination. Furthermore, it points out how the supposition that a good energy necessarily leads to an accurate overall wavefunction can be erroneous.

The calculations on the two-electron systems H_2 and H_3^+ provide even more striking examples of the inability of the minimization of the upper

bound to provide a good energy variance. In these cases a decrease in the accuracy of the total energy, due primarily to the difficulty of describing the electron correlation, is reflected in a marked increase in the energy variance over that found for the one-electron systems. Furthermore, the sensitivity of U^2 to the complexity of the wavefunction is clearly demonstrated. For example, a consideration of the two best wavefunctions for the hydrogen molecule shows that the change in U^2 is 100 times greater than the change in $\langle \mathcal{H} \rangle$. Similarily, for H_3^+ a change in $\langle \mathcal{H} \rangle$ of .001 hartrees is accompanied by a change in U^2 of .028 hartrees^2. Also, the large change in the variance cannot be traced directly to any one of the components of $\langle \mathcal{H}^2 \rangle$, for they are all far from constant, although $\langle V^2 \rangle$ does appear to be converging slightly faster than $\langle TV+VT \rangle$ or $\langle T^2 \rangle$. Thus, the extension to the case of two electrons with the concommitant introduction of correlation effects suggests that the poor lower bound is not only due to the lack of accuracy in the description of the local kinetic energy near the nucleus, but also that $\langle V^2 \rangle$ is poorly represented.

A similar situation exists for He_2^{++} and HeH^+. In addition to the considerations already discussed, the larger nuclear charges are more demanding of the trial function in the vicinity of these nuclei. The inability of the Gaussian description to accurately reproduce both the slope and magnitude of the wavefunction in this region is responsible for the electronic energy of these systems being considerably higher than their true values. Also, it is these features of the Gaussians that are heavily weighted by the operator $\mathcal{H}^2$. As a consequence, the components of $\langle \mathcal{H}^2 \rangle$ are greater than those of H_2 by an order of magnitude, and their lack of convergence is not unexpected.

To estimate the accuracy of the charge distribution around a nucleus, a computation of the forces provides a useful test. For a heteronuclear diatomic molecule, AB, the net force on nucleus A in the z-direction, equal to $-\partial E/\partial zA$, is given by[14]

$$F_A = F_{zA}^{\ n} \text{ (nuclear)} + F_{zA}^{\ e} \text{ (electronic)}, \tag{17}$$

or

$$F_A = \frac{Z_A Z_B}{r_{AB}^2} - Z_A \int \psi(1,2,...N) \sum_{i=1}^{N} \frac{z_{Ai}}{r_{Ai}^3} \psi(1,2,...N) \, d\tau_1 \, d\tau_2 \, ...d\tau_N, \tag{18}$$

according to the coordinate system in which the origin is chosen at atom A, and $+z_A$ is measured in the direction toward atom B. F_B is similarily defined. Here the perpendicular forces on the nuclei A and B are zero by symmetry. The first term in Equation (18) represents the nuclear force of repulsion, and the second term represents the electronic force of attraction. For H_3^+ the situation is rather more complicated. Here the total force can be divided into two components, $F_{\parallel}$ and $F_{\perp}$ respectively, as shown in Figure II-1.

$$F_{\parallel} = \frac{3}{2r_{AB}^2} - \int \psi(1,2) \sum_{i=1}^{2} \frac{z_{Ai}}{r_{Ai}^3} \psi(1,2) \, d\tau_1 \, d\tau_2 \, , \tag{19}$$

and

$$F_{\perp} = \frac{\sqrt{3}}{2r_{AB}^2} - \int \psi(1,2) \sum_{i=1}^{2} \frac{y_{Ai}}{r_{Ai}^3} \psi(1,2) \, d\tau_1 \, d\tau_2 \, . \tag{20}$$

For a stable molecule the net forces on the nuclei must be zero. Thus

$$F_A = F_B = 0, \qquad\qquad F_{\parallel} = F_{\perp} = 0. \tag{21}$$
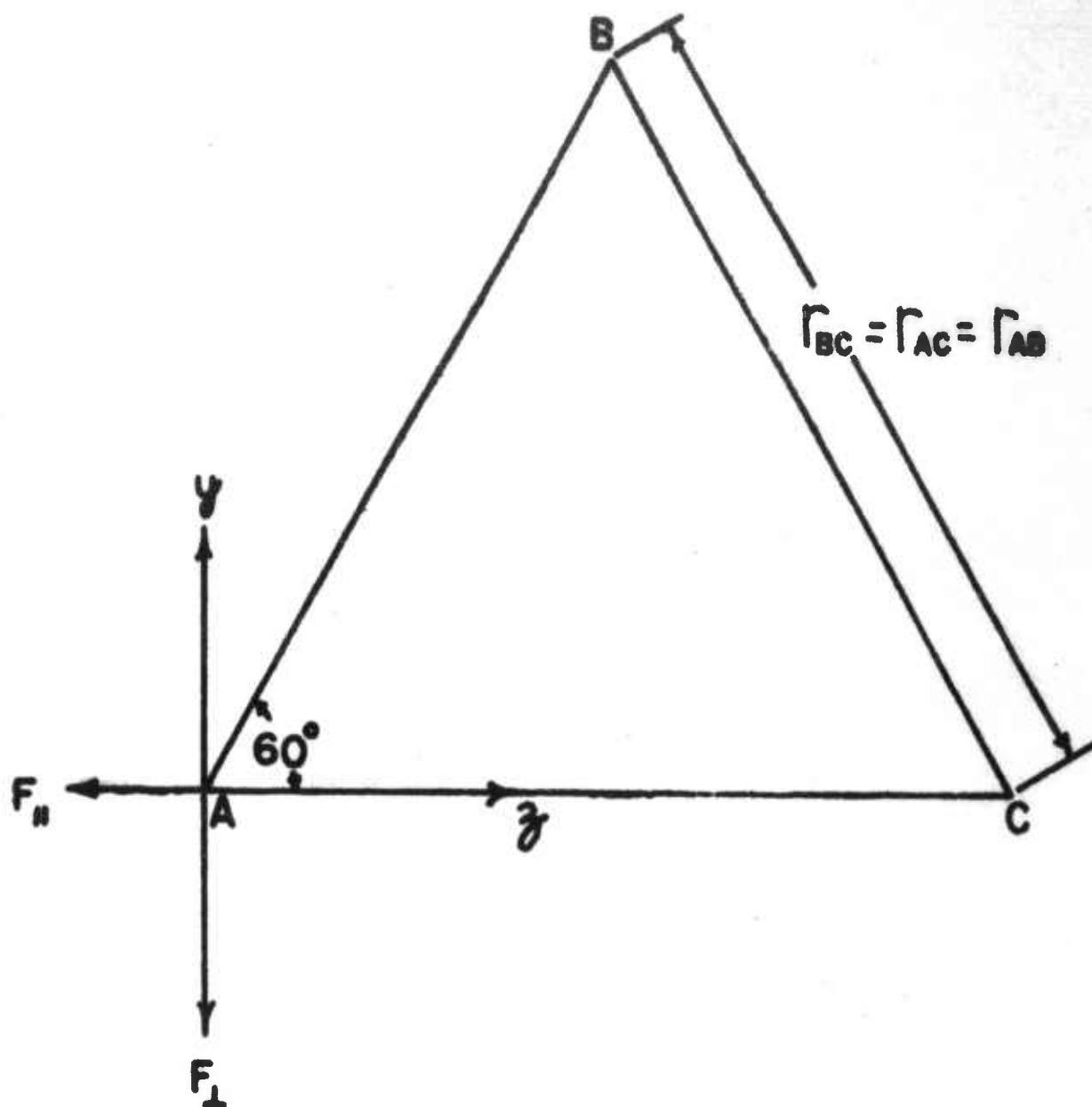
Figure II-1. The definition of $F_{||}$ and $F_{\perp}$ and the coordinate system to be used for the H_3^+ molecule.

The value of these resultant forces for the approximate wavefunctions are
listed in Table II-II. These values are generally very good, and come close
to meeting this requirement, with the obvious exception of HeH⁺, and to a
lesser extent He₂⁺⁺. In HeH⁺ the large positive value of F_H, in contrast
to the nearly zero value of F_{He}, indicates that there is a deficiency of
charge to the bonding side of the hydrogen nucleus. This suggests that, in
the determination of the wavefunction, the larger nuclear charge associated
with the Helium nucleus places a more stringent condition on the energy,
which the wavefunction tries to meet at the expense of the description of
the charge associated with the proton. Such a deficiency of charge is
undoubtedly a large contributing factor to the poor value of the energy
variance. In He₂⁺⁺ the higher nuclear charges are responsible for the value
of F_{He} to be an order of magnitude higher than F_H in H_2, which is a result
that is consistent with the increase in magnitude of $\langle \mathcal{H}^2 \rangle$ with increasing
nuclear charge.

4. INTEGRAL EVALUATION

The integrals J_1, J_2 and J_3 can be readily obtained from the overlap,
nuclear attraction and electron repulsion integrals, respectively, by
recalling the identity

$$\nabla_1^2 \, G_A(1) \; \equiv \; \nabla_A^2 \, G_A(1) \tag{22}$$

where now ∇_A^2 is independent of the electronic coordinates, and hence the
integration variables. Thus, we have

Table II-11. The Resultant Forces on the Nuclei as Defined by Equations (II-18), (II-19) and (II-20). Here, for example, $F_H(H_2^+)$ represents the net force on the hydrogen nucleus in H_2^+. All values are quoted in atomic units. As previously, N indicates the complexity of the wavefunction.

N	$F_H(H_2^+)$	$F_H(H_2)$	$F_{He}(He_2^{++})$	$F_{He}(HeH^+)$	$F_H(HeH^+)$	$F_{\parallel}(H_3^+)$	$F_{\perp}(H_3^+)$
1	- 0.00450	+ .022747	- .013331	+ .040223	+ .344017	+ .002088	+ .001205
2		+ .005466	- .016405	+ .043697	+ .271296	- .000620	- .000358
3		+ .004085	- .003531	+ .017770	+ .234322	+ .000146	+ .000084
4		+ .004215	+ .023098	+ .021861	+ .189922	- .000294	- .000170
5		+ .003442	+ .028628	+ .017134	+ .175108	- .002159	- .001247
6		+ .003149		+ .037945	+ .167810	- .001853	- .001069
7		+ .004247		- .009967	+ .148542	- .001161	- .000670
8						+ .000249	+ .000144

$$J_1 = \nabla_A{}^2 \nabla_B{}^2 \int G_A(1) \, G_B(1) \, dv_1 \, ,$$

$$= K \left(\frac{\pi}{p}\right)^{\frac{3}{2}} \left(\frac{ab}{p}\right)^2 \left\{ 60-80\left(\frac{ab}{p}\right) \overline{AB^2} + 16 \left(\frac{ab}{p}\right)^2 \overline{AB^2} \cdot \overline{AB^2} \right\} . \qquad (23)$$

$$J_2 = \nabla_B{}^2 \int G_A(1) \frac{1}{r_{C1}} \, G_B(1) \, dv_1 \, ,$$

$$= \left(\frac{4\pi bK}{p}\right) \left\{ 2b \cdot \overline{CP^2} \cdot F_2(X_1) + \left[\left(\frac{4ab}{p}\right) \overline{ABCP} - \left(\frac{3b}{p}\right) \right] F_1(X_1) \right.$$

$$\left. + \left[\left(\frac{2a^2b}{p^2}\right) \overline{AB^2} - \left(\frac{3a}{p}\right)\right] F_0(X_1) \right\} . \qquad (24)$$

$$J_3 = \nabla_A{}^2 \iint G_A(1) \, G_C(2) \frac{1}{r_{12}} \, G_B(1) \, G_D(2) \, dv_1 \, dv_2 \, ,$$

$$= \left[\frac{2\pi^{\frac{5}{2}} \cdot K \cdot L}{p \cdot q(p+q)^{\frac{1}{2}}}\right] \left\{ \left(\frac{ab}{p}\right) \left[\left(\frac{4ab}{p}\right) \overline{AB^2} - 6\right] \cdot F_0(X_2) \right.$$

$$\left. + \left[\frac{a^2 q}{p(p+q)}\right] \left[8 \cdot b \cdot \overline{ABPQ} - 6 \right] \cdot F_1(X_2) + \left[\frac{4a^2 q^2}{(p+q)^2} \cdot \overline{PQ^2}\right] \cdot F_2(X_2) \right. . \qquad (25)$$

where

$$p = (a+b) \, , \qquad\qquad q = (c+d) \, ,$$
$$P_i = (aA_i + bB_i)/p \, , \qquad\qquad Q_i = (cC_i + dD_i)/q \, .$$
$$i = X, Y, Z$$

and, in general,

$$\overline{EF^2} = \sum_{X,Y,Z} (E_X - F_X)^2 \, , \qquad\qquad \overline{EFGH} = \sum_{X,Y,Z} (E_X - F_X)(G_X - H_X) \, .$$

Also, $\quad K = \exp\left(-\frac{ab}{p} \cdot \overline{AB^2}\right) \, , \qquad L = \exp\left(-\frac{cd}{q} \cdot \overline{CD^2}\right)$

$$X_1 = p\overline{CP^2} \, , \qquad\qquad X_2 = \frac{pq}{p+q} \overline{PQ^2} \, .$$

In the calculation of J_2 and J_3 it is seen that we are required to evaluate the function $F_m(t)$, (m=0, 1 or 2), defined as

$$F_m(t) = \int_0^1 u^{2m} \exp(-tu^2) \, du \quad .$$ (26)

Satisfactory computational procedures for this auxiliary function have been given by Shavitt,[21] and are based on the recurrence relation

$$F_m(t) = [2t \cdot F_{m+1}(t) + \exp(-t)]/(2m+1) \quad .$$ (27)

It was found that the assumption $F_{46} = 0$ was sufficient to assure eight decimal place accuracy for $F_0(t)$, $F_1(t)$ and $F_2(t)$ for $0 < t \leq 17$. When the argument is larger than 17 the asymptotic forms given by Shavitt were employed.

The remaining integrals ($J_4 \rightarrow J_8$) have been treated within a different context[22,23] and will not be dealt with here in detail. There are, however, several points that should be mentioned.

The integrals J_4 and J_5 can be reduced to a knowledge of Dawson's Integral, defined as

$$D(X) = \exp(-X^2) \int_0^X \exp(y^2) \, dy \quad .$$ (28)

In order to evaluate this function rapidly and accurately, several different representations were employed, depending upon the magnitude of the argument[24,25,26] ($1 \leq X < 2$; $2 \leq X \leq 6$; $6 < X$). For small values of $X(<1)$ it was found convenient to use a Taylor series expansion of the integral about $X = 0$. This results in

$$D(X) = \exp(-X^2) \sum_{n=1}^{\infty} \frac{X^{2n-1}}{(2n-1)(n-1)!} \quad .$$ (29)

The rapid conve-gence of the above form is illustrated by noting that 13 terms are required for the severest case ($X = 0.99999999$). Finally, for $X=0$, which represents a special case in J_4 and J_5, a particularly simple form is found

$$J_4 = 2\pi^{3/2} \cdot K/p^{1/2} \quad, \qquad J_5 = 2\pi^3 \cdot K \cdot L/p^{1/2} \cdot q^{1/2} \cdot (p+q) \quad.$$

The integrals J_6 and J_7 have been calculated numerically. These numerical integrations can be satisfactorily computed by splitting the range $(0, \infty)$ into the ranges $(0,1)$ and $(1,\infty)$ and using 24-point Gauss-Legendre quadrature[27] in each range. A similar numerical technique was used in the calculations of the electronic forces. Here the correct components [see equations (18), (19) and (20)] are obtained from

$$\int G_B(1) \frac{1}{r_{A_1}^3} G_C(1) \, dv_1 \tag{30}$$

by the identities[21]

$$\frac{1}{2\alpha} \frac{\partial}{\partial A_Z} \exp(-\alpha \, r_{A_1}^2) = Z_{A_1} \exp(-\alpha \, r_{A_1}^2) \tag{31}$$

and

$$\frac{1}{2\alpha} \frac{\partial}{\partial A_Y} \exp(-\alpha \, r_{A_1}^2) = Y_{A_1} \exp(-\alpha \, r_{A_1}^2) \tag{32}$$

where now $1/r_{A_1}^3$ in Equation (30) is replaced by

$$\frac{1}{r_{A_1}^3} = \frac{1}{\Gamma(\frac{3}{2})} \int_0^\infty \alpha^{1/2} \exp(-\alpha \, r_{A_1}^2) \, d\alpha \quad,$$

Since many of these integrals have not been tabulated previously, it is necessary to check the accuracy of the integral calculations. To accomplish

this, several identities can be made that are useful. For example, the numerical integration procedures that are needed for J_6 were checked by allowing nucleus D to become coincident with nucleus C, in which case J_4 is obtained (this transformation does not apply to HeH$^+$). A further check on the accuracy of the numerical integrations can be obtained by transforming the integrals to different forms before integrating. Independent calculations on the integrals $J_1 \rightarrow J_3$ can be obtained by the use of the Hermitian property of the momentum operator to give equivalent forms.

5. CONCLUSIONS

The rather large values of the energy variance point out the inability of these particular Gaussian orbitals to describe accurately the true wavefunctions for the systems under consideration. While in most cases the electronic energy is predicted accurately, the magnitude of U^2 is very large. A striking example is the one-electron H_2^+ molecule-ion. In this case the energy is accurate to within 4×10^{-4} hartrees, while the energy variance is far from zero, .023 hartrees^2.

For the two electron systems, any decrease in the accuracy of the wavefunctions, from the energy point of view, is magnified in the energy variance. This is not unexpected, and is due primarily to the sensitivity of the wavefunction to the operators contained in $\mathcal{H}^2$. Moreover, the lack of convergence of all of the components of $\mathcal{H}^2$ shows that they each contribute to these poor results. This sensitivity is even more pronounced for the Gaussian approximation, due to their anomalous behavior in those regions of the molecule which are heavily weighted by $\mathcal{H}^2$.

One obvious way to improve the molecular description would be to minimize the energy variance, rather than the energy, with respect to the parameters contained in the Gaussian approximation.[2] Such a calculation has the added significance that, for systems containing more than two electrons, not only does it require a knowledge of the first- and second-order density matrices[15] [see Equation (14)], but also requires that information concerning the third-order density matrix must be obtained. In this way the wavefunction is subjected to more rigorous constraints which would consequently improve its overall description. This procedure would seem especially worthwhile, since all the integrals that arise can be calculated both accurately and conveniently. In addition, an extrapolation technique, such as the one suggested by Conroy,[16] can then be used to give an accurate approximation to the ground state energy. However, the additional constraints that such a calculation would impose on the wavefunction would necessitate the use of a more flexible basis set. Investigations of this nature are presently being undertaken.

6. REFERENCES

1. For applications of this technique to molecular systems, see, for example, R.E. Christofferson, J. Chem. Phys., 41, 960 (1964) and D.D. Ebbing, J. Chem. Phys., 36, 1361 (1962).

2. G.L. Caldow and C.A. Coulson, Proc. Camb. Phil. Soc., 57, 341 (1961). H. Conroy, J. Chem. Phys., 41, 1327 (1964). T.L. Bailey and J.L. Kinsey, Technical Note No. 45, Quantum Chemistry Group, Uppsala University (1960).

3. G. Temple, Proc. Roy. Soc., (London), A119, 276 (1928).

4. A.F. Stevenson and M.F. Crawford, Phys. Rev., 54, 375 (1938).

5. A. Weinstein, Proc. Nat. Acad. Sci. (U.S.), 20, 529 (1934).

6. See, for example, N. Solony, C.S. Lin and F.W. Birss, J. Chem. Phys. 45, 976 (1966), and references therein. See also H. Conroy, J. Chem. Phys., 41, 1331 (1964).

7. M.E. Schwartz and L.J. Schaad, J. Chem. Phys., 46, 4112 (1967).

8. M.E. Schwartz and L.J. Schaad, J. Chem. Phys., 47, 5325 (1967). See also M.E. Schwartz, Ph.D. Thesis, Vanderbilt University.

9. S.F. Boys, Proc. Roy. Soc., A200, 542 (1950).

10. H. Shull and G.G. Hall, Nature, 184, 1559 (1959).

11. W. Kolos and C.C.J. Roothaan, Rev. Mod. Phys., 32, 219 (1960).

12. M.E. Schwartz, Chem. Phys. Letters, 1, 269 (1967); also, M.E. Schwartz, Proc. Phys. Soc., 90, 51 (1966).

13. A.A. Frost, J. Chem. Phys., 10, 240 (1942); A.A. Frost, R.E. Kellogg and E.C. Curtis, Rev. Mod. Phys., 32, 313 (1960).

14. H. Hellmann, "Einführung in die Quanten Chemie," Franz Deuticke and Co., Leipzig (1937), and R.P. Feynman, Phys. Rev., 56, 340 (1939).

15. P.O. Löwdin, Phys. Rev., 97, 1474 (1955); R. McWeeny, Rev. Mod. Phys., 32, 335 (1960).

16. H. Conroy, J. Chem. Phys., 41, 1336 (1964); H. Conroy, J. Chem. Phys., 47, 930 (1967).

17. D.R. Bates, K. Ledsham, and A.L. Stewart, Phil. Trans. Roy. Soc. (London) A246, 215 (1953).

18. W. Kolos and L. Wolniewicz, J. Chem. Phys., 43, 2429 (1965).

19. See reference (11). Also see F.O. Ellison and A.A. Wu, J. Chem. Phys., 47, 4408 (1967).

20. L. Wolniewicz, J. Chem. Phys., 43, 1087 (1965)

21. I. Shavitt, Methods in Computational Physics, 2, 1 (1963).

22. P. Roberts, Proc. Phys. Soc., 89, 63 (1966).

23. S. Zimering, J. Math. Phys., 8, 1266 (1967).

24. H.G. Dawson, Proc. London Math. Soc., 29, 519 (1898).

25. W.L. Miller and A.R. Gordon, J. Phys. Chem., 35, 2874 (1931).

26. B. Lohmander and S. Rittsten, Kungl. Fysiogr. Sällsk. i Lund Fork, 28, 45 (1958).

27. A.H. Stroud and D. Secrest, "Gaussian Quadrature Formulas," Prentice-Hall, Inc., N.J. (1966).

C. GEMINAL THEORY

1. INTRODUCTION

The need to carry the accuracy of calculations on molecular systems beyond that of Hartree-Fock accuracy[1] has led to the development of several approaches.[2] Among those which retain the physical intuition such as that found in Hartree-Fock-Roothaan theory, the approach using geminal theory seems to hold some promise.[3-6] Although considerable study has been done on the properties of geminals,[7-17] few ab initio calculations have been done using the theory.[18-20] One of the reasons for the paucity of such calculations lies in the difficulty in solving the equations determining the geminals. This has led investigators to the use of simplifying approximations to produce manageable equations[18], or to abandon the equations entirely, and obtain the geminals by an infinite series of orthogonal transformations[19-21] of the original basis.

In this study, a new procedure for the determination of the best separated pair geminals of a closed shell molecule is described. The method treats the set of coupled integro-differential equations which determine the geminals without simplifying assumptions, and produces an algorithm which is quadratically convergent to the desired result.

2. GEMINAL EQUATIONS AND CONNECTION TO HARTREE-FOCK-ROOTHAAN THEORY

The development of the desired algorithm will be done conveniently by first casting the equations determining the geminals in a form analagous to that found in Hartree-Fock-Roothaan theory. To accomplish this, we recall that, for a closed shell system of $2N$ electrons, the total electronic wavefunction to be used as a trial wavefunction can be written in the form of an antisymmetrized product of geminals

$$\Phi(1,2...2N) = \mathcal{A}\{G_1(1,2)\,G_2(3,4)\cdots G_n(2N-1,2N)\},\tag{33}$$

where G_μ is called a geminal, and is a function of the space and spin coordinates

of two electrons. The geminals are usually assumed to be antisymmetric, i.e.,

$$G_\mu(1,2) = - G_\mu(2,1) ,$$

so that $\mathcal{A}$ is a partial antisymmetrizer which exchanges electrons between geminals only. Also, each geminal will be written as a product of a space and spin part,

$$G_\mu(1,2) = \Lambda_\mu(1,2) \, \Theta_\mu(1,2) , \tag{34}$$

and in this study we shall consider only the case where a singlet spin function for each geminal is:

$$\Theta_\mu(1,2) = [\alpha(1) \beta(2) - \beta(1) \alpha(2)]/\sqrt{2} , \qquad \mu = 1,2\ldots,N,$$

Without loss of generality, the spatial part of the geminals can be written in natural orbital form:[22]

$$\Lambda_\mu(1,2) = \sum_{i=1}^{N_\mu} c_{\mu i} \, \chi_{\mu i}(1) \, \chi_{\mu i}^*(2) , \tag{35}$$

in which the natural orbitals are orthonormal

$$\int \chi_{\mu i}^*(1) \, \chi_{\mu i}(1) \, dV_1 = \delta_{ij} , \tag{36}$$

and the geminals are taken to be weakly orthogonal, i.e.,

$$\iint \Lambda_\mu^*(1,2) \, \Lambda_\nu(1,2) \, dV_1 \, dV_2 = \delta_{\mu\nu} . \tag{37}$$

The strongly orthogonal geminals (or separated geminals) to be employed in this study have the further restriction that

$$\int \Lambda_\mu^*(1,m) \, \Lambda_\nu(1,n) \, dV_1 = 0 \qquad (\mu \neq \nu) , \tag{38}$$

which, along with Eq. (5), implies that

$$\int \chi_{\mu i}^*(1) \, \chi_{\nu j}(1) \, dV_1 = \delta_{\mu\nu} \, \delta_{ij} . \tag{39}$$

Using a wavefunction of this form, the energy expression can be written as

$$^1E = \sum_{\mu=1}^N \left\{ 2 \sum_{i=1}^{N_\mu} c_{\mu i}^2 \, [\mu i|h|\mu i] + \sum_{i,j}^{N_\mu} c_{\mu i} \, c_{\mu j} \, [\mu i,\mu j|\mu j,\mu i] \right.$$

$$\left. + \sum_{\nu(\neq\mu)}^N \sum_{i,j} c_{\mu i}^2 \, c_{\nu j}^2 \, \left[2[\mu i,\mu i|\nu j,\nu j] - [\mu i,\nu j|\nu j,\mu i] \right] \right\} , \tag{40}$$

where

$$[\mu i|h|\mu i] = \int \chi_{\mu i}^*(1)\, h\, \chi_{\mu i}(1)\, dV, \qquad\qquad , \qquad\qquad (41)$$

$$[\alpha,\beta|\gamma,\delta] = \iint \chi_\alpha^*(1)\, \chi_\beta(1)\, \frac{1}{r_{12}}\, \chi_\gamma^*(2)\, \chi_\delta(2)\, dV_1 dV_2 \qquad , \qquad (42)$$

and

$$h = -\tfrac{1}{2}\nabla_1^2 - \sum_\alpha \frac{Z\alpha}{r_{\alpha 1}} \qquad , \qquad\qquad (43)$$

and the summation over α is taken over all nuclei.

To obtain the optimum separated geminals, the energy expression of Equation (40) must be minimized simultaneously with respect to both the occupation numbers $(c_{\mu i})$ and the natural orbitals $(\chi_{\mu i})$. Independent variation of Equation (40) with respect to the occupation numbers yields the following set of coupled eigenvalue equations

$$\sum_{i=1}^{N\mu} H_{ki}^\mu\, c_{\mu i} = \epsilon_\mu c_{\mu k} \qquad\qquad , \qquad k=1,2,\ldots \qquad (44)$$
$$\mu = 1,2\ldots,N,$$

where

$$H_{ki}^\mu = 2[\mu k|h|\mu k]\delta_{ki} + [\mu k,\mu i|\mu i,\mu k]$$

$$+ \delta_{ki} \sum_{\nu(\neq\mu)}^N \sum_{j=1}^{N\nu} c_{\nu j}^2 \left\{ 4[\mu k,\mu k|\nu j,\nu j] - 2[\mu k,\nu j|\nu j,\mu k] \right\} \quad , \qquad (45)$$

and ϵ_μ is the energy of an electron pair in the μth geminal in the average field of the other electrons. These equations can be solved satisfactorily[19] by choosing $C_{\nu 1} = 1$ and $C_{\nu j} = 0$ $(j>1)$, as the initial guess in the iterative procedure to obtain the solutions of Eq. (44), and need not concern us further.

Of greater interest are the coupled integro-differential equations that arise from the variation of Eq. (40) with respect to the natural orbitals. To show the connection to Hartree-Fock theory, as well as to aid in the later development of

the quadratically convergent algorithm, let us first rewrite the energy expression of Eq. (40) in matrix form as

$$
{}^{1}E = \sum_{\mu=1}^{N} \left\{ 2 \sum_{i=1}^{N_\mu} c_{\mu i}^2 \left(a_{\mu i}^\dagger \, H \, a_{\mu i} \right) + \sum_{i,j}^{N_\mu} c_{\mu i} \, c_{\mu j} \left(a_{\mu i}^\dagger \, K_{\mu j} \, a_{\mu i} \right) \right.
$$

$$
\left. + \sum_{\nu(\neq\mu)}^{N} \; \sum_{i,j} c_{\mu i}^2 \, c_{\nu j}^2 \, [a_{\mu i}^+ \, (2J_{\nu j} - K_{\nu j}) \, a_{\mu i}] \right\} \quad , \tag{46}
$$

where each natural orbital has been written as

$$
\chi_{\mu i} = \varrho \, a_{\mu i} \quad , \tag{47}
$$

and where ϱ is a row vector of basis orbitals, and $a_{\mu i}$ is a column vector of coefficients needed to transform the basis orbitals into the natural orbital $\chi_{\mu i}$. Also, the matrices H, $J_{\mu j}$, and $K_{\mu j}$ are Hermitian square matrices with elements $(M)_{pq}$, given by

$$
(M)_{pq} = \int \phi_p^* \, M \, \phi_q \, dV \quad , \tag{48}
$$

where M is a one electron operator chosen from Eq. (43), or

$$
J_{\nu j}(1) = \int \chi_{\nu j}^*(2) \, \chi_{\nu j}(2) \, dV_2/r_{12} \quad , \tag{49}
$$

or

$$
K_{\nu j}(1) \, \chi(1) = \int \chi_{\nu j}(1) \frac{1}{r_{12}} \, \chi_{\nu j}^*(2) \, \chi(2) \, dV_2 \quad . \tag{50}
$$

Thus, the determination of the optimum set of natural orbitals is accomplished by the determination of the optimum vectors $a_{\mu i}$.

To effect this determination, we find the variation in the energy with respect to a variation in each of the vectors, subject to the constraint that the natural

orbitals remain orthonormal. This procedure results in

$$
\delta E = 2 \sum_{\mu=1}^{N} \sum_{i=1}^{N_\mu} \delta a_{\mu i}^{\dagger} \left(F_{\mu i} a_{\mu i} - \sum_{\nu=1}^{N} \sum_{j=1}^{N_\nu} S a_{\nu j} \lambda_{\mu i, \nu j} \right)
$$

$$
+ 2 \sum_{\mu=1}^{N} \sum_{i=1}^{N_\mu} \delta a_{\mu i}^{\dagger} \left(F_{\mu i}^{*} a_{\mu i}^{*} - \sum_{\nu=1}^{N} \sum_{j=1}^{N_\nu} S^{*} a_{\nu j}^{*} \lambda_{\nu j, \mu i} \right) , \qquad (51)
$$

where

$$
F_{\mu i} = c_{\mu i}^{2} H + \sum_{j=1}^{N_\mu} c_{\mu i} c_{\mu j} K_{\mu j} + \sum_{\nu(\neq\mu)}^{N} \sum_{j=1}^{N_\nu} c_{\mu i}^{2} c_{\nu j}^{2} (2 J_{\nu j} - K_{\nu j}) . \qquad (52)
$$

and S is the overlap matrix between the basis orbitals, with elements

$$
(S)_{ij} = \int \phi_i^{*} \phi_j \, dV , \qquad (53)
$$

and $-2\lambda_{\mu i, \nu j}$ is the Lagrangian multiplier that has been introduced to assure the orthonormality of $\chi_{\mu i}^{*}$ and $\chi_{\nu j}$. The condition that $\delta E = 0$ for arbitrary vectors $\delta a_{\mu i}^{\dagger}$ and $\delta a_{\mu i}^{\dagger}$ results in

$$
F_{\mu i} a_{\mu i} = \sum_{\nu=1}^{N} \sum_{j=1}^{N_\nu} S a_{\nu j} \lambda_{\mu i, \nu j} \qquad (54)
$$

and

$$
F_{\mu i}^{*} a_{\mu i}^{*} = \sum_{\nu=1}^{N} \sum_{j=1}^{N_\nu} S^{*} a_{\nu j}^{*} \lambda_{\nu j, \mu i} . \qquad (55)
$$

From Eqs. (54) and (55) it is clear that $\lambda_{\nu j, \mu i}$ is an element of a Hermitian matrix λ, with $\lambda_{\nu j, \mu i}^{*} = \lambda_{\mu i, \nu j}$. Thus, Eqs. (54) and (55) are equivalent.

As is apparent from the form of Eq. (54), the equations determining the best natural orbitals have the same form as the equations that are encountered in multi-configuration Hartree-Fock-Roothaan theory.[23] It is not analagous to closed-shell Hartree-Fock-Roothaan theory,[24] because $F_{\mu i}$ is not invariant with respect to a unitary transformation of the basis orbitals. Thus, the reduction of Eq. (54)

to pseudo-eigenvalue equations by a unitary transformation of the basis is not applicable in this case. Instead, the following quadratically convergent algorithm has been developed[25] to obtain the desired solution of Equation (54).

3. QUADRATICALLY CONVERGENT PROCEDURE

Considering real orbitals and coefficients henceforth, it is easily shown from Eq. (54) that

$$\lambda_{\mu i, \nu j} = a^\dagger_{\nu j} F_{\mu i} a_{\mu i} , \qquad (56)$$

$$\lambda_{\nu j, \mu i} = a^\dagger_{\mu i} F_{\nu j} a_{\nu j} . \qquad (57)$$

To assure the preservation of symmetry, we take

$$\lambda_{\nu j, \mu i} = (1/2) a^\dagger_{\mu i} (F_{\mu i} + F_{\nu j}) a_{\nu j} = \lambda_{\mu i, \nu j}, \qquad (58)$$

which allows Eq. (54) to be rewritten as

$$F_{\mu i} a_{\mu i} = (1/2) S \sum_{\nu=1}^{N} \sum_{j=1}^{N_\nu} [a^\dagger_{\mu i} (F_{\mu i} + F_{\nu j}) a_{\nu j}] a_{\nu j} . \qquad (59)$$

To establish the iterative procedure, let us assume that a reasonable approximation is known for each $a_{\mu i}$ (and hence for each $F_{\mu i}$), i.e., $F^0_{\mu i}$ and $a^0_{\mu i}$, respectively. Then, the desired solutions can be written as

$$F_{\mu i} = F^0_{\mu i} + \Delta F_{\mu i} , \qquad (60)$$

and

$$a_{\mu i} = a^0_{\mu i} + \Delta a_{\mu i} , \qquad (61)$$

where terms in $(\Delta F)^2$ and $(\Delta a_{\mu i})^2$ and higher powers have been assumed to be small enough to ignore, and the set of vectors $a^0_{\mu i}$ are chosen to be orthonormal, i.e.,

$$a^{0\dagger}_{\mu i} S a^0_{\nu j} = \delta_{\mu \nu} \delta_{ij} . \qquad (62)$$

Insertion of Eqs. (60) and (61) into Eq. (59) and subsequent neglect of terms of power two or higher in (Δa) or (ΔF) gives

$$\underset{\sim\mu i}{F^O} \; \overset{\bullet}{\underset{\sim\mu i}{a}} + \overset{\bullet}{\underset{\sim\mu i}{F}} \; \Delta\underset{\sim\mu i}{a} + \Delta\underset{\sim\mu i}{F} \; \overset{\bullet}{\underset{\sim\mu i}{a}}$$

$$= (1/2) \underset{\sim}{S} \sum_{\nu=1}^{N} \sum_{j=1}^{N_\nu} \left\{ [\underset{\sim\mu i}{a^{0\dagger}} (\underset{\sim\mu i}{F^O} + \underset{\sim\nu j}{F^O}) \underset{\sim\nu j}{a^O}] \underset{\sim\nu j}{a^O} + [\underset{\sim\mu i}{a^{0\dagger}} (\underset{\sim\mu i}{F^O} + \underset{\sim\nu j}{F^O}) \underset{\sim\nu j}{a^O}] \Delta\underset{\sim\nu j}{a} \right.$$

$$+ [\Delta\underset{\sim\mu i}{a^\dagger} (\underset{\sim\mu i}{F^O} + \underset{\sim\nu j}{F^O}) \underset{\sim\nu j}{a^O}] \underset{\sim\nu j}{a^O} + [\underset{\sim\mu i}{a^{0\dagger}} (\underset{\sim\mu i}{F^O} + \underset{\sim\nu j}{F^O}) \Delta\underset{\sim\nu j}{a}] \underset{\sim\nu j}{a^O}$$

$$\left. + [\underset{\sim\mu i}{a^{0\dagger}} (\Delta\underset{\sim\mu i}{F} + \Delta\underset{\sim\nu j}{F}) \underset{\sim\nu j}{a^O}] \underset{\sim\nu j}{a^O} \right\} \qquad . \tag{63}$$

Defining

$$\underset{\sim\mu i}{B^O} = 1/2 \; \underset{\sim}{S} \sum_{\nu=1}^{N} \sum_{j=1}^{N_\nu} \underset{\sim\nu j}{a^O} [\underset{\sim\nu j}{a^{0\dagger}} (\underset{\sim\mu i}{F^O} + \underset{\sim\nu j}{F^O})] \; , \tag{64}$$

and

$$\underset{\sim\mu i, \nu j}{A^O} = 1/2 \; \underset{\sim}{S} \; \underset{\sim\nu j}{a^O} \; \underset{\sim\mu i}{a^{0}}^{\dagger} (\underset{\sim\mu i}{F^O} + \underset{\sim\nu j}{F^O}) \tag{65}$$

the use of Eqs. (57), (64) and (65) allows Eq. (63) to be written as

$$(\underset{\sim\mu i}{B^O} - \underset{\sim\mu i}{F^O}) \Delta\underset{\sim\mu i}{a} + \sum_{\nu=1}^{N} \sum_{j=1}^{N_\nu} (\underset{\sim}{S} \underset{\mu i, \nu j}{\lambda^O} + \underset{\mu i, \nu j}{A^O}) \Delta\underset{\sim\nu j}{a} - \Delta\underset{\sim\mu i}{F} \; \underset{\sim\mu i}{a^O}$$

$$= \underset{\sim\mu i}{F^O} \; \underset{\sim\mu i}{a^O} - \underset{\sim}{S} \sum_{\nu=1}^{N} \sum_{j=1}^{N_\nu} \underset{\mu i, \nu j}{\lambda^O} \underset{\sim\nu j}{a^O} - (1/2) \underset{\sim}{S} \sum_{\nu=1}^{N} \sum_{j=1}^{N_\nu} [\underset{\sim\mu i}{a^{0}}^{\dagger} (\Delta\underset{\sim\mu i}{F} + \Delta\underset{\sim\nu j}{F}) \underset{\sim\nu j}{a^O}] \underset{\sim\nu j}{a^O} \; .$$

$$\tag{66}$$

where $\underset{\mu i, \nu j}{\lambda^O}$ is formed by using the approximate solutions $\underset{\sim\mu i}{a^O}$, $\underset{\sim\nu j}{a^O}$, $\underset{\sim\mu i}{F^O}$, and $\underset{\sim\nu j}{F^O}$ in Eq. (58).

To express the dependence of $(\Delta\underset{\sim\mu i}{F})$ on the vector $\Delta\underset{\sim\mu i}{a}$, we note that

$$\chi_{\mu i} = \sum_{p=1}^{N_\mu} \phi_p \, a_{p,\mu i}$$

$$= \sum_{p=1}^{N_\mu} \phi_p \, (a^O_{p,\mu i} + \Delta a_{p,\mu i})$$

$$= \underset{\sim\mu i}{\ell \, a} + \ell \, \Delta\underset{\sim\mu i}{a} \tag{67}$$

$$= \chi^O_{\mu i} + \Delta\chi_{\mu i} \qquad . \tag{68}$$

Then, using Eqs. (48), (49), (50), (52), and (68) we see that the variation in $\underset{\sim}{F}_{\mu i}$ can be written as

$$\Delta\underset{\sim}{F}_{\mu i} = \sum_{j=1}^{N} c_{\mu i} c_{\mu j} \left[\iint \varrho^{\dagger}(1) \, (\Delta\chi_{\mu j}(1) \, \frac{1}{r_{12}} \chi_{\mu j}^{0}(2)) \varrho(2) dv_1 dv_2 + \iint \varrho^{\dagger}(1) \, (\chi_{\mu j}^{0}(1) \, \frac{1}{r_{12}} \Delta\chi_{\mu j}(2)) \varrho(2) dv_1 dv_2 \right]$$

$$+ \sum_{\nu(\neq\mu)}^{N} \sum_{k=1}^{N_\nu} c_{\mu i}^{2} c_{\nu k}^{2} \left[2\iint \varrho^{\dagger}(1) \varrho(1) \frac{1}{r_{12}} \Delta\chi_{\nu k}(2) \chi_{\nu k}^{0}(2) dv_1 dv_2 + 2\iint \varrho^{\dagger}(1)\varrho(1) \frac{1}{r_{12}} \chi_{\nu k}^{0}(2) \Delta\chi_{\nu k}(2) dv_1 dv_2 \right.$$

$$\left. - \iint \varrho^{\dagger}(1) \Delta\chi_{\nu k}(1) \frac{1}{r_{12}} \chi_{\nu k}^{0}(2) \varrho(2) dv_1 dv_2 - \iint \varrho^{\dagger}(1) \chi_{\nu k}^{0}(1) \frac{1}{r_{12}} \Delta\chi_{\nu k}(2) \varrho(2) dv_1 dv_2 \right] . \qquad (69)$$

Using this result, the first part of the last term in Eq. (66) can be written as

$$\frac{1}{2} \underset{\sim}{S} \sum_{\nu=1}^{N} \sum_{j=1}^{N_\nu} [\underset{\sim}{a}_{\mu i}^{0\dagger} \, \Delta\underset{\sim}{F}_{\mu i,\nu j} \underset{\sim}{a}_{\nu j}^{0}] \underset{\sim}{a}_{\nu j}^{0}$$

$$= \frac{1}{2} \underset{\sim}{S} \sum_{\nu=1}^{N} \sum_{j=1}^{N_\nu} \underset{\sim}{a}_{\nu j}^{0} \left\{ \sum_{\ell=1}^{N_\mu} c_{\mu i} c_{\mu \ell} \left[\underset{\sim}{a}_{\mu \ell}^{0\dagger} (K_{\mu i,\nu j}^{0} + K_{\mu i,\nu j}^{0\dagger}) \Delta\underset{\sim}{a}_{\mu \ell} \right] \right.$$

$$\left. + \sum_{\eta(\neq\nu)}^{N} \sum_{k=1}^{N} c_{\mu i}^{2} c_{\eta k}^{2} [\, \underset{\sim}{a}_{\eta k}^{0\dagger} (2J_{\mu i,\nu j}^{0\dagger} + 2J_{\mu i,\nu j}^{0} - K_{\mu i,\nu j}^{0} - K_{\mu i,\nu j}^{0\dagger}) \Delta\underset{\sim}{a}_{\eta k}] \right\}$$

$$= \frac{1}{2} \underset{\sim}{S} \sum_{\nu=1}^{N} \sum_{j=1}^{N_\nu} \underset{\sim}{a}_{\nu j}^{0} \sum_{\eta=1}^{N} \sum_{k=1}^{N_\eta} \left\{ \delta_{\eta\mu} c_{\mu i} c_{\eta k} [\underset{\sim}{a}_{\eta k}^{0\dagger} (K_{\mu i,\nu j}^{0} + K_{\mu i,\nu j}^{0\dagger})] \right.$$

$$\left. + (1-\delta_{\eta\nu}) c_{\mu i}^{2} c_{\eta k}^{2} [\underset{\sim}{a}_{\eta k}^{0\dagger} (2J_{\mu i,\nu j}^{0\dagger} + 2J_{\mu i,\nu j}^{0} - K_{\mu i,\nu j}^{0} - K_{\mu i,\nu j}^{0\dagger})] \right\} \Delta\underset{\sim}{a}_{\eta k} . \qquad (70)$$

Rearranging summations in Eq. (70), and defining the elements of a supermatrix $\underset{\sim}{M}$ as

$$(\underset{\sim}{M}^{0})_{\mu i, \eta k} = \frac{1}{2} \underset{\sim}{S} \sum_{\nu=1}^{N} \sum_{j=1}^{N_\nu} \underset{\sim}{a}_{\nu j}^{0} \left\{ \delta_{\eta\mu} c_{\mu i} c_{\eta k} [\underset{\sim}{a}_{\eta k}^{0\dagger} (K_{\mu i,\nu j}^{0} + K_{\mu i,\nu j}^{0\dagger})] \right.$$

$$\left. + (1-\delta_{\eta\nu}) c_{\mu i}^{2} c_{\eta k}^{2} [\underset{\sim}{a}_{\eta k}^{0\dagger} (2J_{\mu i,\nu j}^{0\dagger} + 2J_{\mu i,\nu j}^{0} - K_{\mu i,\nu j}^{0} - K_{\mu i,\nu j}^{0\dagger})] \right\} , \qquad (71)$$

Eq. (70) can be written as

$$\frac{1}{2} \underset{\sim}{S} \sum_{\nu=1}^{N} \sum_{j=1}^{N_\nu} [\underset{\sim}{a}_{\mu i}^{0\dagger} \, \Delta\underset{\sim}{F}_{\mu i,\nu j} \underset{\sim}{a}_{\nu j}^{0}] \underset{\sim}{a}_{\nu j}^{0} = \sum_{\nu=1}^{N} \sum_{j=1}^{N_\nu} (\underset{\sim}{M}^{0})_{\mu i, \nu j} \Delta\underset{\sim}{a}_{\nu j} . \qquad (72)$$

In a similar manner, the last part of the last term in Eq. (66) can be written as

$$\frac{1}{2} \underset{\sim}{S} \sum_{\nu=1}^{N} \sum_{j=1}^{N_\nu} [a_{\mu i}^{O\dagger} \Delta F_{\nu j} a_{\nu j}^{O}] a_{\nu j}^{O} = \sum_{\nu=1}^{N} \sum_{j=1}^{N_\nu} (\underset{\sim}{N}^{O})_{\mu i, \nu j} \Delta a_{\nu j} \quad , \tag{73}$$

where

$$(\underset{\sim}{N}^{O})_{\mu i, \eta k} = \frac{1}{2} \underset{\sim}{S} \sum_{\nu=1}^{N} \sum_{j=1}^{N_\nu} a_{\nu j}^{O} \left\{ \delta_{\eta \nu} c_{\nu j} c_{\eta k} [a_{\eta k}^{O\dagger} (\underset{\sim}{K}_{\mu i, \nu j}^{O} + \underset{\sim}{K}_{\mu i, \nu j}^{O\dagger})] \right.$$
$$\left. + (1-\delta_{\nu\eta}) c_{\nu j}^2 c_{\eta k}^2 [a_{\eta k}^{O\dagger} (2 \underset{\sim}{J}_{\mu i, \nu j}^{O\dagger} + 2 \underset{\sim}{J}_{\mu i, \nu j}^{O} - \underset{\sim}{K}_{\mu i, \nu j}^{O} - \underset{\sim}{K}_{\mu i, \nu j}^{O\dagger})] \right\}. \tag{74}$$

Finally, we note that the other term of interest in Eq. (66) can be expressed as

$$\Delta F_{\mu i} a_{\mu i}^{O} = \sum_{\nu=1}^{N} \sum_{j=1}^{N_\nu} \underset{\sim}{D}_{\mu i, \nu j}^{O} \Delta a_{\nu j} \quad , \tag{75}$$

where

$$(\underset{\sim}{D}^{O})_{\mu i, \nu j} = \delta_{\mu\nu} c_{\mu i} c_{\nu j} (\underset{\sim}{J}_{\mu i, \nu j}^{O\dagger} + \underset{\sim}{K}_{\mu i, \nu j}^{O}) + (1-\delta_{\mu\nu}) c_{\mu i}^2 c_{\nu j}^2 [4 \underset{\sim}{K}_{\mu i, \nu j}^{O\dagger} - \underset{\sim}{J}_{\mu i, \nu j}^{O\dagger} - \underset{\sim}{K}_{\mu i, \nu j}^{O}]. \tag{76}$$

Collecting the results obtained thus far, we find that Eq. (66) can be written as

$$\underset{\sim}{G}^{O} \Delta a = g^{O} \quad , \tag{77}$$

where the elements of the supermatrices in Eq. (77) are given by

$$(\underset{\sim}{G}^{O})_{\mu i, \nu j} = \delta_{\mu\nu} \delta_{ij} (\underset{\sim}{B}_{\mu i}^{O} - \underset{\sim}{F}_{\mu i}^{O}) \tag{78}$$
$$+ \underset{\sim}{S} \lambda_{\mu i, \nu j} + \underset{\sim}{A}_{\mu i, \nu j}^{O} - \underset{\sim}{D}_{\mu i, \nu j}^{O} + \underset{\sim}{M}_{\mu i, \nu j}^{O} + \underset{\sim}{N}_{\mu i, \nu j}^{O} \quad ,$$

and

$$g_{\mu i}^{O} = \underset{\sim}{F}_{\mu i}^{O} a_{\mu i}^{O} - \underset{\sim}{S} \sum_{\nu=1}^{N} \sum_{j=1}^{N_\nu} \lambda_{\mu i, \nu j}^{O} a_{\nu j}^{O} \quad . \tag{79}$$

4. DISCUSSION

The solution of Eq. (77) for Δa provides an iterative procedure of the Newton-Raphson type, which can be expected to be quadratically convergent[26] to the desired result for a sufficiently good set of starting vectors. The analysis presented here is similar in form to a quadratically convergent algorithm developed by Wessel[25] for solving the general Hartree-Fock-Roothaan equations. The present work differs from Wessel's in that the equations arise from the separated pair model, and the dependence of the Fock matrices $\underset{\sim}{F}_{\mu i}$ upon the vectors $\Delta a_{\mu i}$ has been explicitly evaluated.[27]

Considering the convergence properties of the proposed procedure, direct calculation of the natural orbitals of a geminal trial function by this algorithm should provide a favorable alternative to the method of 2 x 2 rotations[19-21] that is often employed. Furthermore, it has not been necessary to neglect any off-diagonal Lagrangian multipliers[2,18] in the above analysis in order to obtain the desired algorithm.

Concerning the use of this algorithm, several comments are appropriate. For atomic calculations, the coefficients obtained from a Gram-Schmidt orthogonal-ization of the entire set of orbitals should serve as suitable starting vectors $a^0_{\mu i}$. In the case of a molecular calculation, the principal natural orbitals (i.e., the first natural orbital $\chi_{\mu 1}$ in each geminal expansion) may be approximated by the canonical Hartree-Fock orbitals, or perhaps by localized Hartree-Fock orbitals. It should be noted that the Hartree-Fock orbitals may be obtained within the framework of this algorithm by simply terminating the natural orbital expansion of each geminal to one term and hence setting $c_{\mu 1} = 1$. In approximating the weakly occupied natural orbitals $(\chi_{\mu i}, i > 1)$ of a molecular calculation, there are several possibilities. One could use the virtual orbitals obtained from the Hartree-Fock calculation as the initial approximation to the weakly occupied natural orbitals. Alternatively, one could construct molecular orbitals of the proper symmetry, and orthogonalize these orbitals to the principal natural orbitals and to each other. Once the starting vectors are chosen, both the atomic and molecular calculations would proceed in the same manner, with the elements of G^0 and g^0 being determined. A correction vector Δa is determined from Eq. (77), and is added to a^0, forming a new set of starting vectors, $a'_{\mu i}$. These corrected vectors are then Gram-Schmidt orthogonalized to insure their orthonormality and acceptability as new starting vectors. The iteration process is repeated until $\Delta a \rightarrow 0$.

Finally, it should be pointed out that the procedure of solving Eq. (77) will give the best set of natural orbitals for a given set of occupation coefficients

$c_{\mu i}$. In order to obtain the best separated geminal wavefunction, a macroiteration cycle should be performed, shuttling back and forth between Eqs. (44) and (77).

One might find it computationally convenient for the $\underset{\sim}{G}^O$ matrix to be symmetric. In the work by Wessel,[25] a symmetric $\underset{\sim}{G}^O$ matrix was obtained by a procedure which might be employed here in a similar manner. Neglecting second order terms, one has, from the orthonormality relationship of the vectors,

$$\underset{\sim}{a}^{O\dagger}_{\nu j} \underset{\sim}{S} \Delta \underset{\sim}{a}_{\mu i} + \underset{\sim}{a}^{O\dagger}_{\mu i} \underset{\sim}{S} \Delta \underset{\sim}{a}_{\nu j} = 0 \quad , \tag{80}$$

from which one may obtain

$$\frac{1}{2} \sum_{\nu=1}^{N} \sum_{j=1}^{N_\nu} \left\{ (\underset{\sim}{F}^O_{\mu i} + \underset{\sim}{F}^O_{\nu j}) \underset{\sim}{a}^O_{\nu j} \underset{\sim}{a}^{O\dagger}_{\nu j} \underset{\sim}{S} \Delta \underset{\sim}{a}_{\mu i} + (\underset{\sim}{F}^O_{\mu i} + \underset{\sim}{F}^O_{\nu j}) \underset{\sim}{a}^O_{\nu j} \underset{\sim}{a}^{O\dagger}_{\mu i} \underset{\sim}{S} \Delta \underset{\sim}{a}_{\nu j} \right\} = 0 \quad , \tag{81}$$

which can be rewritten as

$$\underset{\sim}{B}^{O\dagger}_{\mu i} \Delta \underset{\sim}{a}_{\mu i} + \sum_{\nu=1}^{N} \sum_{j=1}^{N_\nu} \underset{\sim}{A}^{O\dagger}_{\mu i, \nu j} \Delta \underset{\sim}{a}_{\nu j} = 0 \quad . \tag{82}$$

Similar considerations concerning $\underset{\sim}{M}^O_{\mu i, \nu j}$, $\underset{\sim}{N}^O_{\mu i, \nu j}$, and $\underset{\sim}{D}^O_{\mu i, \nu j}$, and addition to Eq. (78) of identities such as Eq. (82) are necessary if it is desired to complete the symmetrization process of $\underset{\sim}{G}^O$.

Applications of the analysis presented here are presently underway on various atomic and molecular systems, and will be analyzed and reported separately in future studies.

5. REFERENCES

1. For a discussion of this necessity, see, for example, P. O. Löwdin, Adv. Chem. Phys., $\underline{2}$, 207 (1959); R. Nesbet, Adv. Chem. Phys., $\underline{9}$, 321 (1965).

2. For example, see A. C. Wahl, P. J. Bertoncini, G. Das and T. L. Gilbert, Int. J. of Quantum Chem., $\underline{1}$, 123 (1967); J. Hinze and C. C. J. Roothaan, Prog. Theor. Phys. (Kyoto), Suppl. $\underline{40}$, 37 (1967); C. F. Bender and E. R. Davidson, J. Phys. Chem., $\underline{70}$, 2675 (1966); W. Kutzelnigg, J. Chem. Phys., $\underline{40}$, 3640 (1964); O. Sinanoğlu, J. Chem. Phys., $\underline{36}$, 706, 3198 (1962); R. K. Nesbet, Phys. Rev., $\underline{155}$, 51 (1967).

3. A. C. Hurley, J. Lennard-Jones and J. Pople, Proc. Roy. Soc. (London), $\underline{A220}$, 446 (1953).

4. T. L. Allen and H. Shull, J. Phys. Chem., $\underline{66}$, 2281 (1962).

5. D. D. Ebbing and L. E. Poplawski, J. Chem. Phys., $\underline{45}$, 2657 (1966); D. D. Ebbing and A. Tanin, J. Chem. Phys., $\underline{48}$, 4300 (1968).

6. M. Klessinger and R. McWeeny, J. Chem. Phys., $\underline{42}$, 3343 (1965); R. McWeeny and K. Ohno, Proc. Roy. Soc. (London), $\underline{A255}$, 367 (1960); R. McWeeny and B. T. Sutcliffe, Proc. Roy. Soc. (London), $\underline{A273}$, 103 (1963).

7. J. M. Parks and R. G. Parr, J. Chem. Phys., $\underline{28}$, 335 (1958).

8. T. Arai, J. Chem. Phys., $\underline{33}$, 95 (1960).

9. P. O. Löwdin, J. Chem. Phys., $\underline{35}$, 78 (1961).

10. E. Kapuy, Phys. Letters, $\underline{1}$, 205 (1962); Theoret. Chim. Acta, $\underline{3}$, 379 (1965); $\underline{6}$, 281 (1966); Acta Phys. Acad. Sci. Hung., $\underline{9}$, 237 (1953); $\underline{11}$, 409 (1960).

11. W. Kutzelnigg, Theoret. Chim. Acta, $\underline{1}$, 317 (1963); $\underline{1}$, 343 (1963); $\underline{3}$, 241 (1965).

12. C. S. Lin and F. W. Birss, Theoret. Chim. Acta, $\underline{5}$, 373 (1966).

13. R. McWeeny and E. Steiner, Adv. Quantum Chem., $\underline{2}$, 93 (1965).

14. H. F. King, J. Chem. Phys., $\underline{46}$, 705 (1967).

15. S. Huzinaga, IBM Tech. Report, Yorktown Hgts., 1964.

16. M. Krauss and A. Weiss, Rev. Mod. Phys., $\underline{32}$, 179 (1960).

17. R. McWeeny, Proc. Roy. Soc. (London), $\underline{A253}$, 242 (1959); Rev. Mod. Phys., $\underline{32}$, 335 (1960); R. McWeeny and S. Mizuno, Proc. Roy. Soc. (London), $\underline{A259}$, 554 (1961).

18. R. Alrichs and W. Kutzelnigg, J. Chem. Phys., $\underline{48}$, 1819 (1968); R. Alrichs, W. Kutzelnigg and W. A. Bingel, Theoret. Chim. Acta, $\underline{5}$, 289 (1966); $\underline{5}$, 305 (1966).

19. K. J. Miller and K. Ruedenberg, J. Chem. Phys., $\underline{48}$, 3414 (1968); $\underline{48}$, 3444 (1968); $\underline{48}$, 3450 (1968).

20. D. D. Ebbing and R. C. Henderson, J. Chem. Phys., $\underline{42}$, 2225 (1965).

21. C. E. Reid and Y. Öhrn, Rev. Mod. Phys., $\underline{35}$, 445 (1963).

22. P. O. Löwdin, Phys. Rev., $\underline{97}$, 1474 (1955).

23. J. Hinze and C. C. J. Roothaan, Reference 2.

24. C. C. J. Roothaan, Rev. Mod. Phys., $\underline{23}$, 69 (1951).

25. Similar analyses within Hartree–Fock and multi-configuration SCF theory have been made by T. H. Brown and R. L. Taylor, J. Phys. Chem., $\underline{69}$, 2316 (1965); W. R. Wessel, J. Chem. Phys., $\underline{47}$, 3253 (1967); T. H. Brown, J. Chem. Phys., $\underline{49}$, 2291 (1968); J. Hinze and C. C. J. Roothaan, Reference 2.

26. A. Ralston, "A First Course in Numerical Analysis," McGraw-Hill (1965), p. 332.

27. The dependence of the Fock matrices upon the vectors Δa has been treated in the case of multi-configuration SCF theory by Hinze and Roothaan (Reference 2).

III. SPECTROSCOPIC INVESTIGATIONS OF TRANSIENT SPECIES

A. ENERGY TRANSFER IN NAPHTHALENE-BIACETYL MIXTURES

1. INTRODUCTION

One of the proposed methods of generating appreciable concentrations of excited-state molecules is that of photosensitization. While our principal aim is the investigation of these excited species by microwave spectroscopy, we have found that there is a great need for investigation of the primary photosensitization process and its energy transfer mechanism and efficiency. This last point is particularly important for the microwave investigations, since efficient modes of production of the excited species are necessary in order to overcome detection sensitivity problems.

To be more specific, the photosensitization processes in which we are interested are those in which an electronically excited molecule transfers its energy to another ground state molecule by a radiationless process. Of the possible types, only those processes involving triplet state donors will be very effective, since singlet donors do not usually exist for a sufficient length of time. Although triplet→singlet (T-S) processes have been known for many years,[1] the analogous triplet→triplet (T-T) process has been established for only a relatively short time.[2] In general the mechanism of the transfer processes is poorly known, although several theoretical discussions have emphasized the importance of dipole-dipole and exchange interactions between donor and acceptor.[3]

In this work we have investigated the gas-phase transfer efficiency between triplet naphthalene and singlet biacetyl to form triplet biacetyl (T-T process). The few similar investigations previously reported include the benzene-biacetyl system[4] and the hexafluoroacetone-biacetyl system.[5] Some more preliminary studies of other donors and acceptors have also been undertaken in our laboratory.

2. METHOD OF ANALYSIS OF ENERGY TRANSFER

While several other energy transfer modes might be considered, we limit ourselves here to those shown in Figure III-1. B indicates biacetyl, N indicates naphthalene, superscripts give the multiplicity of the states, and subscripts 0 and 1 indicate lowest and first excited states, respectively. The straight lines are processes involving absorption or emission of radiation while the wiggly lines are radiationless energy transfer processes. The $^3N_0$ level lies at 21,200 cm^{-1}, the $^3B_0$ at 20,500 cm^{-1}, and the $^1B_1$ at about 22,600 cm^{-1}.[6] The energy levels are shown as single discrete states although this is not meant to imply the absence of vibrational fine structure.

It has been well-established for some time that irradiation of naphthalene at 2537 $\overset{o}{A}$ leads to effective population of the $^3N_0$ state. Because of the near resonance of the $^3B_0$ and $^3N_0$ levels it was believed that there should be efficient energy transfer from triplet naphthalene to ground state biacetyl. This has been observed by irradiating naphthalene-biacetyl mixtures with 2537 $\overset{o}{A}$ light. Under these conditions, experiments performed with a Hilger medium-quartz photographic spectrograph show that there is essentially no biacetyl fluorescence from $^1B_1$ states, but only phosphorescence
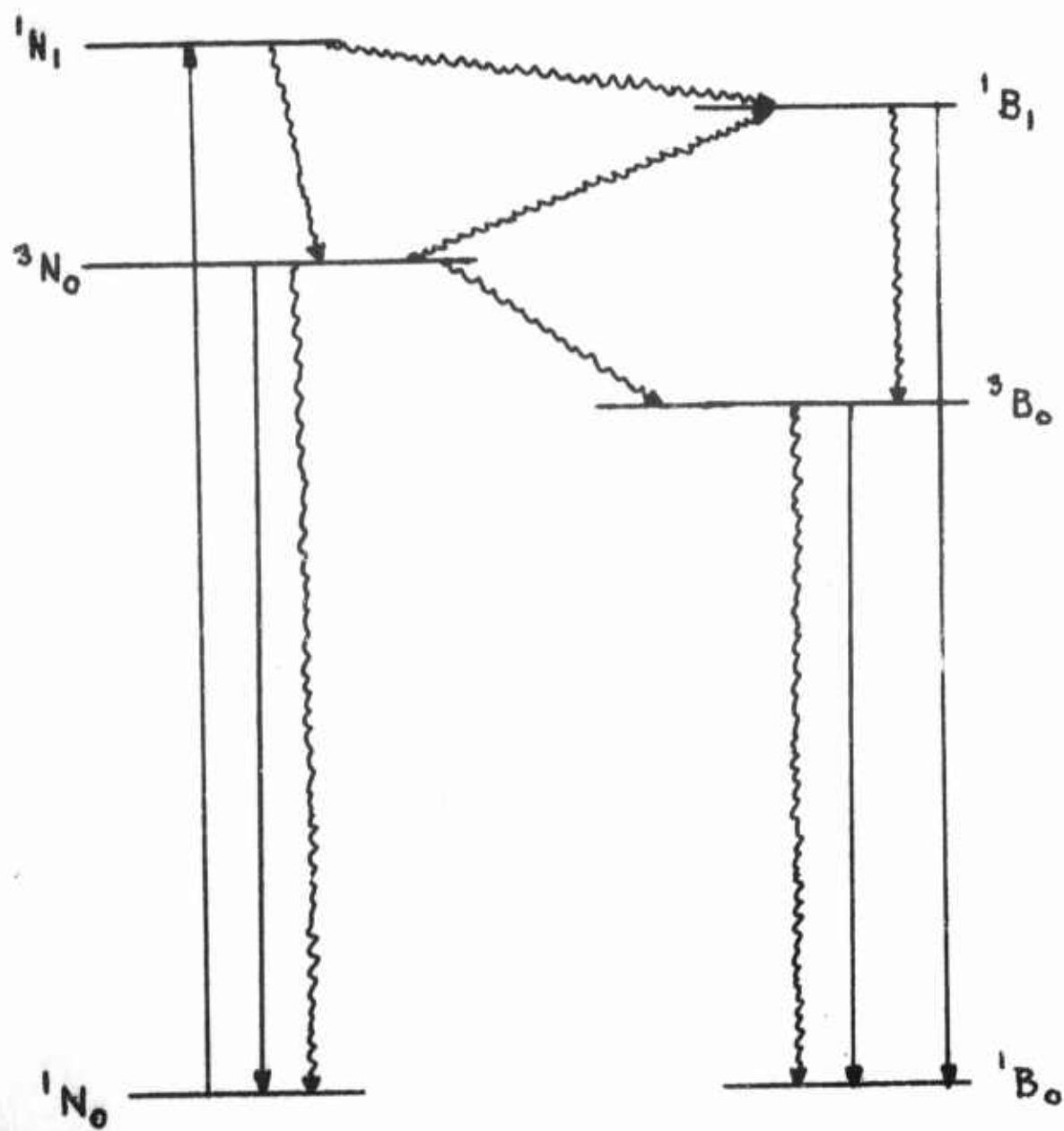
Figure III-1.   Inter- and intra-molecular energy transfer schemes
in naphthalene-biacetyl mixtures.

from $^3B_0$. Also, no naphthalene phosphorescence is observed. From these results we conclude (1) that the $^1B_1$ level is not excited; that is, no S-S energy transfer occurs, (2) that the non-radiative processes destroying $^3N_0$ are very effective, and (3) that $^3B_0$ is produced from $^3N_0$ by T-T energy transfer.

Based on this mechanism the sensitized phosphorescence intensity can be written

$$I_{SP}(2537) = I_N(2537) \cdot \Phi_{ISC} \cdot \Phi_{SP} \qquad (1)$$

where $I_N(2537)$ is the light intensity absorbed by naphthalene at 2537 $\overset{o}{A}$, Φ_{ISC} is the intersystem ($^1N_1 \rightarrow {}^3N_0$) crossover efficiency, and Φ_{SP} is the quantum yield of the phosphorescence, that is, it is the fraction of $^3N_0$ molecules which eventually produce biacetyl phosphorescence. If now the $^1B_1$ system is excited with 4358 $\overset{o}{A}$ radiation, the direct phosphorescence of biacetyl is observed. The intensity of direct phosphorescence may be written

$$I_P(4358) = I_N(4358) \cdot \Phi_P \qquad (2)$$

where Φ_P is the fraction of $^1B_1$ molecules which eventually lead to phosphorescing $^3B_0$ molecules. Combining Equations (1) and (2), we get

$$\Phi_{SP} = \left(\frac{I_{SP}}{I_P}\right)\left(\frac{I_B(4358)}{I_N(2537)}\right)\left(\frac{\Phi_P}{\Phi_{ISC}}\right) \qquad (3)$$

By Equation (3) it is possible to calculate Φ_{SP} relative to Φ_P (which has a value of 0.15).[7] The first two ratios in Equation (3) can be measured

experimentally, and reasonable estimates or limits can be placed upon the intersystem crossing efficiency, Φ_{ISC}. It is eventually of interest to know Φ_{TT}, the triplet-triplet transfer efficiency, which can be defined by Equation (4).

$$\Phi_{SP} = \Phi_{TT}\Phi_P \qquad (4)$$

This equation involves the assumption that all molecules which get into the $^1B_1$ state cross over into the $^3B_0$. Previous evidence indicates that this is correct to within 2%. Then Equation (3) can be written

$$\Phi_{TT} = \left(\frac{I_{SP}}{I_P}\right)\left(\frac{I_B(4358)}{I_N(2537)}\right)\left(\frac{1}{\Phi_{ISC}}\right) \qquad (5)$$

3. EXPERIMENTAL

a. Measurement of Phosphorescence Intensity Ratios

Although it is a task of great difficulty to measure absolute phosphorescence intensities, the measurement of relative phosphorescence intensities is relatively easy. The principle components of the instrumentation used for these measurements are shown in Figure III-2. The gas sample being irradiated is contained in the pyrex T-shaped cell, C, which is fitted with quartz windows. The long portion of the cell is 20 mm in diameter while the sidearm has a diameter of 10 mm. This sidearm is positioned such that its center is $7\frac{1}{2}$ cm from the entrance window.

Irradiation of the samples is performed by use of the mercury vapor source, F, the monochromator, E, and the collimator, D. Bausch and Lomb HP-100 and SP-200 mercury vapor sources have been used for most measurements.

126

Figure III-2. Phosphorescence apparatus schematic.

A – Analysing monochromator
B – Photomultiplier
C – Sample cell
D – Collimator
E – High-pass monochromator
F – Mercury vapor lamp
G – Photometer
H – Recorder

The monochromator, E, is a Bausch and Lomb high-intensity grating instrument fitted with a grating having 1200 lines/mm. With this grating the mono-chromator may be used for irradiation anywhere within the 2000 $\overset{o}{A}$ - 7000 $\overset{o}{A}$ region.

Phosphorescence (or fluorescence) is observed at the sidearm of the T-cell by the scanning monochromator, A, a 0.3 meter McPherson Model 218 plane-grating instrument. The 1200 line/mm grating provides a wavelength range of 1050 $\overset{o}{A}$ - 10,000 $\overset{o}{A}$ with a linear dispersion of 26.5 $\overset{o}{A}$/mm. Detection is accomplished by the photomultiplier assembly, B, a McPherson Model 650 unit fitted with an EMI 9514B photomultiplier.

The high voltage for the photomultiplier is supplied via cable **b** from an Eldorado Model 201 Universal Photometer, which also serves for measuring the photomultiplier output signal via cable **a**. The photometer output drives a Bausch and Lomb VOM-6, 2.5 mv strip-chart recorder for permanent display of the emission signals. To decrease pen jitter on the sensitive photometer and recorder scales, an RC filter with a time constant variable in the range 0-1 second has been attached at the recorder input.

In a typical experiment on the biacetyl-naphthalene system the biacetyl phosphorescence intensities are measured in some convenient units (μamps, say) with irradiating wavelengths of 2537 $\overset{o}{A}$ and 4358 $\overset{o}{A}$. During these measurements the geometry of the system is unchanged, and since the photomultiplier is operated in its linear region the phosphorescence intensity ratio I_{SP}/I_P is easily obtained.

In most measurements that we have performed the phosphorescence intensities were measured as the peak heights of the $^3B_0 \rightarrow {}^1B_0$ band at ~5100 $\overset{o}{A}$ as observed

on the recorder tracings. We have also evaluated the intensities in some cases by integrating over the entire phosphorescence band. The ratios I_{SP}/I_P evaluated by this method have been found to be within 5-10% of those obtained from peak heights, so the majority of our measurements have utilized the simpler peak height method.

In typical runs the phosphorescence band is scanned several times to both higher and lower wavelengths and the average peak height is obtained from these scans. Figure III-3 shows a typical pair of scans over the 5100 $\overset{o}{A}$ biacetyl phosphorescence band.

b. __Measurement of the Ratio of Absorbed Light Intensity__

The ratio of the number of photons absorbed at the two wavelengths has been measured in an indirect fashion. What is needed is $I_B(4358)/I_N(2537)$ in the region of phosphorescence observed through the sidearm T of the sample cell. By straightforward but tedious algebra, it can be shown that

$$\frac{I_B(4358)}{I_N(2537)} = \frac{\dfrac{10^{A_2(B)}-10^{A_1(B)}}{10^{[A_1(B)+A_2(B)]}}}{\dfrac{10^{A_2(N)}-10^{A_1(N)}}{10^{[A_1(N)+A_2(N)]}}} \cdot \frac{I_0(4358)}{I_0(2537)} \qquad (6)$$

where $A_2(B)$ = absorbance of biacetyl at 4358 $\overset{o}{A}$ at some distance l_2, $A_1(B)$ = absorbance of biacetyl at 4358 $\overset{o}{A}$ at some distance l_1, $A_2(N)$ and $A_1(N)$ are the same quantities for naphthalene at 2537 $\overset{o}{A}$, $I_0(4358)$ = the incident intensity at 4358 $\overset{o}{A}$ in photons/sec, and $I_0(2537)$ = the incident intensity at 2537 $\overset{o}{A}$ in photons/sec. For our particular cell geometry we take $l_1 = 7$ cm and $l_2 = 8$ cm.
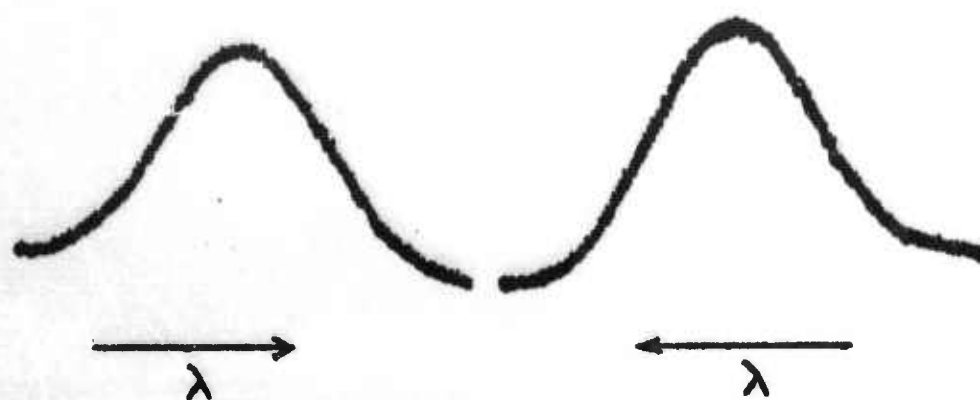
Figure III-3. Successive scans of biacetyl phosphorescence band
to higher and lower wavelength.

The absorbances in Equation (6) have been determined in the following manner. A 10 cm gas cell was filled in all runs with a gas mixture that was identical to that used in the T-shaped phosphorescence cell. The absorbances of the biacetyl and the naphthalene were then measured on a Bausch and Lomb Spectronic 505 spectrophotometer. In these measurements it was necessary to subtract the small biacetyl absorbance at 2537 $\overset{o}{A}$ from the total in order to obtain the absorbance of naphthalene.[4] The values obtained by this method need only be multiplied by 7/10 or 8/10 to give A_1(B or N) and A_2(B or N) of Equation (6).

Equation (6) was derived with the assumption that the two components strictly obey Beer's Law individually and when mixed. Although some deviation from Beer's Law behavior is expected, our measurements and those of others have shown that in the pressure range of interest (30 or 40 torr total pressure) the deviations should produce errors of no more than five percent.[4]

The ratio of incident light intensities is then the only measureable quantity remaining in Equation (6). This has been measured by interposing the detector element of a Kettering Model 8301 radiometer in the path of the light beam before it enters the sample cell. A direct reading in erg cm^{-2} sec^{-1} is obtained for each wavelength. Appropriate conversion to photons sec^{-1} leads directly to the desired ratio, $I_0(4358/I_0(2537)$. Stated accuracy of the radiometer is 5%, and the reproducibility seems to be about 2%.

Some attempts were made to calibrate the radiometer by ferrioxalate actinometry.[8] Since, however, the actinometry experiments had an uncertainty

of about 10%, it was possible to show only that the radiometer was accurate to within this limit.

In most cases no attempt was made to perform accurate direct pressure measurements of the biacetyl-naphthalene mixtures. Instead, we have used the Spectronic 505 absorbance measurements with the known values of the extinction coefficients[4,6] to provide an indirect but consistent pressure determination for each component.

4. RESULTS FOR NAPHTHALENE-BIACETYL SYSTEM

Table III-I gives the measured phosphorescence ratios I_{SP}/I_P for seven different runs. The value of $\epsilon_B C_B$ is given for each of these runs, where ϵ_B and C_B are the extinction coefficient and concentration in moles/liter, respectively, of biacetyl. With the average value of $\epsilon_B = 10.2$, C_B and hence the partial pressure of biacetyl are easily obtained.

In Table III-II we have listed the experimental values of $I(4358)/I(2537)$ for the seven runs of Table III-I. The rather large variations in these values are produced by two factors: (1) changes in incident light intensity ratios, and (2) changes in the fraction of radiation absorbed in the viewing region. We found large variations in the incident light intensity ratios from day to day and even from hour to hour. However, in Runs 6 and 7, the large difference is caused by the use of a different SP-200 UV light source. Also listed in Table III-II are $\epsilon_N C_N$ (which is determined only by the vapor pressure of naphthalene at room temperature) and $I_0(4358)/I_0(2537)$.

When the experimental values of Tables III-I and III-II are substituted into Equation (3), along with the value $\varphi_P = 0.15$, we obtain the values of $\Phi_{SP}\Phi_{ISC}$ given in Table III-III. The average value has been listed as

Table III-I. Ratio of Sensitized to Direct Phosphorescence

Intensities for Biacetyl at Different Pressures

Run	$\epsilon_B C_B$	I_{SP}/I_P
1	.0183	.0374
2	.0079	.0399
3	.0037	.0762
4	.0176	.0185
5	.0147	.0180
6	.0322	.0263
7	.0169	.0423

Table III-11. Measured Values of the Ratio of the Number

of Photons Absorbed at the Two Wavelengths.

Also listed are $\epsilon_N C_N$ and incident light intensity ratios.

Run	$\epsilon_N C_N$	$I_o(4358)/I_o(2537)$	$I_B(4358)/I_N(2537)$
1	.0123	3.22	5.25
2	.0160	8.21	5.16
3	.0214	8.21	2.14
4	.0153	9.61	10.38
5	.0143	11.03	11.16
6	.0142	0.570	0.948
7	.0125	0.691	0.856

Table III-III. Sensitized Phosphorescence Quantum Yields
Times Φ_{ISC} (for $^1N_1 \rightarrow {}^3N_0$).

Run	$\Phi_{SP} \cdot \Phi_{ISC}$
1	.027
2	.030
3	.024
4	.029
5	.030
6	.037
7	.033

Average = 0.030 ± 0.003

0.030 ± 0.003, from which it is possible to calculate [from Equation (4)]

$$\Phi_{TT}\Phi_{ISC} = 0.20$$

From the latter two results we also have

$$\frac{\Phi_{TT}}{\Phi_{SP}} = 6.7$$

From the results of Table III-III we found a statistical uncertainty of ±0.003. It should be mentioned that several more runs were performed, but for any of several reasons these results were thrown out. The sources of error which might occur include (1) system geometry changes, (2) impurities, (3) photometer and/or radiometer calibration errors, and (4) lamp intensity variations. With regard to (1), it was important that no geometry changes in the optical path occurred during the irradiations at 4358 and 2537 Å. Some runs were thrown out for reasons attributable to this factor. The major impurity that was guarded against was oxygen because of its well-known quenching abilities.[9] Naphthalene and biacetyl samples were well degassed and were handled on high vacuum lines. In this connection it is worth mentioning that no appreciable changes in phosphorescence intensities occurred over the period of several hours so no appreciable photolytic decomposition[10] of biacetyl was caused by the rather mild irradiations.

Instrument calibrations are still of some concern to us, but we believe that the cumulative errors from these factors could be no more than 10-15%. We mentioned previously the possibility that the peak height phosphorescence intensities might be in error. These results were checked in several runs against the integrated intensities. A typical set of results for two runs are given in Table III-IV.

Table III-IV.   Integrated Versus Peak Height

Phosphorescence Intensity Ratios

August 26 Data

Run	I_{SP}/I_P (Peak)	I_{SP}/I_P (Integrated)
I	.568	.574
II	.185	.201
III	.318	.312

August 27 Data

I	.374	.349
II	.290	.293
III	.257	.243

The problem which caused the most difficulty was the variation of lamp intensity ratios with time. Many bad sets of data were obtained and discarded before the magnitude of this problem was fully appreciated. It was found that after the Bausch and Lomb SP-200 lamp was on for a sufficient period of time the intensities of 2537 and 4358 $\overset{\circ}{A}$ radiation varied smoothly but were not ever constant or reproducible from day to day. Figure III-4 shows plots of these variations versus time that were obtained on two successive days with the same lamp. Because of these variations we took great care to perform the phosphorescence measurements as rapidly as possible. In many cases the lamp intensity ratio was measured before and after each run to insure that the variation during the run was not too great. In any case, we believe this is probably the major source of our errors, since it is difficult to be certain that it has been eliminated. We hope to obtain a more stable lamp so that this problem may be definitely eliminated.

5. DISCUSSION

In this study it was not possible to achieve concentrations such that naphthalene would be in excess, since the naphthalene pressure was limited to the equilibrium vapor pressure at ambient room temperature (approximately 75 microns). For this reason it was not possible to investigate the expected sigmoidal[11] Φ_{SP} versus pressure curve. Hence our results are best compared to the benzene-biacetyl results for $P(\text{biacetyl})/P(C_6H_6) \gg 1$. For these conditions Ishikawa and Noyes found $\Phi_{SP} \sim 0.02$. In our work, $\Phi_{SP} \cdot \Phi_{ISC} = 0.03$. The value of Φ_{ISC} is unknown, but has a value of 0.39 in solution.[12] If this value were valid in the gas phase we would get $\Phi_{SP} = 0.077$, which is somewhat larger than the benzene-biacetyl result at comparable conditions. We would also predict $\varphi_{TT} = 0.51$ from our results.
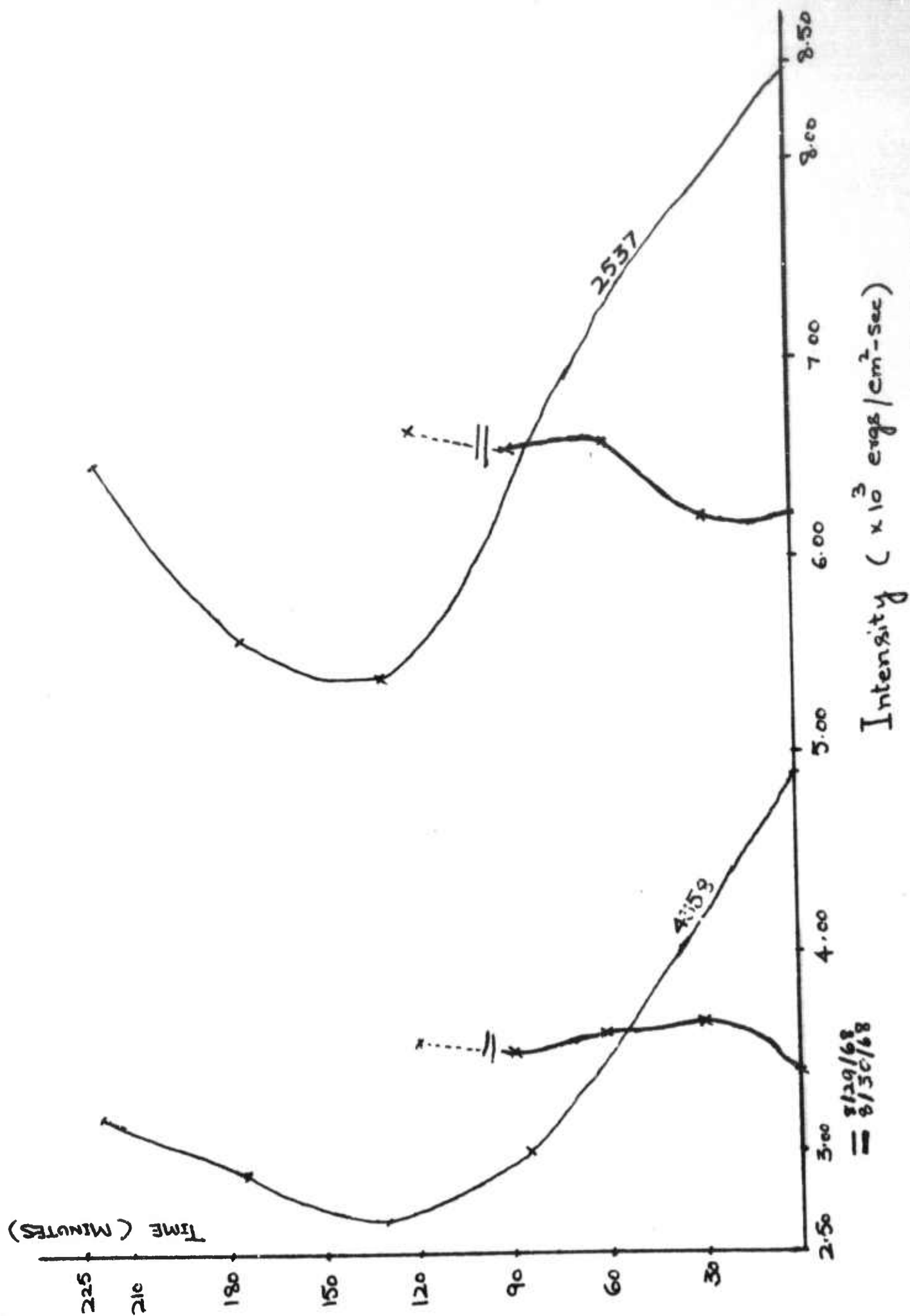
138

Figure III-4. Variation of SP-200 lamp intensity with time.

Actually, the intersystem crossing efficiency for benzene is larger in the gas phase than in solution[12] so a similar result would not be unreasonable for naphthalene. If this were the case the value of Φ_{TT} permitted by our data would have to decrease, however. For example, if $\Phi_{ISC} = 0.78$ (the value for benzene in gas phase), our data would yield $\Phi_{TT} = 0.26$ and $\Phi_{SP} = 0.038$.

One further means of analyzing our results is to note that for benzene-biacetyl, $\Phi_{TT} \sim 1.0$, that is, every triplet benzene produces a triplet biacetyl. If we assume $\Phi_{TT} = 1.0$ for our system, we find $\Phi_{ISC} = 0.20$ and $\Phi_{SP} = 0.15$. Table III-V summarizes our experimental findings and the resulting three possible sets of Φ_{SP}, Φ_{ISC} and Φ_{TT}.

At present our data do not permit a choice between the various assumptions I, II and III of Table III-V. Assumption III is probably the most reasonable since at high biacetyl/naphthalene pressure ratios the bimolecular T-T process should be much more efficient than the processes destroying $^3N_0$. The results for benzene-biacetyl are in accord with this belief.[4] Nevertheless, the results from Assumption II cannot be discounted even though the assumption leads to a rather small T-T transfer efficiency. It is hoped that further measurements will permit a better distinction between the various possibilities.

Table III-V. Calculated Values of Quantum Yields
Based on Various Assumptions.

Experimental	
$\Phi_{SP}\Phi_{ISC}$	$\Phi_{TT}\Phi_{ISC}$
0.030	0.20

Calculated			
	Φ_{SP}	Φ_{ISC}	Φ_{TT}
I	0.077	0.39[a]	0.51
II	0.038	0.78[a]	0.26
III	0.15	0.20	1.00[a]

[a] Assumed value; see text.

6. REFERENCES

1. H. S. Taylor and J. R. Bates, Proc. Nat. Acad. Sci., 12, 714 (1926).

2. A. Terenin and V. Ermolaev, Dokl. Akad. Nauk SSSR, 85, 547 (1952).

3. D. Dexter, J. Chem. Phys., 21, 836 (1953); Th. Förster, Disc. Faraday Soc., 27, 7 (1959); G. W. Robinson and R. P. Frosch, J. Chem. Phys., 38, 1187 (1963).

4. H. Ishikawa and W. A. Noyes, J. Chem. Phys., 37, 583 (1962).

5. P. G. Bowers and G. B. Porter, J. Phys. Chem., 68, 2982 (1964).

6. See, for example, J. G. Calvert and J. N. Pitts, Photochemistry (John Wiley and Sons, New York, 1966).

7. G. M. Almy and P. R. Gillette, J. Chem. Phys., 11, 188 (1943).

8. J. H. Baxendale and N. K. Bridge, J. Phys. Chem., 59, 783 (1955).

9. D. F. Evans, J. Chem. Soc., 1953, 345; 1957, 1351; 1957, 3885; 1959, 2753.

10. W. E. Bell and F. E. Blacet, J. Amer. Chem. Soc., 76, 5332 (1954).

11. J. P. Howe and W. A. Noyes, J. Amer. Chem. Soc., 58, 1404 (1936).

12. See Reference 6, p. 309.

DOCUMENT CONTROL DATA · R&D

(Security classification of title, body of abstract and indexing annotation must be entered when the overall report is classified)

1. ORIGINATING ACTIVITY (Corporate author)	2a. REPORT SECURITY CLASSIFICATION
Department of Chemistry University of Kansas Lawrence, Kansas	Unclassified
	2b. GROUP

3. REPORT TITLE

Structure and Reactivity of Energetic Chemical Species

4. DESCRIPTIVE NOTES (Type of report and inclusive dates)

Annual Summary Report (1 November 1967 to 31 October 1968)

5. AUTHOR(S) (Last name, first name, initial)

Kevan, Larry
Harmony, Marlin
Christoffersen, Ralph

6. REPORT DATE	7a. TOTAL NO. OF PAGES	7b. NO. OF REPS
December, 1968	141	120

8a. CONTRACT OR GRANT NO.	9a. ORIGINATOR'S REPORT NUMBER(S)
F04611-67C-0032	
b. PROJECT NO.	
c.	9b. OTHER REPORT NO(S) (Any other numbers that may be assigned this report)
d.	

10. AVAILABILITY/LIMITATION NOTICES

This document is subject to special export controls and each transmittal to foreign governments or foreign nationals may be made only with prior approval of AFRPL (RPPR-STINFO), Edwards, California 93523.

11. SUPPLEMENTARY NOTES	12. SPONSORING MILITARY ACTIVITY
	Rocket Propulsion Laboratory Edwards Air Force Base, California

13. ABSTRACT

Energetic chemical species have been investigated by both theoretical and experimental methods. The spatial distribution of trapped radicals in γ-irradiated ethyleneglycol dimethacrylate polymers and of trapped electrons in γ-irradiated methanol, ethanol and 2-methyltetrahydrofuran has been studied by paramagnetic relaxation methods. The radius within which electrons are trapped increases with decreasing polarity of the matrix. Charge storage in γ-irradiated polymethylmethacrylate (PMMA) and other organic polymers doped with electron traps has been studied by measuring thermally-induced thermoelectric and ohmic currents. The conduction mechanism for the thermoelectric current in PMMA appears to be hole hopping between rotating carbomethoxy side groups. The origin of the ohmic currents is not yet clear. The theoretical technique for obtaining lower energy bounds has been extended to multi-electron, polyatomic molecules by using Gaussian basis orbitals. The use of Gaussians allows all integrals to be evaluated in closed form or by a single numerical integration. In the geminal theory of chemical bonding a new method for the determination of the best separated pair geminals of a closed shell molecule has been developed. The efficiency of triplet-triplet energy transfer in naphthalene-biacetyl mixtures has been studied.

14. KEY WORDS	LINK A		LINK B		LINK C	
	ROLE	WT	ROLE	WT	ROLE	WT
Electronic energy transfer Quantum chemistry - lower bound calculations Geminal theory Radiolysis of polyvinylchloride Thermoelectric currents Trapped electrons in organic solids Electron paramagnetic resonance Paramagnetic relaxation Radiolysis of polymethylmethacrylate Radiolysis of ethyleneglycol dimethacrylate polymers						

INSTRUCTIONS

1. **ORIGINATING ACTIVITY:** Enter the name and address of the contractor, subcontractor, grantee, Department of Defense activity or other organization (*corporate author*) issuing the report.

2a. **REPORT SECURITY CLASSIFICATION:** Enter the overall security classification of the report. Indicate whether "Restricted Data" is included. Marking is to be in accordance with appropriate security regulations.

2b. **GROUP:** Automatic downgrading is specified in DoD Directive 5200.10 and Armed Forces Industrial Manual. Enter the group number. Also, when applicable, show that optional markings have been used for Group 3 and Group 4 as authorized.

3. **REPORT TITLE:** Enter the complete report title in all capital letters. Titles in all cases should be unclassified. If a meaningful title cannot be selected without classification, show title classification in all capitals in parenthesis immediately following the title.

4. **DESCRIPTIVE NOTES:** If appropriate, enter the type of report, e.g., interim, progress, summary, annual, or final. Give the inclusive dates when a specific reporting period is covered.

5. **AUTHOR(S):** Enter the name(s) of author(s) as shown on or in the report. Enter last name, first name, middle initial. If military, show rank and branch of service. The name of the principal author is an absolute minimum requirement.

6. **REPORT DATE:** Enter the date of the report as day, month, year; or month, year. If more than one date appears on the report, use date of publication.

7a. **TOTAL NUMBER OF PAGES:** The total page count should follow normal pagination procedures, i.e., enter the number of pages containing information.

7b. **NUMBER OF REFERENCES:** Enter the total number of references cited in the report.

8a. **CONTRACT OR GRANT NUMBER:** If appropriate, enter the applicable number of the contract or grant under which the report was written.

8b, 8c, & 8d. **PROJECT NUMBER:** Enter the appropriate military department identification, such as project number, subproject number, system numbers, task number, etc.

9a. **ORIGINATOR'S REPORT NUMBER(S):** Enter the official report number by which the document will be identified and controlled by the originating activity. This number must be unique to this report.

9b. **OTHER REPORT NUMBER(S):** If the report has been assigned any other report numbers (*either by the originator or by the sponsor*), also enter this number(s).

10. **AVAILABILITY/LIMITATION NOTICES:** Enter any limitations on further dissemination of the report, other than those imposed by security classification, using standard statements such as:

(1) "Qualified requesters may obtain copies of this report from DDC."

(2) "Foreign announcement and dissemination of this report by DDC is not authorized."

(3) "U. S. Government agencies may obtain copies of this report directly from DDC. Other qualified DDC users shall request through

_____."

(4) "U. S. military agencies may obtain copies of this report directly from DDC. Other qualified users shall request through

_____."

(5) "All distribution of this report is controlled. Qualified DDC users shall request through

_____."

If the report has been furnished to the Office of Technical Services, Department of Commerce, for sale to the public, indicate this fact and enter the price, if known.

11. **SUPPLEMENTARY NOTES:** Use for additional explanatory notes.

12. **SPONSORING MILITARY ACTIVITY:** Enter the name of the departmental project office or laboratory sponsoring (*paying for*) the research and development. Include address.

13. **ABSTRACT:** Enter an abstract giving a brief and factual summary of the document indicative of the report, even though it may also appear elsewhere in the body of the technical report. If additional space is required, a continuation sheet shall be attached.

It is highly desirable that the abstract of classified reports be unclassified. Each paragraph of the abstract shall end with an indication of the military security classification of the information in the paragraph, represented as (TS), (S), (C), or (U).

There is no limitation on the length of the abstract. However, the suggested length is from 150 to 225 words.

14. **KEY WORDS:** Key words are technically meaningful terms or short phrases that characterize a report and may be used as index entries for cataloging the report. Key words must be selected so that no security classification is required. Identifiers, such as equipment model designation, trade name, military project code name, geographic location, may be used as key words but will be followed by an indication of technical context. The assignment of links, rules, and weights is optional.